



UNIVERSIDAD NACIONAL DE COLOMBIA

**Desarrollo teórico e implementación computacional de una metodología no Born-Oppenheimer de teoría de funcionales de la densidad basada en el método del orbital molecular nuclear con escalamiento cúbico para el estudio de efectos cuánticos nucleares**

**Félix Santiago Moncada Arias**

Universidad Nacional de Colombia  
Facultad de Ciencias, Departamento de Química  
Bogotá, Colombia  
2013





UNIVERSIDAD NACIONAL DE COLOMBIA

**Theoretical development and computational implementation of a non Born-Oppenheimer density functional theory methodology based on the nuclear molecular orbital method with cubic scaling for the study of nuclear quantum effects**

**Félix Santiago Moncada Arias**

Universidad Nacional de Colombia  
Chemistry Department  
Bogotá, Colombia  
2013



**Desarrollo teórico e implementación computacional de una metodología no Born-Oppenheimer de teoría de funcionales de la densidad basada en el método del orbital molecular nuclear con escalamiento cúbico para el estudio de efectos cuánticos nucleares**

**Félix Santiago Moncada Arias**

Tesis presentada como requisito parcial para optar al título de:  
**Magister en Ciencias - Química**

Director(a):  
Ph.D. Andrés Reyes

Grupo de Investigación:  
Química Cuántica y Computacional

Universidad Nacional de Colombia  
Facultad de Ciencias, Departamento de Química  
Bogotá, Colombia  
2013



**Theoretical development and computational implementation of a non Born-Oppenheimer density functional theory methodology based on the nuclear molecular orbital method with cubic scaling for the study of nuclear quantum effects**

**Félix Santiago Moncada Arias**

Thesis presented in partial fulfillment of the requirements for the degree of:  
**Master in Science - Chemistry**

Advisor:  
Ph.D. Andrés Reyes

Research Group:  
Quantum and Computational Chemistry

Universidad Nacional de Colombia  
Chemistry Department  
Bogotá, Colombia  
2013

## Acknowledgements

We gratefully acknowledge contributions from: MSc. Jorge Charry to chapters 2 and 3; MSc. Edwin Posada to chapters 3 and 6; Dr. Roberto Flores-Moreno to chapters 3 and 4; Sergio González to chapter 4 and Jonathan Romero and Lalita Uribe to chapter 5. We thank Dr. Adam Wasserman for helpful discussions. We gratefully acknowledge the financial support of Universidad Nacional de Colombia, División de Investigación sede Bogotá. We thank Jorge Charry and Gisel Peña for proofreading this manuscript.

## Abstract

In this work, we present some theoretical developments on the Any Particle Molecular Orbital (APMO) method to reduce its computational cost and to include correlation between particles of different species. These methodologies were implemented in the LOWDIN code. We also present APMO applications to the study of nuclear quantum effects and muonic chemistry. Our results reveal that the inclusion of nuclear-electron correlation improves the accuracy of the nuclear quantum effects predicted with the APMO method. APMO calculations with lower scaling with respect to the size of the system are achieved using a localized Hartree product approximation and the auxiliary density functional theory.

**Keywords:** any particle molecular orbital, nuclear quantum effects, muonic chemistry, density functional theory, auxiliary density, Hartree product, LOWDIN code

## Resumen

En este trabajo se presentan algunos desarrollos teóricos del método del orbital molecular para cualquier partícula (APMO) para reducir su costo computacional y para incluir correlación entre partículas de especies diferentes. Estas metodologías fueron implementadas en el código LOWDIN. También se presentan aplicaciones del método APMO al estudio de efectos cuánticos nucleares y química muónica. Nuestros resultados muestran que incluir correlación núcleo-electrón incrementa la precisión de los efectos cuánticos nucleares predichos con el método APMO. Para lograr cálculos APMO con menor escalamiento respecto al tamaño del sistema se usa la aproximación del producto localizado de Hartree y la teoría del funcional de la densidad auxiliar.

**Palabras clave:** orbital molecular para cualquier partícula, efectos cuánticos nucleares, química muónica, teoría del funcional de la densidad, densidad auxiliar, producto de Hartree, código LOWDIN.

# Content

<b>Acknowledgements</b>	<b>viii</b>
<b>Abstract</b>	<b>ix</b>
<b>List of Abbreviations</b>	<b>xi</b>
<b>1 Introduction</b>	<b>2</b>
1.1 Nuclear Quantum Effects . . . . .	2
1.2 Muonic Chemistry . . . . .	2
1.3 Nuclear Molecular Orbitals Methods . . . . .	3
1.4 This work . . . . .	4
<b>2 Multicomponent DFT</b>	<b>6</b>
2.1 APMO/DFT . . . . .	6
2.2 The exchange-correlation functional . . . . .	10
2.2.1 Pair density . . . . .	10
2.2.2 APMO/HF exchange functional . . . . .	11
2.2.3 Nuclear-electron correlation functionals . . . . .	12
2.3 APMO/DFT proton affinities . . . . .	12
<b>3 APMO Calculations with Cubic Scaling</b>	<b>15</b>
3.1 Theory . . . . .	16
3.1.1 APMO/ADFT Theory . . . . .	16
3.1.2 APMO/ADFT/HPA method . . . . .	18
3.2 APMO/ADFT/HPA calculations . . . . .	19
3.2.1 APMO/ADFT/HPA numerical accuracy . . . . .	19
3.2.2 APMO/ADFT/HPA scaling . . . . .	22
3.3 APMO/ADFT calculations . . . . .	22
3.3.1 Building auxiliary basis sets . . . . .	23
3.3.2 APMO/ADFT scaling . . . . .	23
3.3.3 APMO/ADFT numerical accuracy . . . . .	25

---

<b>4</b>	<b>MBPT(2) for Any Quantum Particle</b>	<b>28</b>
4.1	APMO/MBPT(2) Theory . . . . .	29
4.1.1	APMO/HF theory . . . . .	29
4.1.2	APMO/MBPT(2) theory . . . . .	30
4.1.3	APMO/HF/HPA theory . . . . .	30
4.1.4	APMO/MBPT(2)/HPA theory . . . . .	32
4.2	Computational details . . . . .	32
4.3	APMO/MBPT(2)/HPA energies . . . . .	33
4.4	APMO/MBPT(2)/HPA computational efficiency . . . . .	38
4.5	Negative muon-electron correlation . . . . .	40
4.6	An approximated MBPT(2) nuclear-electron correlation functional . . . . .	43
<b>5</b>	<b>Isotope Effects on Protonated Rare Gas Clusters</b>	<b>46</b>
5.1	Methodology . . . . .	47
5.2	Energy Decomposition Analysis . . . . .	47
5.3	Results and Discussion . . . . .	49
5.3.1	RgX <sup>+</sup> complexes . . . . .	49
5.3.2	Rg <sub>2</sub> X <sup>+</sup> complexes . . . . .	53
5.3.3	Rg <sub>3</sub> X <sup>+</sup> complexes . . . . .	56
<b>6</b>	<b>Muonic Chemistry at the Full-CI Level</b>	<b>60</b>
6.1	Theory . . . . .	61
6.1.1	APMO theory for muonic systems . . . . .	61
6.1.2	Finite Nuclear Mass Correction (FNMC) . . . . .	62
6.2	Computational Details . . . . .	62
6.3	Results and discussion . . . . .	63
6.3.1	Nuclear mass effect . . . . .	63
6.3.2	Muonic basis set errors . . . . .	63
6.3.3	Electron-muon correlation . . . . .	65
6.3.4	Partial muon screening and muon relaxation effects . . . . .	65
6.3.5	Combined effects in IP . . . . .	68
6.3.6	Combined effects in reaction energies . . . . .	69
<b>7</b>	<b>Conclusions</b>	<b>72</b>
	<b>Bibliography</b>	<b>75</b>

# List of Abbreviations

$\mu$  Negative muon

ADFT Auxiliary Density Functional Theory

APMO Any Particle Molecular Orbital

APMO/ADFT Any Particle Molecular Orbital in the Auxiliary Density Functional Theory framework

APMO/ADFT/HPA Any Particle Molecular Orbital with Auxiliary Density Functional Theory for light particles and a Hartree Product Approximation for heavy particles

APMO/DFT Any Particle Molecular Orbital in the Density Functional Theory framework

APMO/FCI Any Particle Molecular Orbital at Full Configuration Interaction level

APMO/FNMC Any Particle Molecular Orbital with Finite Nuclear Mass Correction

APMO/FNMC/eFCI Any Particle Molecular Orbital with Finite Nuclear Mass Correction at electronic Full Configuration Interaction level

APMO/FNMC/FCI Any Particle Molecular Orbital with Finite Nuclear Mass Correction at Full Configuration Interaction level

APMO/HF Any Particle Molecular Orbital at Hartree Fock level

APMO/HF/HPA Any Particle Molecular Orbital at Hartree Fock level with a Hartree Product Approximation for heavy particles

APMO/MBPT(2) Any Particle Molecular Orbital at second order Many Body Perturbation Theory level

APMO/MBPT(2)/HPA Any Particle Molecular Orbital at second order Many Body Perturbation Theory level with a Hartree Product Approximation for heavy particles

BOA Born-Oppenheimer Approximation

CS Colle Salvetti

DFT Density Functional Theory

EDA Energy Decomposition Analysis

FCI Full Configuration Interaction

FNMC Finite Nuclear Mass Correction

GTFs Gaussian Type Functions

HF Hartree-Fock

HPA Hartree Product Approximation

IEs Isotope effects

IP Ionization Potential

MBPT(2) second order Many Body Perturbation Theory

MCMO Multi-Component Molecular Orbital

MO/HF regular electronic structure Hartree Fock

MO/MBPT(2) regular electronic structure second order Many Body Perturbation Theory

NEO Nuclear-Electronic Orbital

NMO Nuclear Molecular Orbital

NOMO Nuclear Orbital plus Molecular Orbital

NQEs Nuclear Quantum Effects

PA Proton Affinity

PES Potential Energy Surface

$X\mu$  X atom in which one electron was replaced with a negative muon

# 1 Introduction

## 1.1 Nuclear Quantum Effects

For centuries chemists have been interested in exploring the properties of atoms, molecules and materials which are composed of electrons, protons and neutrons. From a theoretical perspective, the Born-Oppenheimer approximation (BOA) is one of the most fundamental approximations of molecular physics and chemistry. This approximation has been used successfully in many research areas ranging from spectroscopy to quantum chemistry making possible the study of molecular systems containing thousands of electrons and nuclei [1].

Despite the success of quantum chemistry methods based on the BOA they still fail to include nuclear quantum effects (NQEs) on the molecular electronic structure, because the BOA completely uncouples the electronic and nuclear degrees of freedom. For most chemical systems these NQEs are very small. However, for systems containing light or delocalized nuclei, they may be very important [2–4].

We are interested in developing non-BOA methodologies to allow the theoretical study of these NQEs on the electronic structure of atoms and molecules.

## 1.2 Muonic Chemistry

In recent decades, there has been a growing interest in studying the so-called exotic atoms and molecules (i.e. systems containing either positrons, muons, among others) due primarily to advances in the generation and manipulation of these subatomic particles. Among these exotic systems those containing positrons and positive muons have received most of the attention by the chemistry community. This is due in part to advances in the development of positron and positive muon techniques which, for instance, have resulted in methods currently used in medicine and chemistry such as positron emission tomography [5] and muon spin resonance [6]. In contrast, the study of systems containing negative muons ( $\mu^-$  in the rest of the document) has mainly attracted the physicists' community. They have investigated extensively for the last 60 years, both theoretical and experimentally, muonic atoms and molecules. These studies have been inspired primarily by the potential of muonic systems to catalyze nuclear fusion processes. Refs [6–8] and references therein present overviews of muon catalyzed fusion in the  $dt\mu$  molecule.

A wide variety of aspects have been investigated experimentally on these negative muonic

systems: muon transfer and capture processes [6, 7, 9, 10], nuclear fusion reaction rates [6, 7, 11], quantum electrodynamics effects (e.g. Lamb shifts and vacuum polarization)[12, 13], X-ray spectroscopy [14] among others. From a theoretical perspective, the investigation of atomic and molecular muonic systems has also been used to study the above-mentioned properties [9, 15–20] and to determine the accuracy of many-body approximation methods. [21–27]

The chemical properties of  $\mu$ -many-electron atoms (denoted in the rest of the document by  $X\mu$ , where  $X$  is the atomic symbol)) and molecules were rarely investigated in the last century. There are only a few reports of  $\mu$ -spin resonance studies on solids [28–32]. From a theoretical perspective, there are a few Dirac-Fock calculations on many-electron muonic atoms [33, 34]. The lack of reports on these muonic species is in part due to: 1. experimental difficulties in the preparation and manipulation of these short-lived systems; 2. limitations of the theoretical methods implemented so far to study molecular systems containing particles other than electrons and nuclei.

In this regard, in recent years a couple of papers [35–37] have presented measurements of reaction rates for the collisional process  ${}^4\text{He}\mu + \text{H}_2 \rightarrow {}^4\text{He}\mu \text{H} + \text{H}$ . It has been concluded from these reports that  $\text{He}\mu$  chemically behaves as a heavy isotope of hydrogen.

Inspired by the findings of these experimental studies, we have studied theoretically electronic properties of muonic atoms and molecules in which one or two electron has been replaced by negative muons [38–41].

## 1.3 Nuclear Molecular Orbitals Methods

In recent years, several authors have proposed alternative approaches beyond the BOA to include NQE directly on the electronic structure and molecular geometries [2–4]. Examples of these methods are the Nuclear Orbital plus Molecular Orbital method (NOMO) [42, 43], the Multi-Component Molecular Orbital method (MCMO) [44], the Nuclear-Electronic Orbital approach (NEO) [45]. One main advantage of these nuclear molecular orbital (NMO) methods is that the NQEs on the electronic structure and molecular properties are obtained in one single calculation and not as further corrections.

The NMO approach has been extended to different levels of theory including wave function based methods such as Hartree-Fock (HF) [42–45], second-order perturbation theory [46–49], configuration interaction [44–46, 50, 51], coupled-cluster [46], explicitly correlated methods [52, 53], among others. It has also been derived for density functional theory (DFT) within the Kohn-Sham approach [54–57].

NMO methods based on the HF reference for electronic and nuclear wave functions have been used successfully to study NQEs on a variety of molecular systems such as: the anharmonicity of diatomic molecules [58], primary and secondary isotope effects on geometry and stability [54, 59–65], kinetic isotope effects [66, 67], ionization energies [68, 69] phase-transition properties of ferroelectric materials [70–72], nuclear quantum effects on magnetic

properties [73], among other applications. It has been shown that sometimes the inclusion of nuclear-electron correlation may significantly improve the calculation of stabilization energies and internuclear distances [63, 64], which in some cases may lead to gigantic effects on the symmetry of low-barrier H-bonded systems [74].

In our group, we have proposed an extension of the NMO methods to any kind of quantum particle. We refer to this methodology as the Any Particle Molecular Orbital approach (APMO) [61, 63]. At the APMO Hartree-Fock (APMO/HF) level of theory, the total wave function is constructed as a product of wave functions for each type of quantum particle, described as Slater determinants for fermionic species and symmetric products for bosonic species. However, we can identify two problems with the APMO/HF method: First, it does not include interparticle correlation and second, it has a formal quartic scaling with respect to the basis sets sizes.

It has been shown that in NMO calculations including nuclear-electron correlation is crucial to obtain accurate results [51, 53]. The APMO method has been extended to the second-order perturbation theory (APMO/MBPT(2)) level [63] to include interparticle correlation. However, sometimes perturbation theory approaches do not recover enough of nuclear-electron correlation [46]. One way to include enough nuclear-electron correlation is to perform NMO calculations under the density functional theory formalism including an adequate nuclear-electron correlation functional [57].

The APMO method, as well as most of NMO schemes, employ localized gaussian type functions (GTFs) to construct molecular orbitals. As a result, its formal scaling with respect to the different basis set sizes is identical to that of a BOA method of the same level of theory. For instance, APMO/HF and APMO/MBPT(2) formal scalings are quartic and quintic respectively. In consequence of this scaling behavior, APMO calculations of large systems will turn unmanageable, e.g., in solvation phenomena studies. Under the DFT framework for electrons, reduction of the self-consistent field calculations formal scaling from quartic to cubic has been achieved by using the variational approximation of the Coulomb potential [75–79].

## 1.4 This work

In this work, we present some theoretical developments on the APMO method to reduce its computational cost and to include correlation between particles of different species, as well as APMO applications to the study of NQEs and muonic chemistry. The methodologies developed in this work were implemented in the LOWDIN software, which is developed in our group [80].

This thesis is organized as follows: In chapter 2 we provide the expressions of Kohn-Sham DFT extended to the APMO framework and discuss general aspects of the multicomponent exchange correlation functional. In chapter 3 we present the extension of the auxiliary density functional theory (ADFT) to the APMO framework, as well as its combination

---

with the Hartree product approximation (HPA). In chapter 4 we present an alternative APMO/MBPT(2) method, in which the reference wave function is constructed as a product of Slater determinants for light species and Hartree products of localized orbitals for heavy species. In chapter 5 we investigate Hydrogen isotope and nuclear quantum effects on geometries and binding energies of small protonated rare gas clusters with the APMO/MBPT(2) level of theory. In chapter 6 we present a study of the chemistry of muonic atoms at the APMO full configuration interaction (APMO/FCI) level. Finally in chapter 7 we provide concluding remarks.

## 2 Multicomponent DFT

In this chapter we present the general expressions of DFT applied to a system containing different quantum species following a Kohn-Sham methodology. We will refer to this method as APMO/DFT. These expressions are a straightforward extension of those presented in Refs. [54–57, 81, 82] applied to nuclear and electron densities. For simplicity, in this work we use atomic units in all the equations and assume real wavefunctions.

### 2.1 APMO/DFT

We consider a system containing  $N_q$  different quantum species. This system has  $N_\alpha$  particles of the  $\alpha$  species,  $N_\beta$  particles of the  $\beta$  species and so on, under an external scalar field  $V^x(\mathbf{r})$ . The hamiltonian for this system is

$$\hat{H} = \sum_{\alpha}^{N_q} \hat{K}_{\alpha} + \sum_{\alpha}^{N_q} \hat{V}_{\alpha}^x + \sum_{\alpha}^{N_q} \hat{V}_{\alpha\alpha} + \sum_{\beta>\alpha}^{N_q} \hat{V}_{\alpha\beta}, \quad (2-1)$$

where  $\hat{K}_{\alpha}$ ,  $\hat{V}_{\alpha}^x$  and  $\hat{V}_{\alpha\alpha}$  are the kinetic energy, external potential and intraspecies interaction operators for the  $\alpha$  species and  $\hat{V}_{\alpha\beta}$  is the interaction operator for  $\alpha$  and  $\beta$  species. Considering coulombic interactions, these energy operators are

$$\hat{K}_{\alpha} = - \sum_i^{N_{\alpha}} \frac{\nabla_{\mathbf{r}_{\alpha i}}^2}{2m_{\alpha}}, \quad (2-2)$$

$$\hat{V}_{\alpha}^x = q_{\alpha} \sum_i^{N_{\alpha}} V^x(\mathbf{r}_{\alpha i}), \quad (2-3)$$

$$\hat{V}_{\alpha\alpha} = q_{\alpha}^2 \sum_{j>i}^{N_{\alpha}} \frac{1}{|\mathbf{r}_{\alpha i} - \mathbf{r}_{\alpha j}|}, \quad (2-4)$$

$$\hat{V}_{\alpha\beta} = q_{\alpha} q_{\beta} \sum_i^{N_{\alpha}} \sum_j^{N_{\beta}} \frac{1}{|\mathbf{r}_{\alpha i} - \mathbf{r}_{\beta j}|} \quad \forall \beta \neq \alpha, \quad (2-5)$$

where  $q_{\alpha}$  and  $m_{\alpha}$  are the charge and mass of  $\alpha$  species respectively. If the external potential is produced by a set of  $N_c$  point charges,

$$V^x(\mathbf{r}) = \sum_I^{N_c} \frac{q_I}{|\mathbf{r} - \mathbf{r}_I|} + \sum_{J>I}^{N_c} \frac{q_I q_J}{|\mathbf{r}_I - \mathbf{r}_J|}. \quad (2-6)$$

The Schrödinger equation for this system is

$$\hat{H}(\{\mathbf{r}\})\Psi(\{\mathbf{r}\}) = E\Psi(\{\mathbf{r}\}). \quad (2-7)$$

Here,  $\{\mathbf{r}\}$  represents the set of the coordinates of all particles of the system.

The wavefunction squared,  $|\Psi(\{\mathbf{r}\})|^2$ , represents the probability density of finding the particles at the  $(\{\mathbf{r}\})$  set of coordinates. The single particle density of the  $\alpha$  species is obtained by integrating the wavefunction squared in all coordinates except one,

$$\rho_\alpha(\mathbf{r}) = \iint \cdots \int |\Psi(\{\mathbf{r}\})|^2 \{d\mathbf{r} \neq d\mathbf{r}_{\alpha 1}\}, \quad (2-8)$$

$\rho_\alpha(\mathbf{r})$  represents the probability of finding one particle of  $\alpha$  species at  $\mathbf{r}$  and integrates to  $N_\alpha$ ,

$$\int \rho_\alpha(\mathbf{r})d\mathbf{r} = N_\alpha. \quad (2-9)$$

Following Refs. [81, 82] the Hohenberg-Kohn theorems can be extended to systems with many species. Therefore, the energy of the system is a functional of the set of the single particle densities,  $\{\rho\}$ ,

$$\begin{aligned} E[\{\rho\}] &= \langle \Psi | \hat{H} | \Psi \rangle \\ &= \sum_{\alpha}^{N_q} \langle \Psi | \hat{K}_\alpha | \Psi \rangle + \sum_{\alpha}^{N_q} \langle \Psi | \hat{V}_\alpha^x | \Psi \rangle + \sum_{\alpha}^{N_q} \langle \Psi | \hat{V}_{\alpha\alpha} | \Psi \rangle + \sum_{\beta > \alpha}^{N_q} \langle \Psi | \hat{V}_{\alpha\beta} | \Psi \rangle \\ &= \sum_{\alpha}^{N_q} K_\alpha[\{\rho\}] + \sum_{\alpha}^{N_q} q_\alpha \int \rho_\alpha(\mathbf{r})V^x(\mathbf{r})d\mathbf{r} + \sum_{\alpha}^{N_q} V_{\alpha\alpha}[\{\rho\}] + \sum_{\beta > \alpha}^{N_q} V_{\alpha\beta}[\{\rho\}]. \end{aligned} \quad (2-10)$$

The ground-state of the system corresponds to the set of densities that minimize this functional. Here,  $K_\alpha[\{\rho\}]$  and  $V_{\alpha\alpha}[\{\rho\}]$  are the kinetic energy and intraspecies interaction functionals for  $\alpha$  species and  $V_{\alpha\beta}[\{\rho\}]$  is the  $\alpha$  and  $\beta$  interaction functional.

Following Kohn-Sham method [81, 82], we now construct reference spin-orbitals,  $\chi$ , for each species. These spin-orbitals are obtained from a non-interacting system and are composed of a spatial orbital  $\psi$  and a spin function. They form an orthonormal set, and the density of each species is constructed from them,

$$\rho_\alpha = \sum_i^{N_\alpha} |\psi_{\alpha i}|^2. \quad (2-11)$$

The energy functional can be rewritten as,

$$E[\{\rho\}] = \sum_{\alpha}^{N_q} K_\alpha^{KS}[\rho_\alpha] + \sum_{\alpha}^{N_q} q_\alpha \int \rho_\alpha(\mathbf{r})V^x(\mathbf{r})d\mathbf{r} + \sum_{\alpha}^{N_q} J_{\alpha\alpha}[\rho_\alpha] + \sum_{\beta > \alpha}^{N_q} J_{\alpha\beta}[\rho_\alpha, \rho_\beta] + E^{xc}[\{\rho\}]. \quad (2-12)$$

Where  $K_\alpha^{KS}[\rho_\alpha]$  is the Kohn-Sham kinetic energy functional and  $J_{\alpha\alpha}[\rho_\alpha]$  and  $J_{\alpha\beta}[\rho_\alpha, \rho_\beta]$  are the Hartree functionals for the  $\alpha$  repulsion and  $\alpha - \beta$  interaction. They are defined as,

$$K_\alpha^{KS}[\rho_\alpha] = - \sum_i^{N_\alpha} \int \psi_{\alpha i}(\mathbf{r}) \frac{\nabla_{\mathbf{r}}^2}{2m_\alpha} \psi_{\alpha i}(\mathbf{r}) d\mathbf{r}, \quad (2-13)$$

$$J_{\alpha\alpha}[\rho_\alpha] = \frac{q_\alpha^2}{2} \iint \frac{\rho_\alpha(\mathbf{r})\rho_\alpha(\mathbf{r}')}{|\mathbf{r} - \mathbf{r}'|} d\mathbf{r}d\mathbf{r}', \quad (2-14)$$

$$J_{\alpha\beta}[\rho_\alpha, \rho_\beta] = q_\alpha q_\beta \iint \frac{\rho_\alpha(\mathbf{r})\rho_\beta(\mathbf{r}')}{|\mathbf{r} - \mathbf{r}'|} d\mathbf{r}d\mathbf{r}'. \quad (2-15)$$

The exchange correlation functional  $E^{xc}[\{\rho\}]$  includes the interactions neglected in the Kohn-Sham kinetic energy and the Hartree interactions functionals,

$$\begin{aligned} E^{xc}[\{\rho\}] &= \sum_{\alpha}^{N_q} (K_\alpha[\{\rho\}] - K_\alpha^{KS}[\rho_\alpha]) + \sum_{\alpha}^{N_q} (V_{\alpha\alpha}[\{\rho\}] - J_{\alpha\alpha}[\rho_\alpha]) \\ &\quad + \sum_{\beta > \alpha}^{N_q} (V_{\alpha\beta}[\{\rho\}] - J_{\alpha\beta}[\rho_\alpha, \rho_\beta]). \end{aligned} \quad (2-16)$$

The canonical Kohn-Sham equations are,

$$\begin{aligned} \left( - \frac{\nabla_{\mathbf{r}}^2}{2m_\alpha} + q_\alpha V^x(\mathbf{r}) + q_\alpha^2 \int \frac{\rho_\alpha(\mathbf{r}')}{|\mathbf{r} - \mathbf{r}'|} d\mathbf{r}' + q_\alpha \sum_{\beta \neq \alpha}^{N_q} q_\beta \int \frac{\rho_\beta(\mathbf{r}')}{|\mathbf{r} - \mathbf{r}'|} d\mathbf{r}' \right. \\ \left. + V_\alpha^{xc}[\{\rho\}](\mathbf{r}) \right) \psi_{\alpha i}(\mathbf{r}) = \epsilon_{\alpha i} \psi_{\alpha i}(\mathbf{r}), \end{aligned} \quad (2-17)$$

for each particle  $i$  of each species  $\alpha$ . Here we introduced the exchange-correlation potential  $V_\alpha^{xc}$ , which is defined as the functional derivative of  $E^{xc}$  with respect to the  $\alpha$  species density.

$$V_\alpha^{xc}[\{\rho\}] = \frac{\delta E^{xc}[\{\rho\}]}{\delta \rho_\alpha}. \quad (2-18)$$

Each orbital  $\psi_{\alpha i}$  is constructed as a linear combination of  $B_\alpha$  GTFs,  $\phi_\alpha$ .

$$\psi_{\alpha i} = \sum_{\mu}^{B_\alpha} C_{\alpha i \mu} \phi_{\alpha \mu} \quad (2-19)$$

$$\phi_{\alpha \mu}(\mathbf{r}) = N(x - X)^n (y - Y)^m (z - Z)^l \exp(-\zeta(\mathbf{r} - \mathbf{R})^2). \quad (2-20)$$

Here  $\mathbf{R}$ ,  $n$ ,  $m$ ,  $l$  and  $\zeta$  are the parameters of each GTF and  $N$  is a normalization constant.

The energy functional can be rewritten in terms of the basis set functions,

$$E[\{\rho\}] = \sum_{\alpha}^{N_q} \sum_{\mu\nu}^{B_\alpha} P_{\alpha\mu\nu} \left( H_{\alpha\mu\nu} + \frac{1}{2} G_{\alpha\mu\nu} + \frac{1}{2} I_{\alpha\mu\nu} \right) + E^{xc}[\{\rho\}], \quad (2-21)$$

where  $\mathbf{H}_\alpha$ ,  $\mathbf{P}_\alpha$ ,  $\mathbf{G}_\alpha$  and  $\mathbf{I}_\alpha$  are the  $\alpha$  core, density, two-particles and coupling matrices. Their elements are

$$P_{\alpha\mu\nu} = \sum_{j>i}^{B_\alpha} C_{\alpha i\mu} C_{\alpha j\nu}, \quad (2-22)$$

$$\begin{aligned} H_{\alpha\mu\nu} &= \left\langle \phi_{\alpha\mu} \left| -\frac{\nabla_{\mathbf{r}}^2}{2m_\alpha} + q_\alpha V^x \right| \phi_{\alpha\nu} \right\rangle \\ &= \int \phi_{\alpha\mu}(\mathbf{r}) \left( -\frac{\nabla_{\mathbf{r}}^2}{2m_\alpha} + q_\alpha V^x(\mathbf{r}) \right) \phi_{\alpha\nu}(\mathbf{r}) d\mathbf{r}, \end{aligned} \quad (2-23)$$

$$G_{\alpha\mu\nu} = q_\alpha^2 \sum_{\sigma\tau}^{B_\alpha} P_{\alpha\sigma\tau} (\phi_{\alpha\mu} \phi_{\alpha\nu} | \phi_{\alpha\sigma} \phi_{\alpha\tau}), \quad (2-24)$$

$$I_{\alpha\mu\nu} = \sum_{\beta \neq \alpha}^{N_q} q_\alpha q_\beta \sum_{\sigma\tau}^{B_\beta} P_{\beta\sigma\tau} (\phi_{\alpha\mu} \phi_{\alpha\nu} | \phi_{\beta\sigma} \phi_{\beta\tau}). \quad (2-25)$$

The four center integrals are defined as,

$$(\phi_{\alpha\mu} \phi_{\alpha\nu} | \phi_{\alpha\sigma} \phi_{\alpha\tau}) = \langle \phi_{\alpha\mu} \phi_{\alpha\nu} | \phi_{\alpha\sigma} \phi_{\alpha\tau} \rangle = \iint \frac{\phi_{\alpha\mu}(\mathbf{r}) \phi_{\alpha\nu}(\mathbf{r}) \phi_{\alpha\sigma}(\mathbf{r}') \phi_{\alpha\tau}(\mathbf{r}')}{|\mathbf{r} - \mathbf{r}'|} d\mathbf{r} d\mathbf{r}', \quad (2-26)$$

$$(\phi_{\alpha\mu} \phi_{\alpha\nu} | \phi_{\beta\sigma} \phi_{\beta\tau}) = \langle \phi_{\alpha\mu} \phi_{\beta\sigma} | \phi_{\alpha\nu} \phi_{\beta\tau} \rangle = \iint \frac{\phi_{\alpha\mu}(\mathbf{r}) \phi_{\alpha\nu}(\mathbf{r}) \phi_{\beta\sigma}(\mathbf{r}') \phi_{\beta\tau}(\mathbf{r}')}{|\mathbf{r} - \mathbf{r}'|} d\mathbf{r} d\mathbf{r}'. \quad (2-27)$$

Given these definitions, to find the ground state of a system we need the set of coefficients  $\{C\}$  that minimizes the energy functional. We proceed to solve iteratively the Roothan equations for each species,

$$\mathbf{K}_\alpha \mathbf{C}_\alpha = \mathbf{S}_\alpha \mathbf{C}_\alpha \epsilon_\alpha. \quad (2-28)$$

Here  $\epsilon_\alpha$  is a vector containing the eigenvalues of  $\alpha$  species orbitals and  $\mathbf{C}_\alpha$  is a matrix containing the coefficients of each  $\alpha$  species orbital.  $\mathbf{K}_\alpha$  and  $\mathbf{S}_\alpha$  are the Kohn-Sham and overlap matrices. Their elements are,

$$S_{\alpha\mu\nu} = \int \phi_{\alpha\mu}(\mathbf{r}) \phi_{\alpha\nu}(\mathbf{r}) d\mathbf{r}, \quad (2-29)$$

$$K_{\alpha\mu\nu} = H_{\alpha\mu\nu} + G_{\alpha\mu\nu} + I_{\alpha\mu\nu} + V_{\alpha\mu\nu}^{xc}, \quad (2-30)$$

where the exchange-correlation potential matrix for  $\alpha$  species,  $\mathbf{V}_\alpha^{xc}$  was defined. Its elements are

$$\begin{aligned} V_{\alpha\mu\nu}^{xc} &= \langle \phi_{\alpha\mu} | V_\alpha^{xc}[\{\rho\}] | \phi_{\alpha\nu} \rangle \\ &= \int \phi_{\alpha\mu}(\mathbf{r}) V_\alpha^{xc}[\{\rho\}](\mathbf{r}) \phi_{\alpha\nu}(\mathbf{r}) d\mathbf{r}. \end{aligned} \quad (2-31)$$

To perform APMO/DFT calculations, we need to know an analytic expression for  $E^{xc}$ .

## 2.2 The exchange-correlation functional

As discussed above, there are two contributions to  $E^{xc}$ , one from the inclusion of the Kohn-Sham kinetic energy operators and the other from the inclusion of the Hartree interaction operators. In this section we focus on the contribution of the Coulomb interactions to the exchange-correlation energy. If we neglect the kinetic energy terms from eq. 2-16,

$$E^{xc}[\{\rho\}] = \sum_{\alpha}^{N_q} (V_{\alpha\alpha}[\{\rho\}] - J_{\alpha\alpha}[\rho_{\alpha}]) + \sum_{\beta>\alpha}^{N_q} (V_{\alpha\beta}[\{\rho\}] - J_{\alpha\beta}[\rho_{\alpha}, \rho_{\beta}]). \quad (2-32)$$

### 2.2.1 Pair density

Consider now the definition of the pair densities for particles of the same species,  $\rho_{\alpha\alpha}$ , and for particles of different species,  $\rho_{\alpha\beta}$ ,

$$\rho_{\alpha\alpha}(\mathbf{r}, \mathbf{r}') = \iint \cdots \int |\Psi(\{\mathbf{r}\})|^2 \{d\mathbf{r} \neq d\mathbf{r}_{\alpha 1}, d\mathbf{r}_{\alpha 2}\}, \quad (2-33)$$

$$\rho_{\alpha\beta}(\mathbf{r}, \mathbf{r}') = \iint \cdots \int |\Psi(\{\mathbf{r}\})|^2 \{d\mathbf{r} \neq d\mathbf{r}_{\alpha 1}, d\mathbf{r}_{\beta 1}\}. \quad (2-34)$$

These pair densities represent the probability of finding one particle at  $\mathbf{r}$  and the other at  $\mathbf{r}'$ . It follows that,

$$\int \rho_{\alpha\alpha}(\mathbf{r}, \mathbf{r}') d\mathbf{r}' = \rho_{\alpha}(\mathbf{r}), \quad (2-35)$$

$$\iint \rho_{\alpha\alpha}(\mathbf{r}, \mathbf{r}') d\mathbf{r} d\mathbf{r}' = \frac{N_{\alpha}(N_{\alpha} - 1)}{2}, \quad (2-36)$$

$$\int \rho_{\alpha\beta}(\mathbf{r}, \mathbf{r}') d\mathbf{r}' = \rho_{\alpha}(\mathbf{r}), \quad (2-37)$$

$$\iint \rho_{\alpha\beta}(\mathbf{r}, \mathbf{r}') d\mathbf{r} d\mathbf{r}' = N_{\alpha} N_{\beta}. \quad (2-38)$$

The exact Coulomb interaction functionals can be written in terms of the pair densities,

$$V_{\alpha\alpha}[\{\rho\}] = \frac{q_{\alpha}^2}{2} \iint \frac{\rho_{\alpha\alpha}(\mathbf{r}, \mathbf{r}')}{|\mathbf{r} - \mathbf{r}'|} d\mathbf{r} d\mathbf{r}', \quad (2-39)$$

$$V_{\alpha\beta}[\{\rho\}] = q_{\alpha} q_{\beta} \iint \frac{\rho_{\alpha\beta}(\mathbf{r}, \mathbf{r}')}{|\mathbf{r} - \mathbf{r}'|} d\mathbf{r} d\mathbf{r}'. \quad (2-40)$$

Therefore, we can rewrite  $E^{xc}$ ,

$$\begin{aligned}
E^{xc}[\{\rho\}] &= \sum_{\alpha}^{N_q} \frac{q_{\alpha}^2}{2} \iint \frac{\rho_{\alpha\alpha}(\mathbf{r}, \mathbf{r}') - \rho_{\alpha}(\mathbf{r})\rho_{\alpha}(\mathbf{r}')}{|\mathbf{r} - \mathbf{r}'|} d\mathbf{r}d\mathbf{r}' + \\
&\quad \sum_{\beta>\alpha}^{N_q} q_{\alpha}q_{\beta} \iint \frac{\rho_{\alpha\beta}(\mathbf{r}, \mathbf{r}') - \rho_{\alpha}(\mathbf{r})\rho_{\beta}(\mathbf{r}')}{|\mathbf{r} - \mathbf{r}'|} d\mathbf{r}d\mathbf{r}' \\
&= \sum_{\alpha}^{N_q} E_{\alpha}^{xc}[\rho_{\alpha}] + \sum_{\beta>\alpha}^{N_q} E_{\alpha\beta}^c[\rho_{\alpha}, \rho_{\beta}], \tag{2-41}
\end{aligned}$$

where we defined exchange-correlation functionals for each species,  $E_{\alpha}^{xc}$ , and correlation functionals for pairs of species,  $E_{\alpha\beta}^c$ .

Many exchange correlation functionals for electrons,  $E_e^{xc}$ , have been developed during the last forty years for regular electronic structure calculations [83]. These functionals can be used in APMO calculations. On the other hand, it has been shown that nuclear exchange and correlation contributions are negligible [46, 48, 49, 84], Therefore, as nuclear exchange correlation functional,  $E_n^{xc}$ , we only have to include a term to cancel self-repulsion [85]. For a system with  $N_m$  distinguishable nuclei:

$$E_n^{sr} = - \sum_m^{N_m} \sum_{\mu\nu\sigma\tau}^{B_m} q_m^2 P_{m\mu\nu} P_{m\sigma\tau} (\theta_{m\mu}\theta_{m\nu} | \theta_{m\sigma}\theta_{m\tau}). \tag{2-42}$$

Correlation functionals between pairs of species, for example, nuclear-electron correlation functionals, have been rarely investigated. We summarize some of these studies in section 2.2.3.

## 2.2.2 APMO/HF exchange functional

In the APMO/HF method, the wavefunction is constructed as a product of Slater determinats of spin-orbitals for fermionic species, and symmetric products of spin-orbitals for bosonic species. We represent them as  $\Phi$ . [42, 43, 45, 61]

$$\Psi^{HF}(\{\mathbf{r}\}) = \prod_{\alpha}^{N_q} \Phi_{\alpha}(\{\mathbf{r}_{\alpha}\}). \tag{2-43}$$

From this definition it clearly follows that  $\rho_{\alpha\beta}(\mathbf{r}, \mathbf{r}') = \rho_{\alpha}(\mathbf{r})\rho_{\beta}(\mathbf{r}')$ . Therefore at the HF level there is no correlation between particles of different species,  $E_{\alpha\beta}^c = 0$ . The Coulomb interaction expression for particles of the same species is well known from regular electronic structure [86]

$$V_{\alpha\alpha}[\{\rho\}] = J_{\alpha\alpha}[\rho_{\alpha}] + K_{\alpha\alpha}[\rho_{\alpha}], \tag{2-44}$$

$$K_{\alpha\alpha}[\rho_{\alpha}] = \pm q_{\alpha}^2 \sum_{j>i}^{N_{\alpha}} \langle \chi_i \chi_j | \chi_j \chi_i \rangle, \tag{2-45}$$

where the exchange is positive for bosons and negative for fermions. Note that  $K_{\alpha\alpha}$  cannot be written explicitly in terms of the density, but it is related to it as it depends on the reference orbitals. We conclude that at the HF level,  $E^{xc}$  only contains exchange operators,

$$E^{xc}[\{\rho\}] = \sum_{\alpha}^{N_q} K_{\alpha\alpha}[\rho_{\alpha}]. \quad (2-46)$$

### 2.2.3 Nuclear-electron correlation functionals

Udagawa and Tachikawa [54] proposed the formulation of an electron-nucleus correlation functional by extension of the Colle-Salvetti (CS) functional to study the interaction between electron and nuclei. Later, Imamura and Nakai [55] reformulated the expression of this functional to remove singular denominators,

$$E_{en}^c[\rho_e, \rho_n] = \int \rho_e(\mathbf{r})\rho_n(\mathbf{r})k(\rho_e)d\mathbf{r}, \quad (2-47)$$

$$k(\rho_e) = \frac{\pi q_n^2 [(24 + (-9 + 2\sqrt{2})\pi)q_n + 4(-4 + \pi)\sqrt{\pi}\beta]}{2\pi\beta^4 \exp[\frac{4q_n(q_n - \sqrt{\pi}\beta)}{\pi\beta^2}]}, \quad (2-48)$$

$$\beta = q\rho_e^{1/3}(\mathbf{r}). \quad (2-49)$$

Where  $q$  is a parameter that depends of  $q_n$ . Values of  $q$  can be found in Ref [55]. This expression and its functional derivatives with respect to the nuclear and electronic density were implemented in the LOWDIN code. We will refer to eq. 2-47 as the CS-type functional. Chakraborty et al. [57] and Sirjoosingh et al. [87] have proposed nuclear-electron correlation functionals based on the pair density of explicitly correlated wavefunctions, as shown in eq. 2-40. Comparing eqs. 2-40 and 2-47, we notice that the evaluation of the former requires numerical integration over six cartesian coordinates, whereas the latter only requires three. It is well known that the computational cost of the numerical integration on a grid grows exponentially with the number of dimensions. Therefore, the evaluation of the functionals presented in Refs. [57, 87] will be limited to very small systems. As a consequence, these functionals have not been implemented in the LOWDIN code.

## 2.3 APMO/DFT proton affinities

As an illustration of the importance of including nuclear-electron correlation in the APMO method, we have performed proton affinities calculations for 15 neutral and anionic atoms and molecules. APMO/DFT calculations were performed including the CS-type functional in APMO/HF calculations. For reference, we also performed APMO/HF and APMO /HF including the APMO/MBPT(2)/HPA nuclear-electron correlation energy calculations (the latter method is discussed in chapter 4) . Dunning's aug-cc-pVTZ [88–90] electronic and Nakai's 5s5p nuclear [43] basis sets were used. Only hydrogen nuclei and electrons were

treated as quantum particles. Proton affinities were calculated as the energy difference of the neutral or anionic species and its protonated form. Results are presented in Table **2-1** along with experimental proton affinities.

Table **2-1** reveals that the inclusion of the CS-type functional in APMO/HF calculations significantly reduces the error in proton affinities: APMO/HF values average deviation from experimental data is 70 kJ/mol, whereas APMO/DFT values deviation is just 25 kJ/mol. APMO/DFT results are even better than APMO/MBPT(2)/HPA ones, as the deviation with the latter method is 42 kJ/mol. Further analysis of results presented in table **2-1** shows that APMO/HF and APMO/MBPT(2)/HPA methods underestimate proton affinities, whereas APMO/DFT tends to overestimate them.

It should be noted that in the calculation of these proton affinities we have not included electronic correlation nor thermal corrections. Inclusion of these effects in the APMO calculations may reduce the deviation from the experimental results. Nevertheless, these effects are smaller than the NQEs arising from the nuclear (vibrational) zero point energies in protonation reactions. Therefore, the trends discussed above will also be observed in more elaborate calculations including those effects.

Results presented in this section confirm that the inclusion of nuclear-electron correlation improves the accuracy of the NQEs predicted with the APMO method.

**Table 2-1:** Comparison of APMO/HF, APMO/MBPT(2)/HPA, APMO/DFT and experimental proton affinities. Energies in kJ/mol

System	APMO proton affinities				APMO deviations from exp.		
	exp <sup>a</sup>	HF	MBPT(2)/HPA <sup>b</sup>	DFT <sup>c</sup>	HF	MBPT(2)/HPA	DFT
Ne	201	141	162	232	-60	-39	31
Ar	371	292	318	383	-79	-53	12
H <sub>2</sub>	424	368	389	460	-56	-35	36
HF	490	438	460	529	-52	-30	39
H <sub>2</sub> O	697	651	675	742	-46	-22	45
SH <sub>2</sub>	712	642	671	732	-70	-41	20
NH <sub>3</sub>	854	812	839	902	-42	-15	48
Br <sup>-</sup>	1354	1265	1295	1354	-89	-59	0
Cl <sup>-</sup>	1395	1301	1332	1390	-94	-63	-5
CN <sup>-</sup>	1477	1377	1410	1465	-100	-67	-12
SH <sup>-</sup>	1477	1388	1420	1477	-89	-57	0
F <sup>-</sup>	1554	1497	1530	1586	-57	-24	32
OH <sup>-</sup>	1635	1595	1628	1684	-40	-7	49
H <sup>-</sup>	1675	1566	1605	1653	-109	-70	-22
aad <sup>d</sup>					70	42	25

<sup>a</sup> Experimental values were taken from Ref. [91]

<sup>b</sup> In APMO/MBPT(2) calculations only nuclear-electron correlation was included

<sup>c</sup> APMO/DFT corresponds to APMO/HF calculations including the CS-type functional

<sup>d</sup> Average absolute deviation

## 3 APMO Calculations with Cubic Scaling

In this chapter we present a methodology to reduce the computational cost of APMO/DFT calculations from quartic to cubic, by introducing an auxiliary density.

Most of the NMO schemes discussed in chapter 1 employ localized GTFs to construct electronic and nuclear molecular orbitals. As a result, their scaling with respect to the total basis set size (electronic and nuclear) is identical to that of BOA methods of the same level of theory. For instance, for NMO/HF and NMO/DFT formal scalings will remain quartic. As a consequence of this scaling behavior, investigation of NQE on large systems with NMO methods will turn unmanageable, e.g. in solvation phenomena studies [92].

In this regard, several strategies have been devised to reduce the computational effort of NMO calculations. For instance, significant savings can be obtained by dividing the nuclei of a molecular system into two types: classical (treated as point charges) and quantum nuclei. Additional savings can be achieved by representing the nuclear wave function of a system with multiple protons, as a localized Hartree product rather than a Slater determinant [43, 85]. The use of this Hartree product approximation (HPA) of the nuclear wavefunction leads to reductions from quartic to linear scaling with respect to the number of nuclei [85]. Still, the scaling with respect to electronic basis size remains quartic and consequently, the global scaling of NMO/HF and NMO/DFT methods remains quartic. Thus, if calculations on large systems want to be performed further improvements on efficiency are desired. These improvements must focus first on reducing their scaling with respect to the electronic basis set size.

For DFT, faster electronic Kohn-Sham based approaches have been developed by using the variational approximation of the Coulomb potential [75–79]. By introducing an auxiliary density, four-index integrals are avoided, and only one-, two- and three-center electron repulsion integrals are calculated. This results in a formal cubic scaling with respect to the electronic basis set size. When the auxiliary density is used in the calculation of the exchange-correlation potential [93–95] the resulting methodology is called auxiliary density functional theory (ADFT) [94].

In this chapter we discuss two methods with cubic scaling based on ADFT: One in which we perform the variation approximation of the Coulomb potential for all species (referred as APMO/ADFT) and one in which we perform that approximation only for light particles (electrons), and we include a localized Hartree product approximation for the heavy particles

(referred as APMO/ADFT/HPA) . APMO/ADFT/HPA results have been published in the Chemical Physics journal [96], and APMO/ADFT results will be submitted to the same journal [97].

This chapter is organized as follows. In section 3.1, we derive the equations of APMO/ADFT and APMO/ADFT/HPA methods. In section 3.2, we discuss some aspects of APMO/ADFT /HPA calculations on systems with quantum electrons and protons. In section 3.3 we discuss some aspects of APMO/ADFT, including the construction of nuclear auxiliary basis sets.

## 3.1 Theory

### 3.1.1 APMO/ADFT Theory

Here we invoke the variational approximation of the Coulomb potential [75–79, 94, 95] for each species. First, we introduce the auxiliary densities  $\{\tilde{\rho}\}$  expanded in terms of an auxiliary basis set, composed of GTFs  $\{\tilde{\phi}_\alpha\}$ ,

$$\tilde{\rho}_\alpha = \sum_k^{A_\alpha} x_{\alpha k} \tilde{\phi}_{\alpha k}, \quad (3-1)$$

where  $A_\alpha$  is the auxiliary function set size and  $\{x_\alpha\}$  is the set of fitting coefficients for  $\alpha$  species. The fitting coefficients are obtained by minimization of the Coulomb energy error [75, 98]:

$$\begin{aligned} \xi_\alpha &= \frac{1}{2} \iint \frac{[\rho_\alpha(\mathbf{r}) - \tilde{\rho}_\alpha(\mathbf{r})][\rho_\alpha(\mathbf{r}') - \tilde{\rho}_\alpha(\mathbf{r}')]}{|\mathbf{r} - \mathbf{r}'|} d\mathbf{r} d\mathbf{r}' \geq 0 \\ &= \frac{1}{2} \sum_{\mu\nu\sigma\tau}^{B_\alpha} P_{\alpha\mu\nu} P_{\alpha\sigma\tau} (\phi_{\alpha\mu} \phi_{\alpha\nu} | \phi_{\alpha\sigma} \phi_{\alpha\tau}) - \sum_k^{A_\alpha} \sum_{\mu\nu}^{B_\alpha} P_{\alpha\mu\nu} x_{\alpha k} (\phi_{\alpha\mu} \phi_{\alpha\nu} | \tilde{\phi}_{\alpha k}) \\ &\quad + \frac{1}{2} \sum_{kl}^{A_\alpha} x_{\alpha k} x_{\alpha l} (\tilde{\phi}_{\alpha k} | \tilde{\phi}_{\alpha l}). \end{aligned} \quad (3-2)$$

Finding the extrema of  $\xi_\alpha$  with respect to  $\{x_\alpha\}$  leads to,

$$\sum_{\mu\nu}^{B_\alpha} P_{\alpha\mu\nu} (\phi_{\alpha\mu} \phi_{\alpha\nu} | \tilde{\phi}_{\alpha k}) = \sum_l^{A_\alpha} x_{\alpha l} (\tilde{\phi}_{\alpha k} | \tilde{\phi}_{\alpha l}). \quad (3-3)$$

Defining the elements of the Coulomb matrix  $\tilde{\mathbf{G}}_\alpha$  and the Coulomb vector  $\tilde{\mathbf{J}}_\alpha$  [94, 99] as,

$$\tilde{G}_{\alpha kl} = (\tilde{\phi}_{\alpha k} | \tilde{\phi}_{\alpha l}), \quad (3-4)$$

$$\tilde{J}_{\alpha k} = \sum_{\mu\nu} P_{\alpha\mu\nu} (\phi_{\alpha\mu}^\alpha \phi_{\alpha\nu}^\alpha | \tilde{\phi}_{\alpha k}). \quad (3-5)$$

A linear equation system for the determination of the fitting coefficients vector,  $\mathbf{x}_\alpha$ , can be formulated as

$$\begin{aligned}\tilde{\mathbf{G}}_\alpha \mathbf{x}_\alpha &= \tilde{\mathbf{J}}_\alpha, \\ \mathbf{x}_\alpha &= \tilde{\mathbf{G}}_\alpha^{-1} \tilde{\mathbf{J}}_\alpha.\end{aligned}\quad (3-6)$$

Because the Coulomb energy error (Eq. 3-2) is positive definite the following inequality holds,

$$\sum_{\mu\nu\sigma\tau}^{B_\alpha} P_{\alpha\mu\nu} P_{\alpha\sigma\tau} (\phi_{\alpha\mu} \phi_{\alpha\nu} | \phi_{\alpha\sigma} \phi_{\alpha\tau}) \geq 2 \sum_k^{A_\alpha} \sum_{\mu\nu}^{B_\alpha} P_{\alpha\mu\nu} x_{\alpha k} (\phi_{\alpha\mu} \phi_{\alpha\nu} | \tilde{\phi}_{\alpha k}) - \sum_{kl}^{A_\alpha} x_{\alpha k} x_{\alpha l} (\tilde{\phi}_{\alpha k} | \tilde{\phi}_{\alpha l}). \quad (3-7)$$

Using the approximate densities the interspecies interaction term can be estimated,

$$\sum_{\mu\nu}^{B_\alpha} \sum_{\sigma\tau}^{B_\beta} P_{\alpha\mu\nu} P_{\beta\sigma\tau} (\phi_{\alpha\mu} \phi_{\alpha\nu} | \phi_{\beta\sigma} \phi_{\beta\tau}) \approx \sum_k^{A_\alpha} \sum_l^{A_\beta} x_{\alpha k} x_{\beta l} (\tilde{\phi}_{\alpha k} | \tilde{\phi}_{\beta l}). \quad (3-8)$$

Substitution of the density by its approximated form in the evaluation of the exchange-correlation functionals yields the final APMO-ADFT energy expression,

$$\begin{aligned}E[\{\rho\}] &\approx \sum_\alpha^{N_q} \sum_{\mu\nu}^{B_\alpha} P_{\alpha\mu\nu} H_{\alpha\mu\nu} + \frac{1}{2} \sum_\alpha^{N_q} \sum_{\beta \neq \alpha}^{N_q} q_\alpha q_\beta \sum_k^{A_\alpha} \sum_l^{A_\beta} x_{\alpha k} x_{\beta l} (\tilde{\phi}_{\alpha k} | \tilde{\phi}_{\beta l}) + E^{xc}[\{\tilde{\rho}\}] \\ &+ \sum_\alpha^{N_q} q_\alpha^2 \left( \sum_k^{A_\alpha} \sum_{\mu\nu}^{B_\alpha} P_{\alpha\mu\nu} x_{\alpha k} (\phi_{\alpha\mu} \phi_{\alpha\nu} | \tilde{\phi}_{\alpha k}) - \frac{1}{2} \sum_{kl}^{A_\alpha} x_{\alpha k} x_{\alpha l} (\tilde{\phi}_{\alpha k} | \tilde{\phi}_{\alpha l}) \right).\end{aligned}\quad (3-9)$$

Elements of the Kohn-Sham matrices are obtained deriving this energy expression with respect to density matrices elements. The two particles, coupling and exchange-correlation matrices can be defined in terms of the auxiliary densities as well,

$$G_{\alpha\mu\nu} = q_\alpha^2 \sum_k^{A_\alpha} x_{\alpha k} (\phi_{\alpha\mu} \phi_{\alpha\nu} | \tilde{\phi}_{\alpha k}), \quad (3-10)$$

$$I_{\alpha\mu\nu} = \sum_{\beta \neq \alpha}^{N_q} q_\alpha q_\beta \sum_{km}^{A_\alpha} \sum_l^{A_\beta} G_{\alpha km}^{-1} (\phi_{\alpha\mu} \phi_{\alpha\nu} | \tilde{\phi}_{\alpha m}) x_{\beta l} (\tilde{\phi}_{\alpha k} | \tilde{\phi}_{\beta l}), \quad (3-11)$$

$$V_{\alpha\mu\nu}^{xc} = \sum_{kl}^{A_\alpha} G_{\alpha kl}^{-1} (\phi_{\alpha\mu} \phi_{\alpha\nu} | \tilde{\phi}_{\alpha k}) \langle \tilde{\phi}_{\alpha l} | V_\alpha^{xc}[\{\tilde{\rho}\}] \rangle, \quad (3-12)$$

$$\langle \tilde{\phi}_{\alpha l} | V_\alpha^{xc}[\{\rho\}] \rangle = \int \tilde{\phi}_{\alpha l}(\mathbf{r}) V_\alpha^{xc}[\{\tilde{\rho}\}](\mathbf{r}) d\mathbf{r}. \quad (3-13)$$

With these elements, Kohn-Sham matrices are built (Eq. 2-30), and with those matrices, Eqs. 2-28 are solved iteratively for each species.

### 3.1.2 APMO/ADFT/HPA method

In an APMO/DFT calculation, heavy particles (nuclei, muons) can be assumed to be distinguishable, in a similar fashion as in the APMO/HF/HPA and APMO/MBPT(2)/HPA methods discussed in sections 4.1.3 and 4.1.4. If localized basis sets are used to build the heavy particle reference orbitals, only the calculation of the light particles (electrons)  $\mathbf{G}_e$  matrix will remain as a quartic-scaling process with respect to the basis set size,  $B_e$ . To reduce the scaling of this process to cubic we invoke the variational approximation of the Coulomb potential discussed above only for electrons. We will refer to this method as the APMO/ADFT/HPA. For a system composed of  $N_e$  electrons and  $N_m$  distinguishable heavy particles, the APMO/ADFT/HPA energy expression is,

$$\begin{aligned}
E[\{\rho\}] \approx & \sum_{\mu\nu}^{B_e} P_{e\mu\nu} H_{e\mu\nu} + \sum_m^{N_m} \sum_{\mu\nu}^{B_m} P_{m\mu\nu} H_{m\mu\nu} + \sum_k^{A_e} \sum_{\mu\nu}^{B_e} P_{e\mu\nu} x_{ek} (\theta_{e\mu} \theta_{e\nu} | \tilde{\theta}_{ek}) \\
& - \frac{1}{2} \sum_{kl}^{A_e} x_{ek} x_{el} (\tilde{\theta}_{ek} | \tilde{\theta}_{el}) - \sum_m^{N_m} \sum_{\mu\nu}^{B_e} \sum_{\sigma\tau}^{B_m} q_m P_{e\mu\nu} P_{m\sigma\tau} (\theta_{e\mu} \theta_{e\nu} | \theta_{m\sigma} \theta_{m\tau}) \\
& + \sum_{m' > m}^{N_m} \sum_{\mu\nu}^{B_m} \sum_{\sigma\tau}^{B_{m'}} q_m q_{m'} P_{m\mu\nu} P_{m'\sigma\tau} (\theta_{m\mu} \theta_{m\nu} | \theta_{m'\sigma} \theta_{m'\tau}) + E^{xc}[\tilde{\rho}_e, \{\rho_m\}]. \tag{3-14}
\end{aligned}$$

Elements of the two particles, coupling and exchange correlation matrices elements are

$$G_{e\mu\nu} = \sum_k^{A_e} x_{ek} (\phi_{e\mu} \phi_{e\nu} | \tilde{\phi}_{ek}), \tag{3-15}$$

$$I_{e\mu\nu} = - \sum_m^{N_m} q_m \sum_{\sigma\tau}^{B_m} P_{m\sigma\tau} (\phi_{e\mu} \phi_{e\nu} | \phi_{m\sigma} \phi_{m\tau}), \tag{3-16}$$

$$V_{e\mu\nu}^{xc} = \sum_{kl}^{A_e} G_{ekl}^{-1} (\phi_{e\mu} \phi_{e\nu} | \tilde{\phi}_{ek}) \langle \tilde{\phi}_{el} | V_e^{xc}[\{\tilde{\rho}\}] \rangle, \tag{3-17}$$

$$G_{m\mu\nu} = q_m^2 \sum_{\sigma\tau}^{B_m} P_{m\sigma\tau} (\phi_{m\mu} \phi_{m\nu} | \phi_{m\sigma} \phi_{m\tau}), \tag{3-18}$$

$$I_{m\mu\nu} = -q_m \sum_{\sigma\tau}^{B_e} P_{e\sigma\tau} (\phi_{m\mu} \phi_{m\nu} | \phi_{e\sigma} \phi_{e\tau}) + \sum_{m' \neq m}^{N_m} q_m q_{m'} \sum_{\sigma\tau}^{B_{m'}} P_{m'\sigma\tau} (\phi_{m\mu} \phi_{m\nu} | \phi_{m'\sigma} \phi_{m'\tau}), \tag{3-19}$$

$$V_{m\mu\nu}^{xc} = \langle \phi_{m\mu} | V_m^{xc}[\tilde{\rho}_e, \{\rho_m\}] | \phi_{m\nu} \rangle. \tag{3-20}$$

With these elements, Kohn-Sham matrices are built (Eq. 2-30), and with those matrices, Eqs. 2-28 are solved iteratively for each species.

When compared to the APMO/ADFT, with the HPA we avoid including auxiliary densities for the heavy species.

In the next section we discuss some basic aspects of APMO/ADFT/HPA calculations.

## 3.2 APMO/ADFT/HPA calculations

In this section we discuss the results for APMO/ADFT/HPA calculations on systems with quantum electrons and protons, neglecting nuclear-electron correlation and nuclear exchange and correlation. A nuclear functional is included to cancel self-repulsion (Eq. 2-42). The exchange correlation functional used in these calculations is,

$$E^{xc}[\{\rho\}] = E_e^x[\tilde{\rho}_e] + E_e^c[\tilde{\rho}_e] + E_n^{sr}[\rho_n]. \quad (3-21)$$

In all calculations the electronic Slater-Dirac exchange [100, 101] and Vosko-Wilk-Nusair correlation [102] functionals were used. All calculations considered hydrogen nuclei as quantum particles and heavier nuclei as point charges. Calculations to test the numerical accuracy of the APMO/ADFT/HPA method were performed with the electronic 6-311++G\*\* [103] and nuclear DZSPD [45] basis sets. Calculations to test the scaling behavior of the APMO/ADFT/HPA method were performed with electronic 6-31G [104] and nuclear DZSP basis sets [45]. Primitive cartesian GTFs were employed as auxiliary function set. Auxiliary exponents were generated using the GEN-A2\* [105] algorithm. Numerical integration of exchange-correlation potential and energy were performed employing a (75,302) fixed grid. Hydrogen bond-lengths were calculated as expectation values of  $\langle R_H \rangle$ . Integral screening and asymptotic repulsion integral expansions were not employed in our calculations, for observed and formal scaling to be as close as possible. All calculations were performed on a workstation with a Pentium(R) Dual-Core (2.93GHz) CPU and 4.0 GB of RAM.

### 3.2.1 APMO/ADFT/HPA numerical accuracy

The impact of the approximations introduced in APMO/ADFT/HPA on total energies, atomization energies and bond lengths was estimated by comparing APMO/DFT and APMO/ADFT/HPA calculations for HF, H<sub>2</sub>O, NH<sub>3</sub>, CH<sub>4</sub> and FHF<sup>-</sup>. Results are summarized in Table 3-1.

A first analysis of total energies,  $E$ , exposes that APMO/ADFT/HPA results differ at most by 3 mHartree from APMO/DFT for these molecules. For atomization energies, AE, this analysis reveals good agreement between APMO/ADFT/HPA and APMO/DFT results, displaying deviations of less than 1.5 kcal/mol. As to optimized geometries, heavy and hydrogen nuclei average distances differ by less than 0.01 Å.

The magnitudes of the deviations in energies and geometries observed in Table 3-1 are similar to those obtained in electronic structure ADFT [78, 94]. This analysis suggests that the introduction of an approximated electronic density will not significantly impact the physical description of the molecule and consequently the quality of APMO/ADFT calculations.

**Table 3-1:** APMO/DFT and APMO/ADFT/HPA total energies ( $E$ ), atomization energies (AE) and average bond-lengths ( $R_{X-H}$ ).

Molecule	Method	$E/\text{a.u.}$	AE/ kcal mol $^{-1}$	$R_{X-H}/\text{\AA}$
HF	APMO/DFT	-99.7954	-156.8	0.949
	APMO/ADFT/HPA	-99.7965	-157.1	0.952
H <sub>2</sub> O	APMO/DFT	-75.8189	-255.4	0.988
	APMO/ADFT/HPA	-75.8191	-255.2	0.989
NH <sub>3</sub>	APMO/DFT	-55.9773	-320.1	1.037
	APMO/ADFT/HPA	-55.9801	-321.6	1.038
CH <sub>4</sub>	APMO/DFT	-39.9561	-444.3	1.124
	APMO/ADFT/HPA	-39.9549	-443.3	1.117
FHF <sup>-</sup>	APMO/DFT	-199.1385	-309.3	1.164
	APMO/ADFT/HPA	-199.1401	-309.5	1.160

All calculations were performed with the [6-311++G\*:DZSPD] electronic:nuclear basis sets

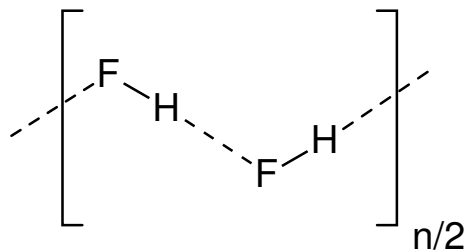


**Figure 3-1:** Schematic representation of the  $(\text{HF})_n$  chains.

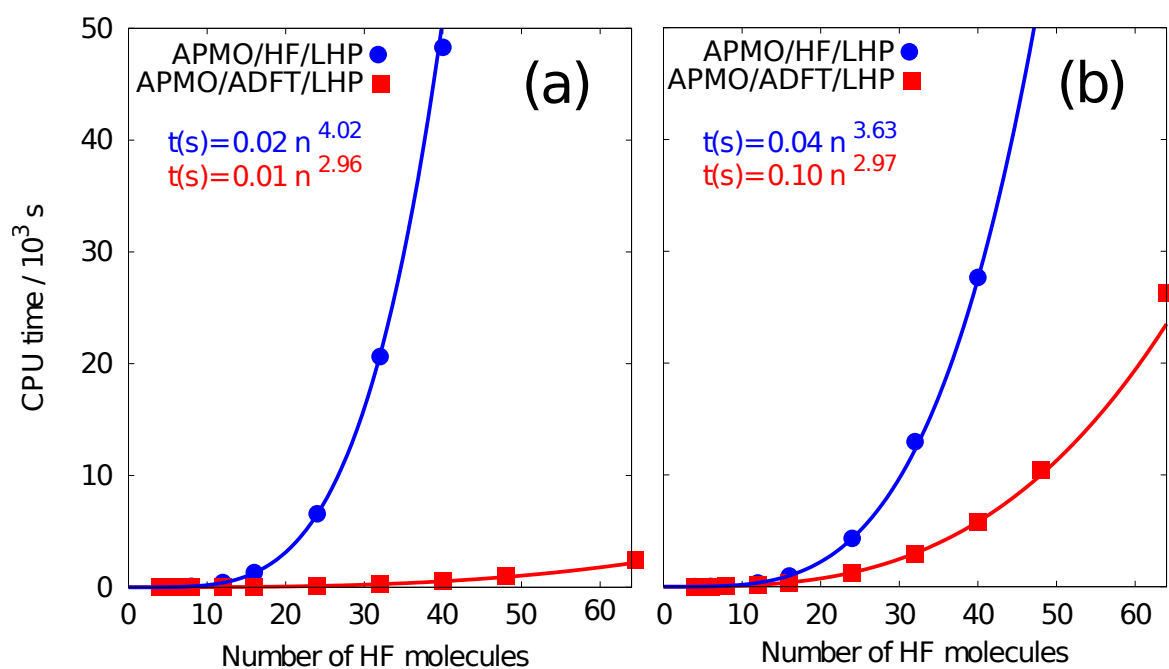


**Figure 3-2:** Comparison of APMO/ADFT/HPA and APMO/HF/HPA calculation times for  $(\text{HF})_n$  chains. (a) Electronic Coulomb integral calculation times. (b) Total time per SCF cycle. Calculations were performed with the [6-31G:DZSP] electronic:nuclear basis sets.

### 3.2.2 APMO/ADFT/HPA scaling

Single-point calculations were performed on  $(\text{HF})_n$  chains ( $n=2-64$ ) (Figure 3-1) to test the scaling order of the APMO/ADFT/HPA method with respect to the size of the system. APMO/HF/HPA calculations were also performed for reference. APMO/HF/HPA is expected to be slightly faster than APMO/DFT and therefore it provides a lower bound to APMO/DFT timing.

In Figure 3-2(a) we plot the time employed by APMO/ADFT/HPA and APMO/HF/HPA methods in the calculation of electronic Coulomb integrals for  $(\text{HF})_n$  chains. In all cases considered APMO/ADFT/HPA outperforms APMO/HF/HPA. This figure clearly exposes that savings in computational time reached by APMO/ADFT/HPA increase dramatically with system size. For instance, in the  $(\text{HF})_{40}$  chain calculation a speedup of 90x is obtained. As observed in Figure 3-2(a) APMO/ADFT/HPA and HF/HPA report scaling orders of 2.96 and 4.02 with respect to the number of HF molecules. In APMO/ADFT/HPA calculations this scaling is achieved by using a variational fitting of the Coulomb potential.

In Figure 3-2(b) we compare the CPU time per single SCF cycle. Here APMO/ADFT/HPA and APMO/HF/HPA scaling orders were 2.97 and 3.63 with respect to the number of HF molecules. Although the scaling of APMO/ADFT/HPA is similar in Figures 3-2(a) and 3-2(b) its prefactor is ten times larger in the SCF cycle. This difference can be understood considering that 3-center integrals are called twice in each SCF cycle. First, to obtain the fitting coefficients (Eq. 3-6) and second to build the Kohn-Sham matrix (Eq. 3-10). In addition, each SCF involves several matrix manipulations with cubic scaling including 3-D numerical integration.

The results presented so far suggest that average deviations from experimental results are expected to be of the same order for APMO/DFT and APMO/ADFT/HPA. However, to the best of our knowledge the APMO/ADFT/HPA methodology proposed in this work outperforms all previous formulations of NMO/DFT. This development unfolds new possibilities of studying nuclear quantum effects in much larger systems, for instance solvation phenomena of chemical and biological interest.

## 3.3 APMO/ADFT calculations

In this section we discuss the results for APMO/ADFT calculations on systems with quantum electrons and nuclei including nuclear-electron correlation. A nuclear functional is included to cancel self-repulsion (Eq. 2-42). The exchange correlation functional used in these calculations is,

$$E^{xc}[\{\rho\}] = E_e^x[\tilde{\rho}_e] + E_e^c[\tilde{\rho}_e] + E_{en}^c[\tilde{\rho}_e, \tilde{\rho}_n] + E_n^{sr}[\rho_n]. \quad (3-22)$$

Nakai's Colle-Salvetti nuclear-electron correlation functional was employed [55] (Eq. 2-47). Unless otherwise noted, in all calculations the electronic Slater-Dirac exchange [100, 101] and

Vosko-Wilk-Nusair correlation [102] functionals were used. Auxiliary electronic exponents were generated using the GEN-A2\* algorithm [105]. Dunning’s cc-pVTZ [88–90] electronic basis and Nakai’s 7s7p7d [43] nuclear basis were used.

### 3.3.1 Building auxiliary basis sets

We have proposed an algorithm for the generation of nuclear auxiliary basis functions based on the GEN- $A_n$  algorithm for the generation of electronic auxiliary functions [105]. The number of exponents is given by:

$$N_{exp} = \text{int} \left( \frac{\ln(\varsigma_{max})/\ln(\varsigma_{min})}{(6-n)} + 0.5 + \Delta M \right), \quad (3-23)$$

where  $\varsigma$  is a nuclear basis exponent and  $\Delta M$  is an additional parameter to increase the number of auxiliary functions. The exponents of the auxiliary GTFs are generated by an even tempered scheme. We used in this calculations  $n = 2$ .

To evaluate the quality of the nuclear auxiliary basis set we calculated the integral of the auxiliary density and compared it to the number of nuclei using the ratio,

$$\frac{\tilde{N}_n}{N_n} = \frac{\int \tilde{\rho}_n(\mathbf{r}) d\mathbf{r}}{N_n}. \quad (3-24)$$

The closer this ratio is to one, the better the auxiliary density is.

In figure **3-3** we present  $\frac{\tilde{N}_n}{N_n}$  for some diatomic systems as a function of the increment in the auxiliary basis set size. This figure reveals that for quantum nuclei the number of particles obtained from the auxiliary density is very different from the integer expected value when  $\Delta M$  is lower than four. When we increase the number of auxiliary functions in four functions, the number of particles obtained from the auxiliary density is very close to the integer value expected.

In figure **3-4** is plotted the relative change of the nuclear-electronic energy with respect the nuclear auxiliary basis size for some diatomic systems. The change in energy is calculated as the ratio of the correlation energy and the correlation energy obtained with the largest auxiliary basis used. This figure reveals that convergence is obtained when four additional basis functions are included. For instance, for the  $F_2$  molecule the correlation energy with four additional basis functions is only 1.008 times greater than the obtained with seven auxiliary functions.

From these results we can conclude that four additional nuclear auxiliary basis functions are required when APMO/ADFT calculations are performed.

### 3.3.2 APMO/ADFT scaling

Single-point calculations were performed on  $(HF)_n$  chains (Figure **3-1**) to test scaling order of APMO/ADFT with respect to the size of system including the calculation of CS-type

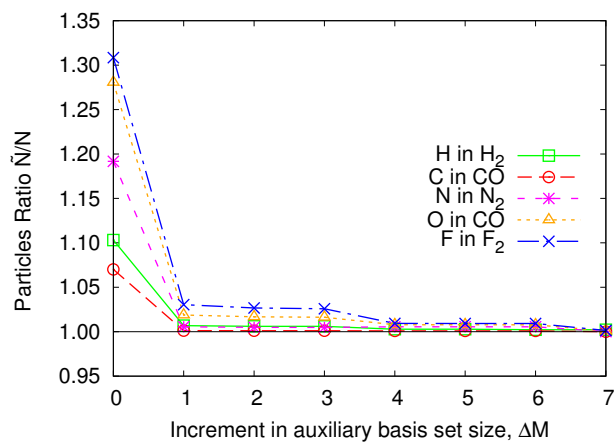


**Figure 3-3:** Ratio of the number of particles obtained from the auxiliary density and the number of nuclei in function of the auxiliary basis set size

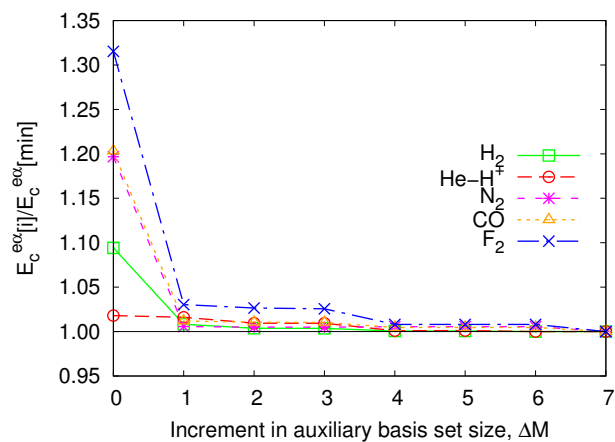


**Figure 3-4:** Convergence of the nuclear-electronic correlation energy

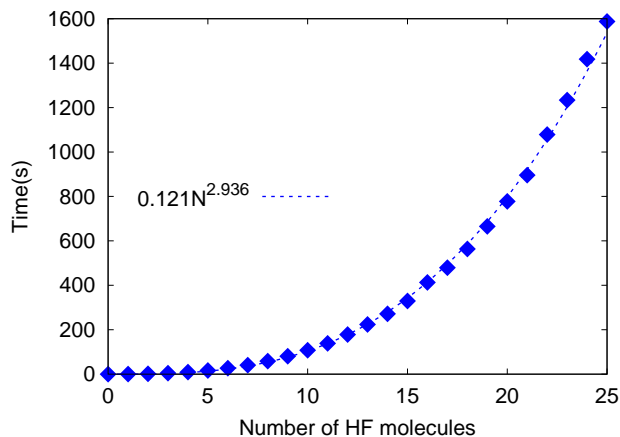


**Figure 3-5:** APMO/ADFT total time per SCF cycle using for  $(\text{HF})_n$  chains including a nuclear-electronic correlation functional.

nuclear-electronic correlation functional. In these calculations, F nuclei were treated as point charges. Electronic 6-31G [104] and nuclear DZSP basis sets [45] were used.

In Figure 3-5 we plot the APMO/ADFT total time per SCF cycle elapsed in the calculation of  $(\text{HF})_n$  chains from  $n=2$  to  $n=25$ . This figure reveals the scaling of the APMO/ADFT method including the CS-type nuclear-electronic correlation functional is cubic. The fact that APMO/ADFT calculations present cubic scaling will allow the evaluation of the impact of nuclear-electron correlation in much larger systems than other methods based on wavefunctions, such as APMO/MBPT(2).

### 3.3.3 APMO/ADFT numerical accuracy

We have evaluated the impact of the use of the nuclear and electronic auxiliary densities in the evaluation of the nuclear-electron correlation energy comparing our APMO/ADFT results with those of Imamura and Nakai [55]. These calculations were performed by including the Colle-Salvetti nuclear-electron correlation functional (eq. 2-47) in APMO/HF calculations, to reproduce Imamura and Nakai's procedure. Table 3-2 presents these results.

Our APMO/ADFT nuclear-electronic correlation energies are 5 to 6% larger than the values reported in Ref. [55], regardless of the nucleus type. These differences arise from the use of the nuclear and electronic auxiliary densities in the evaluation of eq. 2-47.

However, we should note that these differences in total energies are not very relevant to chemical applications, because in chemistry we are interested in computing energy differences.

To evaluate the impact of the nuclear and electronic auxiliary densities in chemical properties, we have performed APMO/DFT and APMO/ADFT calculations of proton affinities for 15 atoms and molecules. These calculations were performed by including the CS-type

**Table 3-2:** Comparison of nuclear-electronic correlation energy obtained with APMO/ADFT and Ref. [55] results.

System	Ref. [55]	APMO/ADFT	% Error
LiH	-0.1968	-0.2068	5.1
BeH	-0.3015	-0.3180	5.5
Li <sub>2</sub>	-0.3254	-0.3425	5.3
HF	-1.0307	-1.0901	5.8
N <sub>2</sub>	-1.3824	-1.4813	7.2
CO	-1.3949	-1.4839	6.4
F <sub>2</sub>	-1.9935	-2.1043	5.6
H <sub>2</sub> O	-0.9199	-0.9620	4.6

functional in APMO/HF calculations. The only difference between these APMO/DFT and APMO/ADFT calculations is that in the former the exact density was used in the evaluation of the CS-type functional whereas in the latter the auxiliary density was used. Dunning’s aug-cc-pVTZ [88–90] electronic and Nakai’s 5s5p nuclear [43] basis sets were used. Only hydrogen nuclei and electrons were treated as quantum particles. Proton affinities were calculated as the energy difference of the neutral or anionic species and their protonated forms. Results are presented in Table **3-3**.

Table **3-3** reveals that the calculates proton affinities with APMO/DFT and APMO/ADFT are in excellent agreement. In average the difference between the APMO/DFT and APMO/ADFT proton affinities is 1.2 kJ/mol. This analysis suggests that the introduction of approximated electronic and nuclear densities in the calculation of the nuclear-electron correlation energy does not significantly impact the physical description of the molecule and consequently the quality of the APMO/ADFT calculations.

These results show that APMO/ADFT is a promising methodology to include nuclear-electronic correlation with cubic scaling, which allows the study of NQEs in medium sized systems. Currently, we are working in the development and implementation of more accurate nuclear-electron correlation functionals. We expect that with the right functional APMO/ADFT results will be as accurate as multicomponent full-CI [51] or explicitly correlated methods [53, 106].

**Table 3-3:** Comparison of APMO/DFT and APMO/ADFT proton affinities (in kJ/mol)

System	APMO/DFT	APMO/ADFT	diff
Ne	232	231	-2
Ar	383	384	1
H <sub>2</sub>	460	465	4
HF	529	529	0
H <sub>2</sub> O	732	734	1
SH <sub>2</sub>	742	743	1
NH <sub>3</sub>	902	903	2
Br <sup>-</sup>	1354	1355	1
Cl <sup>-</sup>	1390	1391	1
CN <sup>-</sup>	1465	1466	1
SH <sup>-</sup>	1477	1478	1
F <sup>-</sup>	1586	1586	0
OH <sup>-</sup>	1653	1654	1
H <sup>-</sup>	1684	1685	1

Electrons and protons were considered as quantum particles. [aug-cc-pVTZ:5s5p]  
electronic:nuclear basis sets

# 4 Second-Order Many-Body Perturbation Theory for Any Quantum Particle in the Framework of Hartree Products of Localized Wave Functions

In this chapter we present an alternative APMO/MBPT(2) method, which includes more nuclear-electron and muon-electron correlation energies and has lower scaling than the regular APMO/MBPT(2).

Previous studies have demonstrated that substantial savings in computational effort of NMO/HF calculations can be achieved by representing proton wave function as a Hartree product of localized proton orbitals rather than as a Slater determinant. [43, 85]. These works also revealed that the impact of this nuclear Hartree product approximation (HPA) on the NMO/HF energy is negligible as a consequence of the localized nature of the nuclear orbitals and the small magnitude (of the order of  $10^{-10}$  a.u. [43, 84]) of the nuclear exchange term (which is neglected with the nuclear HPA). Nakai and Sodeyama [46], proposed the use of an independent particle model, which is equivalent to a nuclear HPA, for many-body perturbation theory and coupled cluster NOMO approaches. However, in their paper, neither the formulation of the theory for this model nor its numerical impact on total energies were reported.

We have developed in our groups the APMO method. This approach extends the NMO formalism to any kind of quantum particle. Our aim in this paper is to describe in detail the formulation of a second-order many body perturbation theory (MBPT(2)) for the APMO method, based on a HPA for the heavier quantum species. We will refer to the APMO calculations at HF level including the HPA as APMO/HF/HPA.

Besides the applications of this method to the study of NQEs, we are currently interested in the chemistry of atoms and molecules containing negative muons. This is a result of a series of papers by Fleming and coworkers on the reaction rates for the  ${}^4\text{He}\mu + \text{H}_2 \rightarrow {}^4\text{He}\mu\text{H} + \text{H}$  reaction [35–37]. We have studied the electronic and muonic structure of muonic atoms with the APMO approach at the HF level [38, 39]. In this paper we study the magnitude of the negative muon-electron correlation calculated at the MBPT(2) level.

Throughout the text APMO/HF and APMO/HF/HPA will refer to the regular APMO Hartree-Fock and the APMO HF method including HPA respectively. The MBPT(2) meth-

ods derived from these two methods will be denoted as APMO/MBPT(2) and APMO/MBPT(2)/HPA respectively. The APMO/HF/HPA and APMO/MBPT(2)/HPA equations were implemented on the LOWDIN program [80].

An outline of the chapter is as follows. In section 4.1 we summarize the APMO/HF, APMO/HF/HPA, APMO/MBPT(2) and APMO/MBPT(2)/HPA methods. In section 4.2, we discuss some aspects of the computational implementation. In sections 4.3 and 4.4 we present some applications of the APMO/MBPT(2)/HPA approach to several model systems to assess numerically its accuracy and computational efficiency respectively. In section 4.5 we present the applications of the APMO/MBPT(2)/HPA approach to study muon-electron correlation. In section 4.6 we propose a nuclear-electron correlation functional based on APMO/MBPT(2)/HPA results.

Results presented in this chapter have been submitted for publication in the Molecular Physics journal [40]

## 4.1 APMO/MBPT(2) Theory

We first highlight some APMO/HF [42, 43, 45, 61], APMO/MBPT(2) [47, 48, 63] and APMO/HF/HPA [85] expressions. We then derive the expressions of APMO/MBPT(2)/HPA method. For simplicity in this section we assume that all quantum particles are fermions [84].

### 4.1.1 APMO/HF theory

These equations can be thought as a subset of the APMO/DFT equations presented in section 2.1, where the exchange-correlation functional is composed only of the Fock exchange functionals, as presented in subsection 2.2.2. It is relevant to this section to take into account that at the APMO/HF level the eigenvalues for occupied orbitals are

$$\varepsilon_{\alpha\alpha} = \langle a_\alpha | h | a_\alpha \rangle + \sum_{b^\alpha \neq a^\alpha}^{N_\alpha} q_\alpha^2 \langle a_\alpha b_\alpha | | a_\alpha b_\alpha \rangle + \sum_{\beta}^{N_{types}} \sum_{a_\beta}^{N_\beta} q_\alpha q_\beta \langle a_\alpha a_\beta | a_\alpha a_\beta \rangle, \quad (4-1)$$

and the eigenvalues for virtual orbitals are

$$\varepsilon_{\alpha r} = \langle r_\alpha | h | r_\alpha \rangle + \sum_{a_\alpha}^{N_\alpha} q_\alpha^2 \langle r_\alpha a_\alpha | | r_\alpha a_\alpha \rangle + \sum_{\beta}^{N_{types}} \sum_{a_\beta}^{N_\beta} q_\alpha q_\beta \langle r_\alpha a_\beta | r_\alpha a_\beta \rangle, \quad (4-2)$$

here  $\{a_\alpha, b_\alpha\}$  and  $\{r_\alpha, s_\alpha\}$  are indices for the occupied and virtual molecular orbitals of quantum species  $\alpha$ .

### 4.1.2 APMO/MBPT(2) theory

In this approach [46–49, 63], the reference hamiltonian for the Rayleigh-Schrödinger perturbation theory is

$$H_0 = \sum_{\alpha}^{N_q} \sum_i^{N_{\alpha}} \left[ h_{\alpha}(i) + \sum_j^{N_{\alpha}} q_{\alpha}^2 [J_{\alpha j} - K_{\alpha j}] + \sum_{\beta \neq \alpha}^{N_q} \sum_j^{N_{\beta}} q_{\alpha} q_{\beta} J_{\beta j} \right]. \quad (4-3)$$

The fluctuation operator takes the form:

$$W = \sum_{\alpha}^{N_q} \sum_i^{N_{\alpha}} \left[ \sum_{j>i}^{N_{\alpha}} \frac{q_{\alpha}^2}{r_{ij}} + \sum_{\beta>\alpha}^{N_q} \sum_j^{N_{\beta}} \frac{q_{\alpha} q_{\beta}}{r_{ij}} \right] - \sum_{\alpha}^{N_q} \sum_i^{N_{\alpha}} \left[ \sum_j^{N_{\alpha}} q_{\alpha}^2 [J_{\alpha j} - K_{\alpha j}] + \sum_{\beta \neq \alpha}^{N_q} \sum_j^{N_{\beta}} q_{\alpha} q_{\beta} J_{\beta j} \right]. \quad (4-4)$$

The APMO/HF energy corrected by MBPT(2) is

$$E_{\text{APMO/MBPT(2)}} = E_{\text{APMO/HF}} + \sum_{\alpha}^{N_q} E_{\alpha\alpha}^{(2)} + \sum_{\alpha}^{N_q} \sum_{\beta>\alpha}^{N_q} E_{\alpha\beta}^{(2)}. \quad (4-5)$$

The second-order correction to the energy for particles of the same species is

$$E_{\alpha\alpha}^{(2)} = \frac{q_{\alpha}^2}{4} \sum_{a_{\alpha}}^{N_{\alpha}} \sum_{b_{\alpha}}^{N_{\alpha}} \sum_{r_{\alpha}>N_{\alpha}}^{B_{\alpha}} \sum_{s_{\alpha}>N_{\alpha}}^{B_{\alpha}} \frac{|\langle a_{\alpha} b_{\alpha} || r_{\alpha} s_{\alpha} \rangle|^2}{\varepsilon_{\alpha a} + \varepsilon_{\alpha b} - \varepsilon_{\alpha r} - \varepsilon_{\alpha s}}, \quad (4-6)$$

the second-order energy correction to interaction between particles of different species is

$$E_{\alpha\beta}^{(2)} = q_{\alpha} q_{\beta} \sum_{a_{\alpha}}^{N_{\alpha}} \sum_{a_{\beta}}^{N_{\beta}} \sum_{r_{\alpha}>N_{\alpha}}^{B_{\alpha}} \sum_{r_{\beta}>N_{\beta}}^{B_{\beta}} \frac{|\langle a_{\alpha} a_{\beta} | r_{\alpha} r_{\beta} \rangle|^2}{\varepsilon_{\alpha a} + \varepsilon_{\beta a} - \varepsilon_{\alpha r} - \varepsilon_{\beta r}}. \quad (4-7)$$

By comparison of the MBPT(2) energy Eq. 4-5 and the exchange correlation energy functional presented in Eq. 2-32, we observe that at the MBPT(2) level  $E_{\alpha}^{xc}[\rho_{\alpha}] = E_{\alpha\alpha}^{(2)}$  and  $E_{\alpha\beta}^c[\rho_{\alpha}, \rho_{\beta}] = E_{\alpha\beta}^{(2)}$ .

### 4.1.3 APMO/HF/HPA theory

This approach makes a distinction between light particles (electrons) and heavy particles (nuclei, muons). For simplicity we present the expressions for a system with just two different types of particles, electrons and a heavy particle. The extension to an arbitrary number of types particles is straightforward. The electronic wave function,  $\Phi_e$ , is represented as a Slater determinant of spin orbitals whereas the heavy particle wave function is constructed as a Hartree product of localized orbitals,  $\psi_m$ :

$$\Psi_0 = \Phi_e \prod_m^{N_m} \psi_m, \quad (4-8)$$

here  $N_n$  is the number of heavy particles. Each heavy particle is treated as a distinguishable particle. The resulting HF equations are written in terms of effective one-particle operators,

$$f_e(i)\psi_{ei} = \varepsilon_{ei}\psi_{ei}, \quad i = 1, \dots, N_e, \quad (4-9)$$

$$f_m(1)\psi_{m1} = \varepsilon_{m1}\psi_{m1}, \quad n = 1, \dots, N_m, \quad (4-10)$$

where  $N_e$  is the number of electrons. Because of the distinguishability of the heavy particles, there is no particle index ( $i$ ) associated to them.

Fock operators,  $f_e$  and  $f_m$ , are written as

$$f_e(i) = h_e(i) + \sum_j^{N_e} [J_{ej} - K_{ej}] - \sum_m^{N_m} q_m J_m, \quad (4-11)$$

$$f_m(1) = h_m(1) + \sum_{m' \neq m}^{N_m} q_m q_{m'} J_{m'} - \sum_j^{N_e} q_m J_{ej}. \quad (4-12)$$

Note that there are no exchange operators,  $K$ , for identical heavy particles in Eq. 4-12. Thus, the sum over Coulomb operators  $J$  cannot include self-repulsion terms. Here, the prime on the  $m'$  index indicates that the  $f_m(1)$  operator adds interactions with all the nuclei different from  $m$ .

The resulting eigenvalues for occupied orbitals are

$$\varepsilon_{ea} = \langle a_e | h | a_e \rangle + \sum_{b_e \neq a_e}^{N_e} \langle a_e b_e | | a_e b_e \rangle + \sum_m^{N_m} q_m \langle a_e 1_m | a_e 1_m \rangle, \quad (4-13)$$

$$\varepsilon_{m1} = \langle 1_m | h | 1_m \rangle + \sum_{m' \neq m}^{N_m} q_m q_{m'} \langle 1_m 1_{m'} | 1_m 1_{m'} \rangle + \sum_{a_e}^{N_e} q_m \langle 1_m a_e | 1_m a_e \rangle, \quad (4-14)$$

and the eigenvalues for virtual orbitals are

$$\varepsilon_{er} = \langle r_e | h | r_e \rangle + \sum_{a_e}^{N_e} \langle r_e a_e | | r_e a_e \rangle + \sum_m^{N_m} q_m \langle r_e 1_m | r_e 1_m \rangle, \quad (4-15)$$

$$\varepsilon_{mr} = \langle r_m | h | r_m \rangle + \sum_{m' \neq m}^{N_m} q_m q_{m'} \langle r_m 1_{m'} | r_m 1_{m'} \rangle + \sum_{a_e}^{N_e} q_m \langle r_m a_e | r_m a_e \rangle. \quad (4-16)$$

The molecular orbitals of electronic and heavy particles are constructed as linear combinations of GTFs. It is worth mentioning that under the HPA, a basis set will be assigned to each heavy particle as they are treated as a distinguishable species. This will have an impact on the computational performance of the HPA calculation. The removal of the non-local exchange terms allows for the decoupling of the heavy particle equations. This results in a simplification of the SCF process. Furthermore, the use of a Hartree product leads to the diagonalization of small (single particle) matrices for the heavy particle part. Electronic and heavy particle MOs are obtained solving Eq. 4-9 and Eq. 4-10 iteratively.

#### 4.1.4 APMO/MBPT(2)/HPA theory

In this approach, the reference hamiltonian for the Rayleigh-Schrödinger perturbation theory is

$$H_0 = \sum_i^{N_e} \left[ h_e(i) + \sum_j^{N_e} [J_{ej} - K_{ej}] - \sum_n^{N_m} q_n J_m \right] + \sum_m^{N_m} \left[ h_m - \sum_j^{N_e} q_m J_{ej} + \sum_{m' \neq m}^{N_m} q_m q_{m'} J_{m'} \right]. \quad (4-17)$$

The fluctuation operator takes the following form:

$$W = \sum_i^{N_e} \sum_{j>i}^{N_e} \frac{1}{r_{ij}} + \sum_m^{N_m} \sum_{m'>m}^{N_m} \frac{q_m q_{m'}}{r_{mm'}} - \sum_i^{N_e} \sum_j^{N_m} \frac{q_j}{r_{ij}} \\ - \sum_i^{N_e} \sum_j^{N_e} [J_{ej} - K_{ej}] - \sum_m^{N_m} \sum_{m' \neq m}^{N_m} q_m q_{m'} J_{m'} + \sum_i^{N_e} \sum_m^{N_m} q_m J_m + \sum_m^{N_m} \sum_j^{N_e} q_m J_{ej}. \quad (4-18)$$

The APMO/HF/HPA energy corrected by MBPT(2) is as follows:

$$E_{\text{APMO/MBPT(2)/HPA}} = E_{\text{APMO/HF/HPA}} + E_{ee}^{(2)} + E_{mm'}^{(2)} + E_{em}^{(2)}, \quad (4-19)$$

where the electronic second-order energy correction term is

$$E_{ee}^{(2)} = \frac{1}{4} \sum_{a_e}^{N_e} \sum_{b_e}^{N_e} \sum_{r_e > N_e}^{B_e} \sum_{s_e > N_e}^{B_e} \frac{|\langle a_e b_e || r_e s_e \rangle|^2}{\varepsilon_{ea} + \varepsilon_{be} - \varepsilon_{er} - \varepsilon_{es}}, \quad (4-20)$$

the heavy particle second-order energy correction term is

$$E_{mm'}^{(2)} = \sum_m^{N_m} \sum_{m'>m}^{N_m} \sum_{r_m > 1}^{B_m} \sum_{r_{m'} > 1}^{B_{m'}} q_m q_{m'} \frac{|\langle 1_m 1_{m'} | r_m r_{m'} \rangle|^2}{\varepsilon_{m1} + \varepsilon_{m'1} - \varepsilon_{mr} - \varepsilon_{m'r}}, \quad (4-21)$$

and the heavy particle-electron second-order energy correction term is

$$E_{em}^{(2)} = \sum_m^{N_m} \sum_{a_e}^{N_e} \sum_{r_m > 1}^{B_m} \sum_{r_e > N_e}^{B_e} q_m \frac{|\langle a_e 1_m | r_e r_m \rangle|^2}{\varepsilon_{ea} + \varepsilon_{m1} - \varepsilon_{er} - \varepsilon_{mr}}. \quad (4-22)$$

## 4.2 Computational details

Equations for the APMO/HF and APMO/MBPT(2) methods have been implemented in the LOWDIN code [80]. A detailed analysis of APMO/HF/HPA equations exposed that these expressions are special cases of the more general APMO/HF/HPA expressions excluding the self-repulsion and the self-exchange. A similar analysis for the APMO/MBPT(2)/HPA equations revealed that these are a subset of the APMO/MBPT(2) expressions when the heavier species are treated as distinguishable particles.

APMO/HF/HPA and APMO/MBPT(2)/HPA calculations can be performed in LOWDIN as a result of its object-oriented nature. The user will only require to create an input in which each heavy particle is treated as a distinguishable particle. For a system containing four quantum protons this step requires labelling each nucleus with a different name,  $H_a$ ,  $H_b$ ,  $H_c$  and  $H_d$ . This technique can be applied in LOWDIN for any number and types of quantum particles.

Regular electronic structure HF and MBPT(2) (we will refer to them as MO/HF and MO/MBPT(2) throughout) and all APMO calculations were performed with the LOWDIN code. In APMO calculations, hydrogen nuclei and negative muons were considered in high-spin configurations [84]. Other nuclei were treated as point charges. Convergence of SCF cycles was achieved when changes in the total energy were lower than  $10^{-9}$  a.u. All calculations were performed on an Intel Pentium-Dual Core (2.93 GHz) with 4 GB of RAM.

In the next three sections we calculate APMO/MBPT(2) and APMO/MBPT(2)/HPA total energies for some hydrogen bonded systems and analyze the origin their differences. Also, we compare the calculated APMO/MBPT(2)/HPA energies for the  $H_2$  molecule with previous full-CI results [51]. In addition, we present some single point calculations on systems containing multiple hydrogen nuclei to determine the computational efficiency of the APMO/MBPT(2)/HPA approach. Finally, we present calculations of the muon-electron correlation energy in muonic molecules.

### 4.3 APMO/MBPT(2)/HPA energies

Total APMO/MBPT(2) and APMO/MBPT(2)/HPA energies of neutral and protonated water and ammonia hydrogen bonded dimers (shown in Figure 4-1) were calculated at the MO/MBPT(2) optimized geometry. 6-31G(d,p) electronic basis set [104] and DZSPD [45, 84] nuclear basis set were employed. Results presented in Table 4-1 reveal that APMO/MBPT(2)/HPA total energies are at least  $10^{-2}$  a.u. lower than those calculated at the APMO/MBPT(2) level. To unveil the origin of these differences, we have also included in Table 4-1 zeroth-order and second-order correlation energy contributions. A detailed comparison of the energy results reveals that zeroth-order ( $E_{APMO}$ ), second-order electronic correlation ( $E_{ee}^{(2)}$ ) and nuclear-nuclear correlation ( $E_{nn}^{(2)}$ ) APMO/MBPT(2) and APMO/MBPT(2)/HPA energies differ by less than  $10^{-4}$  a.u.. In contrast, differences in nuclear-electron correlation energies ( $E_{ee}^{(2)}$ ) are of the order of  $10^{-2}$  a.u. and account for at least 99.8 % of the total energy differences observed between both methods.

The origin of the observed differences in nuclear-electron correlation energy can be deduced by inspecting the APMO/MBPT(2) (Eq. 4-7) and APMO/MBPT(2)/HPA (Eq. 4-22) expressions. To this aim, we present the expressions for a hydrogen molecule using the [STO-3G:DZS] electronic:nuclear basis sets [45, 107]. This system contains two electrons occupying one electronic orbital  $1_e$ . With this minimal electronic basis set there is only one virtual electronic orbital  $2_e$ . At the APMO/MBPT(2) level of theory, the two protons

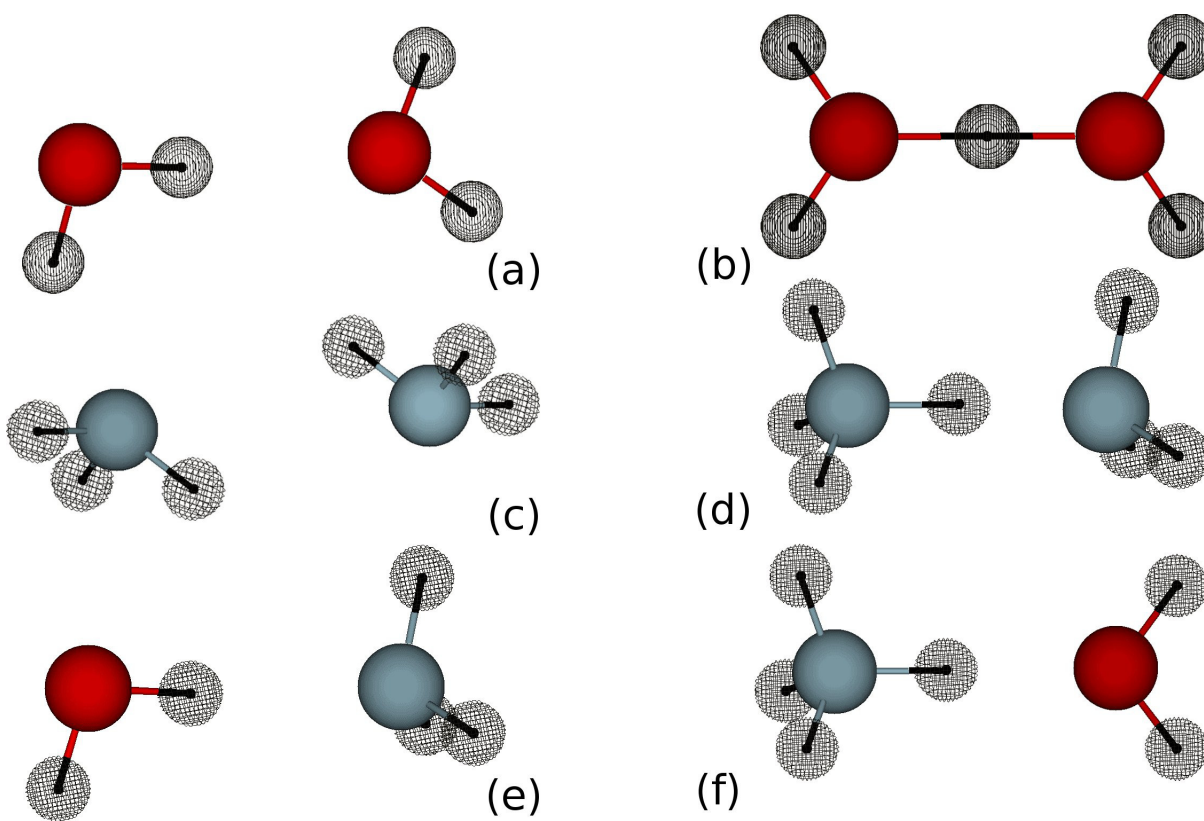


**Figure 4-1:** Schematic representation of hydrogen bonded dimers and complexes. (a)  $[\text{HOH}\cdots\text{OH}_2]$  (b)  $[\text{H}_2\text{O}\cdots\text{H}\cdots\text{OH}_2]^+$  (c)  $[\text{H}_2\text{NH}\cdots\text{NH}_3]$  (d)  $[\text{H}_3\text{N}\cdots\text{H}\cdots\text{NH}_3]^+$  (e)  $[\text{HOH}\cdots\text{NH}_3]$  (f)  $[\text{H}_3\text{NH}\cdots\text{OH}_2]^+$ . Black grids represented hydrogen nuclei treated as a quantum waves. Red and blue balls represent oxygen and nitrogen nuclei.

occupy two nuclear orbitals  $1_H$  and  $2_H$ . With this nuclear basis there are two virtual nuclear orbitals  $3_H$  and  $4_H$ . At this level of theory the proton-electron correlation energy term is

$$E_{en}^{(2)} = 2 \frac{|\langle 1_e 1_H | 2_e 3_H \rangle|^2}{\varepsilon_{e1} + \varepsilon_{H1} - \varepsilon_{e2} - \varepsilon_{H3}} + 2 \frac{|\langle 1_e 1_H | 2_e 4_H \rangle|^2}{\varepsilon_{e1} + \varepsilon_{H1} - \varepsilon_{e2} - \varepsilon_{H3}} + 2 \frac{|\langle 1_e 2_H | 2_e 3_H \rangle|^2}{\varepsilon_{e1} + \varepsilon_{H2} - \varepsilon_{e2} - \varepsilon_{H3}} + 2 \frac{|\langle 1_e 2_H | 2_e 4_H \rangle|^2}{\varepsilon_{e1} + \varepsilon_{H2} - \varepsilon_{e2} - \varepsilon_{H4}}. \quad (4-23)$$

Using the APMO/MBPT(2)/HPA method the two protons ( $H_a$  and  $H_b$ ) are made distinguishable.  $H_a$  proton occupies orbital  $1_{H_a}$  and has one virtual orbital  $2_{H_a}$ . Similarly,  $H_b$  proton occupies orbital  $1_{H_b}$  and has one virtual orbital  $2_{H_b}$ . At this level of theory the proton-electron correlation energy term is

$$E_{en}^{(2)} = 2 \frac{|\langle 1_e 1_{H_a} | 2_e 2_{H_a} \rangle|^2}{\varepsilon_{e1} + \varepsilon_{H_{a1}} - \varepsilon_{e2} - \varepsilon_{H_{a2}}} + 2 \frac{|\langle 1_e 1_{H_b} | 2_e 2_{H_b} \rangle|^2}{\varepsilon_{e1} + \varepsilon_{H_{b1}} - \varepsilon_{e2} - \varepsilon_{H_{b2}}}. \quad (4-24)$$

We observe that Eq. 4-23 contains two more terms than Eq. 4-24 because there are more possible excitations at the APMO/MBPT(2) level. The final nuclear-electron correlation energies depend on the squares of the Coulomb integrals in the numerators and the eigenvalues of occupied and virtual electron and nuclear orbitals in the denominators. Table 4-2 reports the calculated total APMO/MBPT(2) and APMO/MBPT(2)/HPA nuclear-electron correlation energies along with the Coulomb integrals and the eigenvalues for occupied and virtual orbitals.

At the APMO/MBPT(2) level, the eigenvalues of occupied orbitals are negative and those of virtual orbitals are positive. At the APMO/MBPT(2)/HPA level, the eigenvalues of the occupied and virtual orbitals are always negative. Using the eigenvalues presented in Table 4-2, the four denominators in Eq. 4-23 (APMO/MBPT(2) method) are equal to -5.0428 a.u. and the two denominators of Eq. 4-24 (APMO/MBPT(2)/HPA method) are equal to -1.3340 a.u..

We now evaluate the numerators appearing in Eq. 4-23 and Eq. 4-24. Because the four denominators in APMO/MBPT(2) expression (Eq. 4-23) are numerically equal, we can factorize them and calculate the numerator as the sum of the squares of the Coulomb integrals obtaining a value of  $2.750 \times 10^{-3}$  a.u.<sup>2</sup>. Similarly for the APMO/MBPT(2)/HPA expression (Eq. 4-24), after factorizing the two energy terms and adding the squares of the Coulomb integrals we obtain a value of  $2.744 \times 10^{-3}$  a.u.<sup>2</sup>. Since the numerators appearing in the energy expressions of the APMO/MBPT(2) and APMO/MBPT(2)/HPA methods are practically equal, any difference between the nuclear-electron correlation energies must be caused by variations in the denominator values. As observed above, the denominator of the APMO/MBPT(2)/HPA method is almost four times smaller than that of APMO/MBPT(2) method, therefore the nuclear-electron correlation energy in the APMO/MBPT(2)/HPA method is almost four times larger.

**Table 4-1:** APMO/MBPT(2) and APMO/MBPT(2)/HPA total energies ( $E_{\text{MBPT}(2)}$ ), zeroth-order energies ( $E_{\text{APMO}}$ ) and electron ( $E_{ee}^{(2)}$ ), electronic-nuclear ( $E_{en}^{(2)}$ ), nuclear ( $E_{nn}^{(2)}$ ) correlation energies, in a.u., for hydrogen bonded dimers.

System	Reference	$E_{\text{MBPT}(2)}$	$E_{\text{APMO}}$	$E_{ee}^{(2)}$	$E_{en}^{(2)}$	$E_{nn}^{(2)}$
[HOH ... OH <sub>2</sub> ]	APMO/HF	-152.2973	-151.8878	-0.4011	-0.0085	-1 × 10 <sup>-6</sup>
	APMO/HF/HPA	-152.3082	-151.8878	-0.4011	-0.0194	-1 × 10 <sup>-5</sup>
[H <sub>2</sub> O ... H ... OH <sub>2</sub> ] <sup>+</sup>	APMO/HF	-152.6109	-152.1949	-0.4058	-0.0102	-1 × 10 <sup>-6</sup>
	APMO/HF/HPA	-152.6232	-152.1949	-0.4058	-0.0225	-2 × 10 <sup>-5</sup>
[H <sub>2</sub> NH ... NH <sub>3</sub> ]	APMO/HF	-112.5402	-112.1391	-0.3880	-0.0130	-1 × 10 <sup>-6</sup>
	APMO/HF/HPA	-112.5582	-112.1391	-0.3880	-0.0311	-2 × 10 <sup>-5</sup>
[H <sub>3</sub> N ... H ... NH <sub>3</sub> ] <sup>+</sup>	APMO/HF	-112.9057	-112.4955	-0.3954	-0.0148	-2 × 10 <sup>-6</sup>
	APMO/HF/HPA	-112.9255	-112.4955	-0.3954	-0.0346	-3 × 10 <sup>-5</sup>
[HOH ... NH <sub>3</sub> ]	APMO/HF	-132.4238	-132.0179	-0.3952	-0.0107	-1 × 10 <sup>-6</sup>
	APMO/HF/HPA	-132.4382	-132.0179	-0.3952	-0.0251	-2 × 10 <sup>-5</sup>
[H <sub>3</sub> NH ... OH <sub>2</sub> ] <sup>+</sup>	APMO/HF	-132.7700	-132.3593	-0.3982	-0.0125	-1 × 10 <sup>-6</sup>
	APMO/HF/HPA	-132.7863	-132.3593	-0.3982	-0.0288	-3 × 10 <sup>-5</sup>

Calculations were performed at the MO/MBPT(2) 6-31G(d,p) optimized geometries using the [6-31G(d,p):DZSPD]

electronic:nuclear basis sets.

The results presented so far clearly reveal that variations in the nuclear-electron correlation energies are due to differences in the eigenvalues of occupied and virtual orbitals. In general, APMO/HF and APMO/HF/HPA expressions for the eigenvalues of occupied (Eq. 4-1 and Eq. 4-13) and virtual electronic orbitals (Eq. 4-2 and Eq. 4-15) are equal. Similarly, APMO/HF and APMO/HF/HPA expressions for the eigenvalues of occupied nuclear orbitals (Eq. 4-1 and Eq. 4-14) are considered to be equal, because the only differences between them come from the exchange terms, which are negligible [84].

In contrast, APMO/HF and APMO/HF/HPA expressions for the eigenvalues of virtual nuclear orbitals (Eq. 4-2 and Eq. 4-16) are different: at the APMO/HF level, Eq. 4-2 includes the sum of Coulomb integrals between a virtual nuclear orbital and all the occupied nuclear orbitals, whereas in APMO/HF/HPA method, Eq. 4-16 includes the sum of Coulomb integrals between a virtual nuclear orbital and all the occupied nuclear orbitals excluding the occupied nuclear orbital of the same nuclear species (recall that in APMO/HF/HPA all nuclei are treated as different species). The absence of this repulsive term makes the APMO/HF/HPA nuclear virtual eigenvalues lower in energy than those in the APMO/HF method. Thus, the difference between occupied and virtual orbital energies will be lower in the APMO/HF/HPA method, and as a result, the denominators of each nuclear-electron correlation contribution will be smaller in the APMO/MBPT(2)/HPA method. If the sum of the squares of the Coulomb integrals is similar in both methods, as shown above, then the APMO/MBPT(2)/HPA nuclear-electron correlation energy will always be lower (more negative) than the APMO/MBPT(2) one.

Different physical meanings can be associated to the nuclear virtual eigenvalues of APMO/HF and APMO/HF/HPA methods. At the APMO/HF level, a nuclear virtual eigenvalue can be related to the nuclear affinity of the molecule, in the same way that an electronic virtual eigenvalue is related to the electronic affinity [68, 69, 86]. At the APMO/HF/HPA level, a nuclear virtual eigenvalue can be associated to its nuclear ionization potential.

Swalina, Pak and Hammes-Schiffer [47] previously addressed a similar eigenvalue difference for the case of a single active proton when they proposed an alternative formulation of the MBPT(2) proton-electron correlation. The energy differences in APMO/MBPT(2) and APMO/MBPT(2)/HPA nuclear-nuclear correlation terms can be explained in a similar fashion.

In Table **4-3** we present a comparison of the APMO/MBPT(2) and APMO/MBPT(2)/HPA total and nuclear-electron correlation energies of the H<sub>2</sub> molecule isotopologues with the MC-MO full-CI results of Ishimoto et al [51]. These calculations were performed with a 5s2p1d electronic basis set formed with the primitives of the Dunning's cc-pVTZ electronic basis set [88] and Nakai's 5s5p5d nuclear basis set [43].

Table **4-3** clearly reveals that APMO/MBPT(2)/HPA total and nuclear-electron correlation energies are closer to the full-CI results than APMO/MBPT(2) ones. Because the full-CI method is variational, from this comparison we can conclude that APMO/MBPT(2)/HPA gives a better description of the nuclear-electron correlation in the H<sub>2</sub> molecule than APMO/

**Table 4-2:** APMO/MBPT(2) and APMO/MBPT(2)/HPA H<sub>2</sub> electronic and nuclear eigenvalues, integrals and nuclear-electron correlation energies ( $E_{en}^{(2)}$ ). Energies in a.u.

APMO/MBPT(2)		APMO/MBPT(2)/HPA	
$\varepsilon_{e1}$	-0.5603	$\varepsilon_{e1}$	-0.5603
$\varepsilon_{e2}$	0.7202	$\varepsilon_{e2}$	0.7202
$\varepsilon_{H1}$	-1.0951	$\varepsilon_{H_a1}$	-1.0951
$\varepsilon_{H2}$	-1.0951	$\varepsilon_{H_b1}$	-1.0951
$\varepsilon_{H3}$	2.6672	$\varepsilon_{H_a2}$	-1.0416
$\varepsilon_{H4}$	2.6672	$\varepsilon_{H_b2}$	-1.0416
$\langle 1_e 1_H   2_e 3_H \rangle$	$8.823 \times 10^{-3}$	$\langle 1_e 1_{H_a}   2_e 2_{H_a} \rangle$	$8.824 \times 10^{-3}$
$\langle 1_e 1_H   2_e 4_H \rangle$	$3.574 \times 10^{-4}$	$\langle 1_e 1_{H_b}   2_e 2_{H_b} \rangle$	$8.824 \times 10^{-3}$
$\langle 1_e 2_H   2_e 3_H \rangle$	$3.574 \times 10^{-4}$		
$\langle 1_e 2_H   2_e 4_H \rangle$	$8.823 \times 10^{-3}$		
$E_{en}^{(2)}$	$-5.453 \times 10^{-5}$	$E_{en}^{(2)}$	$-2.057 \times 10^{-4}$

Calculations were performed using the [STO-3G:DZS] electronic:nuclear basis sets at the MO/HF STO-3G optimized geometry.

MBPT(2). We expect that in larger molecular systems the same trend would be observed. Nevertheless, we must note that the APMO/MBPT(2)/HPA only recovers about 45% of the full-CI nuclear-electron correlation energy, so for certain applications MBPT(2) may not provide enough interparticle correlation.

## 4.4 APMO/MBPT(2)/HPA computational efficiency

We performed APMO/MBPT(2) and APMO/MBPT(2)/HPA single-point calculations on linear chains of hydrogen fluoride molecules, (HF)<sub>n</sub> for n=1 to n=20. A schematic representation of these molecules is provided in Figure 3-1. Calculations were performed with the [6-31:DZSP] electronic:nuclear basis set [45, 104], because these basis sets have similar number of contractions per HF molecule.

Our calculations reveal that total calculation times are always lower with the APMO/MBPT(2)/HPA methodology.

To understand why APMO/MBPT(2)/HPA calculations are faster than APMO/MBPT(2) we analyze the impact of the HPA on the four center integral transformation times, because these steps are the most computationally expensive ones in a MBPT(2) calculation. Electron-electron integrals transformation times are identical for both methods, so we focus on nuclear-electron and nuclear-nuclear transformation times. Those results are presented in Figure 4-2. This figure clearly reveals that the HPA reduces significantly the transformation times required in each calculation. Furthermore, it is evident that the HPA reduces the scaling of

**Table 4-3:** APMO/MBPT(2), APMO/MBPT(2)/HPA and MC\_MO full-CI<sup>b</sup> total (E) and nuclear-electron correlation energies ( $E_{en}$ ) for the H<sub>2</sub>, HD and D<sub>2</sub> molecules. Energies in a.u.<sup>a</sup>

System	Method	E	$E_{en}$
H <sub>2</sub>	APMO/MBPT(2)	-1.0952	-0.0119
	APMO/MBPT(2)/HPA	-1.1102	-0.0254
	MC_MO/full-CI <sup>b</sup>	-1.1393	-0.0539
HD	APMO/MBPT(2)	-1.1043	-0.0098
	APMO/MBPT(2)/HPA	-1.1173	-0.0217
	MC_MO/full-CI <sup>b</sup>	-1.1436	-0.0464
D <sub>2</sub>	APMO/MBPT(2)	-1.1134	-0.0078
	APMO/MBPT(2)/HPA	-1.1246	-0.0180
	MC_MO/full-CI <sup>b</sup>	-1.1482	-0.0412

<sup>a</sup> MBPT(2) Calculations were performed using the [5s2p1d:5s5p5d] electronic:nuclear basis sets at the APMO/MBPT(2)/HPA optimized geometry.

<sup>b</sup>Ref. [51] full-CI MC\_MO calculation with a [5s2p1d:1s1p1d] electronic:optimal nuclear basis set

both transformation times with respect to the number of HF molecules.

To explain the lowering of the scaling observed, we analyze the number of integrals required to evaluate the correlation energies (eqs. 4-7,4-21,4-22) for both methods. The number of integrals required to obtain the APMO/MBPT(2) nuclear-electron correlation energy is proportional to  $N_e N_H (B_e - N_e) (B_H - N_H)$ , where  $N_e$  is the number of occupied electronic orbitals,  $N_H$  is the number of occupied nuclear orbitals,  $B_e$  is the electronic basis set size and  $B_H$  is the nuclear basis set size respectively. The number of integrals required to obtain the APMO/MBPT(2) nuclear-nuclear correlation energy is proportional to  $N_H^2 (B_H - N_H)^2$ . For this method, all  $N_e$ ,  $N_H$ ,  $B_e$  and  $B_H$  increase linearly as the size of the HF chain increases. Therefore the number of integrals required by APMO/MBPT(2) increases quartically with the size of the system. As a consequence of the stepwise algorithm used for the atomic to molecular integral transformation [108] the nuclear-nuclear and nuclear-electron integral transformations have a formal quintic scaling with the size of the system.

The number of integrals required to obtain the APMO/MBPT(2)/HPA nuclear-electron correlation energy is proportional to  $N_n N_e (B_H - 1) (B_e - N_e)$ , where  $N_n$  is the number of protons of the system. The number of integrals required to obtain the APMO/MBPT(2)/HPA nuclear-nuclear correlation energy is proportional to  $N_n^2 (B_H - 1)^2$  are required. The use HPA and localized basis sets has two consequences: The number of nuclear occupied orbitals is always one; and the basis set size for each nucleus,  $B_H$ , is independent from the system size. Therefore, only  $N_n$ ,  $N_e$  and  $B_e$  increase as the size of the HF chain grows. Consequently, the number of integrals required by the APMO/MBPT(2)/HPA nuclear-

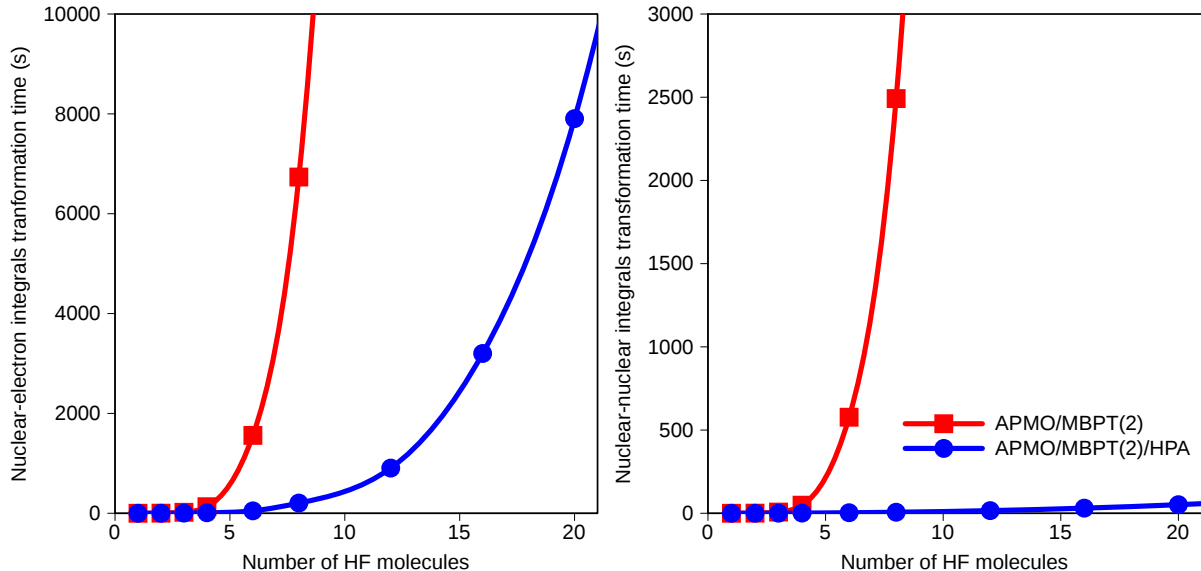


**Figure 4-2:** Nuclear-electron (right) and nuclear-nuclear (left) integral transformation times for HF chains of different length. Continuous lines represent cubic splines interpolations drawn to guide the eye.

electron and nuclear-nuclear correlation energies increase cubically and quadratically respectively. Using the stepwise integral transformation algorithm [108], the formal scalings of the APMO/MBPT(2)/HPA nuclear-electron and nuclear-nuclear integral transformations are quartic and cubic respectively.

## 4.5 Negative muon-electron correlation

In previous works we have studied the electronic properties of atoms and molecules containing negative muons at the APMO/HF level of theory [38, 39]. Our results have revealed that an atom with one negative muon ( $\mu$ ) chemically behaves as an all-electron atom with atomic number  $Z-1$ , because the muonic density is localized over the nucleus and screens one positive charge from it. However, in these studies we did not include muon-electron correlation. To gain insight on the importance of the muon-electron correlation in the APMO framework, we have performed APMO/MBPT(2) and APMO/MBPT(2)/HPA calculations on muonic helium,  $\text{He}\mu$ , muonic lithium,  $\text{Li}\mu$  and muonic helium dimer,  $(\text{He}\mu)_2$ . To perform these calculations we have constructed large even-tempered basis sets [38] for negative muons and for electrons. For simplicity, we consider infinite nuclear masses in these calculations.

As it can be seen in Table 4-4, the muon-electron correlation energies are very sensitive to the choice of basis sets. For instance, the inclusion of 5p functions on the 10s basis sets increases the muon-electron correlation energy by three orders of magnitude. When the basis sets were increased from 10s5p to 20s10p an increase of one order of magnitude is

observed. Nevertheless, further increases in the number of s and p functions or the inclusion of d functions do not recover any more muon-electron correlation. The largest value for the negative muon-electron correlation obtained was  $-1.70 \times 10^{-6}$  a.u. for the muonic helium dimer with the 31s13p basis sets. For most chemical applications energies of this magnitude are negligible.

Further analysis of the muon-electron correlation energy shows that the APMO/MBPT(2)/HPA method recovers more correlation than the APMO/MBPT(2) one. The origin of this energy difference is the same discussed above in the case of nuclear-electron correlation: the APMO/HF/HPA muonic virtual eigenvalues do not include a muon-muon repulsive terms that the APMO/HF ones have.

To verify the validity of these results, we have performed a two particle full-CI calculation on the muonic helium atom with the 20s10p basis sets. From this calculation we obtained a value of  $-0.596 \times 10^{-6}$  a.u. for the muon-electron correlation, which is in excellent agreement with the APMO/MBPT(2)/HPA value of  $-0.590 \times 10^{-6}$  a.u.

These results present a contrary situation of the nuclear-electron correlation discussed previously: For systems containing negative muons and electrons the APMO/HF reference provides a good description of the electron-muon interaction as the muon-electron correlation is negligible. This result opens up the possibility of combining APMO/HF calculations for the negative muon-electron interaction with highly correlated electronic structure methods to obtain very accurate chemical properties of muonic atoms and molecules [109].

**Table 4-4:** APMO/MBPT(2) and APMO/MBPT(2)/HPA total ( $E_{\text{MBPT}(2)}$ ), electron correlation ( $E_{ee}^{(2)}$ ) and negative muon-electron correlation ( $E_{e\mu}^{(2)}$ ) energies for muonic helium, muonic lithium and muonic helium dimer. Energies in a.u.<sup>a</sup>

System	[e <sup>-</sup> : $\mu^-$ ] basis sets	APMO/MBPT(2)			APMO/MBPT(2)/HPA		
		$E_{\text{MBPT}(2)}$	$E_{ee}^{(2)}$	$E_{e\mu}^{(2)}/10^{-6}$	$E_{\text{MBPT}(2)}$	$E_{ee}^{(2)}$	$E_{e\mu}^{(2)}/10^{-6}$
$^{\infty}\text{He}\mu$	[ 10s : 10s ]	-413.9248	-0.0002	-0.0002	-413.9248	-0.0002	-0.0002
	[ 10s5p : 10s5p ]	-413.9248	-0.0337	-0.0337	-413.9248	-0.0464	-0.0464
	[ 20s10p : 20s10p ]	-414.0107	-0.4557	-0.4557	-414.0107	-0.5905	-0.5905
	[ 20s10p5d : 20s10p5d ]	-414.0357	-0.4557	-0.4557	-414.0357	-0.5904	-0.5904
	[ 31s13p : 31s13p ]	-414.0366	-0.4629	-0.4629	-414.0366	-0.5976	-0.5976
$^{\infty}\text{Li}\mu$	[ 10s : 10s ]	-932.5036	-0.0134	-0.0002	-932.5036	-0.0134	-0.0002
	[ 10s5p : 10s5p ]	-932.5200	-0.0298	-0.0342	-932.5200	-0.0298	-0.0427
	[ 20s10p : 20s10p ]	-933.1740	-0.0324	-0.9494	-933.1740	-0.0324	-1.1563
	[ 20s10p5d : 20s10p5d ]	-933.3479	-0.0348	-0.9489	-933.3479	-0.0348	-1.1556
	[ 31s13p : 31s13p ]	-933.3513	-0.0324	-0.9799	-933.3513	-0.0324	-1.1867
$(^{\infty}\text{He}\mu)_2$	[ 10s : 10s ]	-827.9966	-0.0185	-0.0005	-827.9966	-0.0185	-0.0006
	[ 10s5p : 10s5p ]	-828.0135	-0.0304	-0.1040	-828.0135	-0.0304	-0.1428
	[ 20s10p : 20s10p ]	-828.1856	-0.0307	-1.2978	-828.1856	-0.0307	-1.6788
	[ 20s10p5d : 20s10p5d ]	-828.2375	-0.0324	-1.2990	-828.2375	-0.0324	-1.6804
	[ 31s13p : 31s13p ]	-828.2374	-0.0307	-1.3179	-828.2374	-0.0307	-1.6988

$(^{\infty}\text{He}\mu)_2$  was calculated at an internuclear separation of 0.7414 Å. For this system Negative muon-negative muon correlation is lower than  $10^{-13}$  a.u.

**Table 4-5:** Molecules, molecular ions and hydrogen-bonded dimers used as reference for the construction of a nuclear-electron correlation using APMO/MBPT(2)/HPA calculations

ArHAr <sup>+</sup>	AlH <sub>4</sub> <sup>-</sup>	AlH <sub>3</sub>	AlH <sub>2</sub> <sup>+</sup>	NH <sub>4</sub> <sup>+</sup>
ArH <sup>+</sup>	ClHCl <sup>-</sup>	H <sub>2</sub> Cl <sup>+</sup>	LiH	OH <sup>-</sup>
BeH <sub>2</sub>	ClHFH	H <sub>2</sub> OHCl	MgH <sub>2</sub>	PH <sub>2</sub> <sup>-</sup>
BeH <sup>+</sup>	H <sub>3</sub> <sup>+</sup>	NH <sub>3</sub>	MgH <sup>+</sup>	PH <sub>3</sub>
BH <sub>2</sub> <sup>+</sup>	FH <sub>2</sub> <sup>+</sup>	H <sub>2</sub> OHF	NaHHF	PH <sub>4</sub> <sup>+</sup>
BH <sub>3</sub>	FHCl <sup>-</sup>	H <sub>2</sub> O	NaH	SH <sup>-</sup>
BH <sub>4</sub> <sup>-</sup>	FHFH	H <sub>2</sub>	NeHNe <sup>+</sup>	SiH <sub>3</sub> <sup>-</sup>
CH <sub>3</sub> <sup>-</sup>	FHF <sup>-</sup>	H <sub>2</sub> S	NeH <sup>+</sup>	SiH <sub>3</sub> <sup>+</sup>
CH <sub>3</sub> <sup>+</sup>	FHOH <sup>-</sup>	H <sub>3</sub> O <sup>+</sup>	NH <sub>2</sub> <sup>-</sup>	SiH <sub>4</sub>
CH <sub>4</sub>	FH			

## 4.6 An approximated MBPT(2) nuclear-electron correlation functional

Based on the APMO/MBPT(2)/HPA results we have proposed an approximated nuclear-electron correlation functional of the nuclear and electronic densities for the hydrogen nucleus.

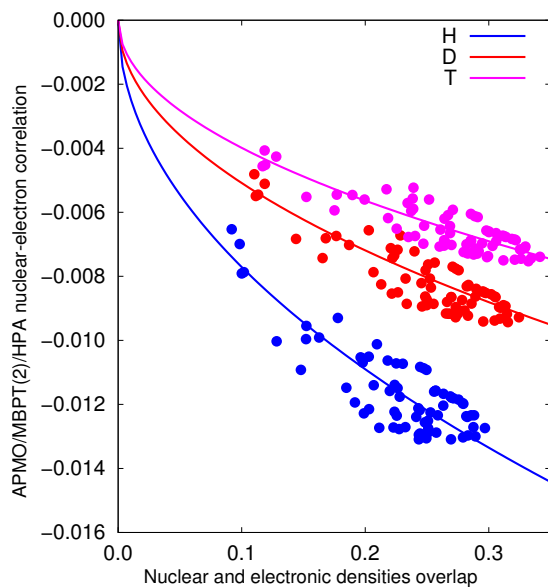
We have considered that at infinite nuclear-electron separation the correlation energy must be zero. To recover the BOA results, the correlation energy of a nucleus with infinite mass should also be zero [82]. We have taken as reference APMO/MBPT(2)/HPA nuclear-electron correlation energies for the H,D,T isotopologues of the 52 molecules, molecular ions and hydrogen-bonded dimers presented in Table 4-5. As electronic basis set the primitives of the cc-pVTZ basis set were used [88–90]. As nuclear basis set Nakai’s 5s5p basis sets were used [43].

Figure 4-3 presents the relation between the densities overlap,  $S_{eH} = \int \rho_e(\mathbf{r})\rho_H(\mathbf{r})d\mathbf{r}$ , and the APMO/MBPT(2)/HPA correlation energies. Through trial and error we found that this relation could be fitted to the equation,

$$E_{eH}^c = -A \frac{S_{eH}^B}{m^C}, \quad (4-25)$$

where A, B and C are fitting parameters. This equation satisfies both the infinite separation and the infinite mass limits discussed before. The computational evaluation of this equation on a numerical grid has a formal cubic scaling. Therefore, it estimates nuclear-electron correlation energies faster than the APMO/MBPT(2)/HPA method.

The parameters obtained using a minimum-squares fit are reported in Table 4-6. With these parameters the average and maximum deviations from the reference data are 1.3 and 4.0



**Figure 4-3:** Relation between the nuclear and electron densities overlap and the APMO/MBPT(2)/HPA nuclear-electron correlation energies for the H/D/T isotopologues. Continuous lines represent the minimum-squares fit to eq. 4-25

kJ/mol respectively, and the average percent deviation is 5.6 %. These results reveal that replacing the APMO/MBPT(2)/HPA nuclear-electron correlation energy with its approximated form introduces an error lower than chemical accuracy (1 kcal/mol or 4.2 kJ/mol). Therefore, for most chemical applications, the quality of the results obtained with the exact and approximated APMO/MBPT(2)/HPA energies should be the same.

We should note that using eq. 4-25 may be used to fit the relation between the densities overlap and the nuclear-electron correlation energies obtained with different (higher) levels of theory and/or larger basis sets.

We have to take into account that MBPT(2) is only the first step towards the inclusion of interspecies correlation in APMO calculations. Even with the HPA, for the  $H_2$  molecule and its isotopologues it only recovers about 45% of the full-CI nuclear-electron correlation. The amount of interparticle correlation in an APMO calculation may be further improved by extending this framework to explicitly correlated wave-function schemes [53, 106], multi-component density functional theory methods [110] or multiconfigurational approaches [51]. Nevertheless, some of these methodologies have very high computational cost. Therefore, APMO/MBPT(2)/HPA stands out as a good starting point in the study of the effects of interspecies correlation in medium-sized systems.

**Table 4-6:** Fitting parameters, average and maximum deviations for the minimum-squares fit of the APMO/MPBT(2)/HPA nuclear-electron correlation data using eq. 4-25

A	2.215
B	0.5
C	0.6
aad <sup>a</sup>	1.3 kJ/mol
mad <sup>b</sup>	4.0 kJ/mol
apd <sup>a</sup>	5.6 %

<sup>a</sup> average absolute deviation

<sup>b</sup> maximum absolute deviation

<sup>a</sup> average percent deviation

# 5 Hydrogen Isotope Effects on Covalent and Noncovalent Interactions: the Case of Protonated Rare Gas Clusters

In this chapter we present an application of the APMO/MBPT(2)/HPA theory to study the magnitude of NQEs on chemical systems.

Protonated rare gas clusters represent prototypical systems for solvation by traditionally chemically inert rare gas atoms. Of particular interest is the nature of the rare gas-hydrogen ion bond in these cationic complexes, because, as opposed to the case of neutral rare gas clusters, it is governed not just by dispersion interactions.

Several theoretical studies on the structural and vibrational properties of  $\text{Rg}_2\text{H}^+$  complexes [111–117] have revealed that these complexes are strongly bound presenting a linear shape with the hydrogen nucleus adopting a centrosymmetric position.

Extensive studies on the structure of larger rare gas clusters  $\text{Rg}_n\text{H}^+$  ( $n > 2$ ) [118–124] have exposed the formation of solvation Rg shells around a  $\text{Rg}_2\text{H}^+$  core. In these cases the binding energies of the rare gas atoms located in these outer shells are substantially smaller than those of the rare gas atoms forming the  $\text{Rg}_2\text{H}^+$  ionic core. These systems therefore become excellent choices for investigating the impact of H/D/T isotope and nuclear quantum effects on different covalent and noncovalent interactions.

There is particular interest in assessing the magnitude of H/D isotope effects (IEs) in non-covalent interactions because there are many examples of significant IEs in these type of interactions (see Ref [125] and references therein). To the best of our knowledge IEs on protonated rare gas clusters have been rarely studied. A few reports on the vibrational states of  $\text{He}_2\text{H}^+$  and  $\text{He}_2\text{D}^+$  [111, 117] and a study on the structure and stability of the  $\text{He}_2\text{H}^+$  isotopologues [63] have exposed that significant H/D IEs are observed on the structural and spectroscopic properties of  $\text{He}_2\text{H}^+$ .

Nuclear quantum effects on the structure and stability of the  $\text{Rg}_n\text{H}^+$  clusters cannot be determined readily by employing conventional electronic structure methods based on the BOA, because in these methods the electronic and nuclear degrees of freedom are completely uncoupled. As opposed to Born-Oppenheimer approximation based schemes, nuclear orbital approaches, offer efficient methodologies to study nuclear quantum effects directly from single calculations and not as further corrections, such as the APMO method. Nuclear orbital methods have been employed successfully to explain observed H/D IEs in a wide

variety of systems [2, 3, 44, 51, 60, 61, 64, 72, 74, 84, 126–129].

In this chapter we present a theoretical study of the H/D/T IEs on protonated helium, neon and argon clusters. We will refer as these complexes as  $\text{Rg}_n\text{X}^+$  ( $\text{Rg}=\text{He,Ne,Ar}$ ,  $\text{X}=\text{H,D,T}$  and  $n=1-3$ ). Calculations have been performed with the APMO/MBPT(2)/HPA method (see chapter 4). To gain insight on the IEs on the rare gas-hydrogen ion interaction we propose an APMO/MBPT(2)/HPA energy decomposition analysis (EDA) scheme based on the proton affinities of the rare gas clusters. These results have been published in the *International Journal of Quantum Chemistry* [65]

This chapter is organized as follows: Methodology section explains the computational details. Energy decomposition analysis section proposes an APMO/MBPT(2)/HPA EDA scheme. Results and discussion section presents the H/D/T IEs on the rare gas binding energies and geometries of  $\text{Rg}_n\text{X}^+$ .

## 5.1 Methodology

APMO/MBPT(2)/HPA geometry optimizations and EDA calculations were performed with the LOWDIN code. In all calculations hydrogen nuclei were treated as quantum waves, whereas helium, neon and argon nuclei were treated as +2, +10, +18 point charges respectively. The aug-cc-pVTZ electronic basis set [88–90] and the 5ZSP-DZD nuclear basis set [130] were employed. Geometry optimizations were performed without imposing symmetry restrictions. Optimization tolerance was set to  $1 \times 10^{-7}$  Hartree/Bohr. Rg-X bond distance was calculated as the expectation value,  $\langle R_{\text{Rg-X}} \rangle$  of the unperturbed nuclear wavefunction. The stability of  $\text{Rg}_n\text{X}^+$  complexes was evaluated in terms of one rare gas atom binding energies ( $E_{\text{Rg}_n \rightarrow n+1\text{X}^+}$ ), defined as the energy of the reaction



$$E_{\text{Rg}_n \rightarrow n+1\text{X}^+} = E_{\text{Rg}_{n+1}\text{X}^+} - E_{\text{Rg}} - E_{\text{Rg}_n\text{X}^+}. \quad (5-2)$$

Counterpoise basis set superposition error corrections were not performed on these binding energies, because previous reports for these systems have revealed that this scheme overcorrects this error [131].

## 5.2 Energy Decomposition Analysis

Here we propose an energy decomposition analysis scheme based on single-point energy calculations for the proton affinity (PA) of the rare gas cluster, considering the cluster and the hydrogen ion as the monomers.

Proton affinities are related to cluster binding energies, because the reaction in Eq. 5-1 is

equivalent to the process of deprotonation, growth and protonation of a rare gas cluster,



Therefore, binding energies can be expressed in terms of these three energies,

$$E_{\text{Rg}_n \rightarrow n+1}\text{X}^+ = E_{\text{Rg}_n \rightarrow n+1} + \text{PA}_{\text{Rg}_n} - \text{PA}_{\text{Rg}_{n+1}}. \quad (5-6)$$

For simplicity, we assume that the rare gas cluster ( $\text{Rg}_n$ ) is already at the protonated complex ( $\text{Rg}_n\text{X}^+$ ) geometry. The proton affinity can be decomposed in terms of the interaction energy between the rare gas cluster and the hydrogen ion,  $E_{\text{Rg}_n\text{X}^+}^{\text{int}}$ , and the zero-point energy contribution. In the present calculations only the hydrogen nuclei are treated as quantum waves, and as a result only their zero-point energies,  $\text{HZPE}_{\text{Rg}_n\text{X}^+}$ , are considered.

$$\text{PA}_{\text{Rg}_n} = E_{\text{Rg}_n\text{X}^+}^{\text{int}} + \text{HZPE}_{\text{Rg}_n\text{X}^+}. \quad (5-7)$$

This interaction energy can be analyzed following Morokuma's EDA scheme [132]. Calculations are greatly simplified because the hydrogen ion has no occupied orbitals; first, because monomers orbitals does not need to be orthogonalized, second, Morokuma's  $E_1$  and  $E_3$  are always equal and third the exchange-repulsion term is always zero.

A first step in Morokuma's EDA consists in calculating the  $\text{Rg}_n$  energy at the  $\text{Rg}_n\text{X}^+$  cluster geometry at HF level,

$$E_0 = \langle \Psi_{\text{Rg}_n}^0 | \hat{H}_{\text{Rg}_n} | \Psi_{\text{Rg}_n}^0 \rangle, \quad (5-8)$$

where  $\Psi_{\text{Rg}_n}^0$  and  $\hat{H}_{\text{Rg}_n}$  are the HF wavefunction and the hamiltonian for the  $\text{Rg}_n$  cluster respectively. In a second step, the energy of  $\text{Rg}_n\text{X}^+$  is evaluated at APMO/HF level with the  $\text{Rg}_n\text{X}^+$  hamiltonian,  $\hat{H}_{\text{Rg}_n\text{X}^+}$ , with three different electronic wavefunctions: the HF wavefunction of  $\text{Rg}_n$  (Eq. 5-9); the relaxed wavefunction of  $\text{Rg}_n$  in the presence of  $\text{X}^+$ ,  $\Psi_{\text{Rg}_n}$  (Eq. 5-10); and the HF wavefunction of  $\text{Rg}_n\text{X}^+$ ,  $\Psi_{\text{Rg}_n\text{X}^+}$  (Eq. 5-11). In these calculations the nuclear wavefunction of  $\text{Rg}_n\text{X}^+$ ,  $\psi_{\text{Rg}_n\text{X}^+}$ , is kept frozen,

$$E_1 = \langle \Psi_{\text{Rg}_n}^0 \psi_{\text{Rg}_n\text{X}^+} | \hat{H}_{\text{Rg}_n\text{X}^+} | \Psi_{\text{Rg}_n}^0 \psi_{\text{Rg}_n\text{X}^+} \rangle, \quad (5-9)$$

$$E_2 = \langle \Psi_{\text{Rg}_n} \psi_{\text{Rg}_n\text{X}^+} | \hat{H}_{\text{Rg}_n\text{X}^+} | \Psi_{\text{Rg}_n} \psi_{\text{Rg}_n\text{X}^+} \rangle, \quad (5-10)$$

$$E_4 = \langle \Psi_{\text{Rg}_n\text{X}^+} \psi_{\text{Rg}_n\text{X}^+} | \hat{H}_{\text{Rg}_n\text{X}^+} | \Psi_{\text{Rg}_n\text{X}^+} \psi_{\text{Rg}_n\text{X}^+} \rangle. \quad (5-11)$$

Employing the  $E_0$ ,  $E_1$ ,  $E_2$  and  $E_4$  energy terms the electrostatic,  $E^{\text{es}}$ , polarization,  $E^{\text{pol}}$ , and charge transfer,  $E^{\text{ct}}$ , energy terms are calculated as

$$E_{\text{Rg}_n\text{X}^+}^{\text{es}} = E_1 - E_0 - \text{HZPE}_{\text{Rg}_n\text{X}^+}, \quad (5-12)$$

$$E_{\text{Rg}_n\text{X}^+}^{\text{pol}} = E_2 - E_1, \quad (5-13)$$

$$E_{\text{Rg}_n\text{X}^+}^{\text{ct}} = E_4 - E_2. \quad (5-14)$$

A dispersion energy term,  $E^{dis}$ , is calculated as the difference between the electronic correlation energy,  $E^{ee}$ , at APMO/MBPT(2)/HPA level of products and reactants.

$$E_{Rg_n X^+}^{dis} = E_{Rg_n X^+}^{ee} - E_{Rg_n}^{ee}. \quad (5-15)$$

A similar term is used in Su and Li EDA [133].

It can be shown that the interaction energy is equal to

$$E_{Rg_n X^+}^{int} = E_{Rg_n X^+}^{es} + E_{Rg_n X^+}^{pol} + E_{Rg_n X^+}^{ct} + E_{Rg_n X^+}^{dis} + E_{Rg_n X^+}^{en}, \quad (5-16)$$

where  $E^{en}$  is the  $Rg_n X^+$  APMO/MBPT(2)/HPA nuclear-electron correlation energy.

Finally, cluster binding energies are analyzed by comparing the EDA terms presented above for the protonation of  $Rg_n$  and  $Rg_{n+1}$  clusters,

$$\begin{aligned} E_{Rg_{n \rightarrow n+1} X^+} = & E_{Rg_{n \rightarrow n+1}} + \Delta HZPE_{Rg_{n \rightarrow n+1} X^+} + \Delta E_{Rg_{n \rightarrow n+1} X^+}^{es} + \\ & \Delta E_{Rg_{n \rightarrow n+1} X^+}^{pol} + \Delta E_{Rg_{n \rightarrow n+1} X^+}^{ct} + \Delta E_{Rg_{n \rightarrow n+1} X^+}^{dis} + \\ & \Delta E_{Rg_{n \rightarrow n+1} X^+}^{en}. \end{aligned} \quad (5-17)$$

In a previous work [129] Ikabata, Imamura and Nakai extended Morokuma-Kitaura and reduced variational space EDA schemes to their nuclear NOMO methodology. These non-Born-Oppenheimer EDA schemes require the construction of several trial wavefunctions mixing monomers orbitals and are general for any molecule or complex. In contrast, the EDA scheme proposed is simpler in the sense that it does not require mixing monomers orbitals but it is limited to systems where a hydrogen ion plays a crucial role in bonding. Ref. [129] EDAs and our EDA include electron-electron and electron-nucleus correlation at the MBPT(2) level.

## 5.3 Results and Discussion

### 5.3.1 $RgX^+$ complexes

Figure 5-1a depicts these systems. APMO/MBPT(2)/HPA binding energies of  $RgX^+$  complexes are presented in Table 5-1 and reveal that rare gas-hydrogen ion bonds are quite strong, being of the same order of magnitude of covalent bonds.

Equilibrium distance data reported in Table 5-1 expose that for  $RgX^+$  complexes the IEs on  $Rg-X$  distances and binding energies follow the trends  $R_{Rg-H} > R_{Rg-D} > R_{Rg-T}$  and  $E_{Rg_{0 \rightarrow 1} H^+} > E_{Rg_{0 \rightarrow 1} D^+} > E_{Rg_{0 \rightarrow 1} T^+}$ . These IEs can be understood in terms of the anharmonicity of the potential and the changes in the zero-point energy of each isotopologue. These trends are in good agreement with those observed in diatomic molecules [134].

In addition to anharmonicity and hydrogen zero-point energy effects, APMO calculations include IEs on the electronic structure of the system. The impact of these IEs on the binding

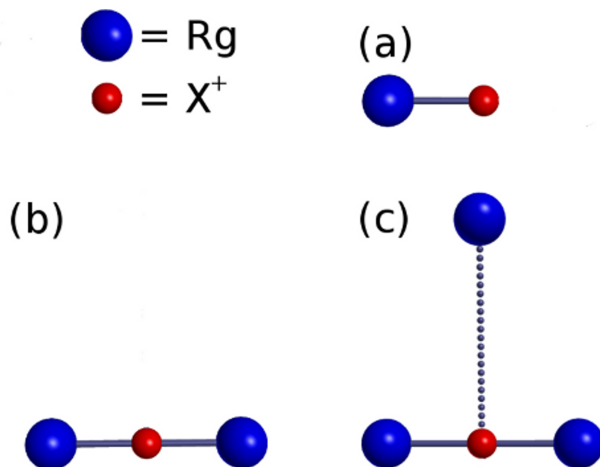


**Figure 5-1:** Schematic illustration of the complexes  $\text{Rg}_n\text{X}^+$  ( $\text{X}=\text{H},\text{D},\text{T}$   $\text{Rg}=\text{He},\text{Ne},\text{Ar}$   $n=1\dots 3$ ). Hydrogen nuclei in red, rare gas nuclei in blue. Hydrogen nuclei are considered as quantum waves and rare gas nuclei as point charges.

**Table 5-1:** APMO/MBPT(2)/HPA equilibrium distances and binding energies for  $\text{RgX}^+$  complexes ( $\text{X}=\text{H},\text{D},\text{T}$   $\text{Rg}=\text{He},\text{Ne},\text{Ar}$ )

	$R_{\text{Rg-X}}/$ (Å)	$E_{\text{Rg}_0 \rightarrow 1\text{X}^+}/$ (kJ mol <sup>-1</sup> )
HeH <sup>+</sup>	0.820	-143.6
HeD <sup>+</sup>	0.804	-156.3
HeT <sup>+</sup>	0.798	-162.3
NeH <sup>+</sup>	1.020	-170.9
NeD <sup>+</sup>	1.007	-183.9
NeT <sup>+</sup>	1.002	-190.0
ArH <sup>+</sup>	1.303	-331.5
ArD <sup>+</sup>	1.292	-347.2
ArT <sup>+</sup>	1.288	-354.5

Calculations were performed with the [aug-cc-pVTZ:5ZSP-DZD] electronic:nuclear basis sets.

energies can be analyzed with the EDA scheme proposed above. EDA results are summarized in Table **5-2**.

An analysis of the data reported in Table **5-2** exposes that the  $\text{HeH}^+$  complex is mainly stabilized by the polarization of the He atom (-187.6 kJ/mol) and the charge transfer from the He to the  $\text{H}^+$  (-51.9 kJ/mol), whereas it is destabilized by the electrostatic interaction between the He and the  $\text{H}^+$  (91.8 kJ/mol) and the hydrogen ZPE (28.5 kJ/mol). We find that  $\text{NeH}^+$  and  $\text{ArH}^+$  complexes are more stable than  $\text{HeH}^+$ , because the polarization (-197.5 kJ/mol and -355.0 kJ/mol respectively) and charge transfer (-70.9 kJ/mol and -134.4 kJ/mol respectively) contributions to the energy are larger. These results are in good agreement with the polarizability trend of the rare gas atoms allowing us to conclude that the Rg-X interaction in  $\text{RgH}^+$  complexes is stabilized mainly by the polarization of the rare gas and in a minor degree by the charge transfer from the Rg to the  $\text{H}^+$ .

EDA calculations for  $\text{X}=\text{H},\text{D},\text{T}$  are also performed to gain a better understanding of the IEs on the electronic structure of  $\text{RgX}^+$  complexes and their impact on the complexes stability. Results presented in Table **5-2** show that hydrogen ZPE decreases as the mass of the isotope increases leading to more localized nuclear wavefunctions, as revealed in Figure **5-2b**. We observe that the polarization energy contribution follow the trend  $\Delta E_{\text{Rg}0\rightarrow 1\text{H}^+}^{\text{pol}} > \Delta E_{\text{Rg}0\rightarrow 1\text{D}^+}^{\text{pol}} > \Delta E_{\text{Rg}0\rightarrow 1\text{T}^+}^{\text{pol}}$ , because a more localized charge density is capable of polarizing more effectively the rare gas electron cloud. In a similar fashion, the charge transfer contribution follows the trend  $\Delta E_{\text{Rg}0\rightarrow 1\text{H}^+}^{\text{ct}} > \Delta E_{\text{Rg}0\rightarrow 1\text{D}^+}^{\text{ct}} > \Delta E_{\text{Rg}0\rightarrow 1\text{T}^+}^{\text{ct}}$ , because heavier nuclei are more electronegative [63]. Figure **5-2a** also displays this charge transfer trend: the electronic density is larger around the heavier hydrogen isotope.

**Table 5-2:** Energy decomposition terms for the reaction  $X^+ + \text{Rg} \rightarrow \text{RgX}^+$  ( $X=\text{H,D,T}$  Rg=He,Ne,Ar). Energies in kJ/mol.

Product	HeH <sup>+</sup>	HeD <sup>+</sup>	HeT <sup>+</sup>	NeH <sup>+</sup>	NeD <sup>+</sup>	NeT <sup>+</sup>	ArH <sup>+</sup>	ArD <sup>+</sup>	ArT <sup>+</sup>
$E_{\text{Rg}_0 \rightarrow 1}$	0.0	0.0	0.0	0.0	0.0	0.0	0.0	0.0	0.0
$\Delta\text{HZPE}_{\text{Rg}_0 \rightarrow 1 \text{X}^+}$	28.5	22.2	18.9	30.0	23.2	19.7	37.8	28.6	24.1
$\Delta E_{\text{Rg}_0 \rightarrow 1 \text{X}^+}^{es}$	91.8	102.6	106.5	96.8	102.8	105.4	159.2	165.9	168.5
$\Delta E_{\text{Rg}_0 \rightarrow 1 \text{X}^+}^{pol}$	-187.6	-201.8	-207.1	-197.5	-207.0	-211.0	-355.0	-365.1	-369.1
$\Delta E_{\text{Rg}_0 \rightarrow 1 \text{X}^+}^{ct}$	-51.9	-59.8	-63.4	-70.9	-79.0	-82.7	-134.4	-144.8	-149.6
$\Delta E_{\text{Rg}_0 \rightarrow 1 \text{X}^+}^{dis}$	-5.6	-6.0	-6.1	-10.0	-10.0	-10.0	-13.7	-13.7	-13.7
$\Delta E_{\text{Rg}_0 \rightarrow 1 \text{X}^+}^{en}$	-18.8	-13.6	-11.2	-19.3	-13.9	-11.3	-25.3	-18.1	-14.7
$E_{\text{Rg}_0 \rightarrow 1 \text{X}^+}$	-143.6	-156.3	-162.3	-170.9	-183.9	-190.0	-331.5	-347.2	-354.5

**Table 5-3:** APMO/MBPT(2)/HPA equilibrium distances and binding energies for  $Rg_2X^+$  complexes ( $X=H,D,T$   $Rg=He,Ne,Ar$ )

	$R_{Rg-X}/$ (Å)	$E_{Rg_1 \rightarrow 2X^+}/$ (kJ mol <sup>-1</sup> )
He <sub>2</sub> H <sup>+</sup>	0.955	-57.2
He <sub>2</sub> D <sup>+</sup>	0.946	-56.6
He <sub>2</sub> T <sup>+</sup>	0.942	-56.3
Ne <sub>2</sub> H <sup>+</sup>	1.166	-79.4
Ne <sub>2</sub> D <sup>+</sup>	1.158	-79.2
Ne <sub>2</sub> T <sup>+</sup>	1.154	-79.1
Ar <sub>2</sub> H <sup>+</sup>	1.514	-85.4
Ar <sub>2</sub> D <sup>+</sup>	1.507	-83.7
Ar <sub>2</sub> T <sup>+</sup>	1.504	-82.9

Calculations were performed with the [aug-cc-pVTZ:5ZSP-DZD] electronic:nuclear basis sets.

### 5.3.2 $Rg_2X^+$ complexes

APMO/MBPT(2)/HPA equilibrium distances and one rare gas atom binding energies for the  $Rg_2X^+$  complexes are presented in Table 5-3. As observed in Figure 5-1b all systems are linear and hydrogen nucleus adopts a centrosymmetric position. Our results are in agreement with previous ones [63, 112–117, 123, 131]. A comparison of the  $RgX^+$  and the  $Rg_2X^+$  results exposes that the coordination of the second rare gas atom leads to the elongation of the  $Rg-X$  bond. It is also observed that the binding energies  $E_{Rg_1 \rightarrow 2X^+}$  are smaller than the corresponding  $E_{Rg_0 \rightarrow 1X^+}$ .

Data presented in Table 5-3 reveals that for  $Rg_2X^+$  complexes the IE on the  $Rg-X$  distance follows the same trend of the  $RgX^+$  complexes, i.e.  $R_{Rg-H} > R_{Rg-D} > R_{Rg-T}$ . However, the binding energy of one rare gas atom,  $E_{Rg_1 \rightarrow 2X^+}$ , follows the opposite trend,  $E_{Rg_1 \rightarrow 2H^+} < E_{Rg_1 \rightarrow 2D^+} < E_{Rg_1 \rightarrow 2T^+}$ . Contrary to chemical intuition this result exposes that the shortening of a  $Rg-X$  bond does not imply its strengthening. We also note that the magnitude of the IEs on binding energies is one order of magnitude smaller when going from  $RgX^+$  to  $Rg_2X^+$  complexes, but the magnitude of the geometric IEs remains the same.

An EDA was conducted for the  $Rg_2X^+$  complexes to gain insight on the origin of the IEs on the binding energies. Results for  $E_{Rg_1 \rightarrow 2X^+}$  are presented in Table 5-4. In the case of the He<sub>2</sub>H<sup>+</sup> complex we found that the polarization term accounts for 81% of the stabilization energy, with small contributions from the charge transfer and dispersion terms. For Ne<sub>2</sub>H<sup>+</sup> complex, the polarization term contributes 66% to the stabilization energy, however in this case the dispersion energy also plays an important role (23%), and there is a small contribution of the charge transfer. Finally, for the Ar<sub>2</sub>H<sup>+</sup> complex the polarization term contributes 50% of the stabilization energy, but the electrostatic and dispersion terms con-

tribute significantly to the stabilization energy (19% and 27% respectively), while the charge transfer term becomes positive.

For all rare gas complexes we found that IEs on the polarization energy, which is the most important contribution to the stabilization energy, follow the same trend of the binding energy, i.e.  $\Delta E_{\text{Rg}_1 \rightarrow 2\text{H}^+}^{\text{pol}} < \Delta E_{\text{Rg}_1 \rightarrow 2\text{D}^+}^{\text{pol}} < \Delta E_{\text{Rg}_1 \rightarrow 2\text{T}^+}^{\text{pol}}$ . These IEs on the polarization contribution can be analyzed in terms of the charge transfer in  $\text{RgX}^+$  complexes: The positive charge over the hydrogen nuclei increases in the order  $q(\text{H})_{\text{RgH}^+} > q(\text{D})_{\text{RgD}^+} > q(\text{T})_{\text{RgT}^+}$ , as the electronegativity of the isotope decreases, as revealed by Figure 5-2a. As a result, the second approaching rare-gas is polarized more effectively by  $\text{RgH}^+$  than  $\text{RgD}^+$  and  $\text{RgT}^+$ .  $\text{Rg}_2\text{H}^+$  complexes can be considered as symmetric hydrogen bonded systems, in which rare gas atoms act as electron donors. Geometric IEs observed in these complexes have also been observed in previous reports on the H/D IEs on symmetric hydrogen bonded complexes [74, 135, 136]. Furthermore, Ref. [74] has revealed that the binding energy is larger for the protium isotopologue of  $[\text{CN-H-NC}]^-$ .

**Table 5-4:** Energy decomposition terms for the reaction  $RgX^+ + Rg \rightarrow Rg_2X^+$  ( $X=H,D,T$   $Rg=He,Ne,Ar$ ). Energies in kJ/mol.

Product	He <sub>2</sub> H <sup>+</sup>	He <sub>2</sub> D <sup>+</sup>	He <sub>2</sub> T <sup>+</sup>	Ne <sub>2</sub> H <sup>+</sup>	Ne <sub>2</sub> D <sup>+</sup>	Ne <sub>2</sub> T <sup>+</sup>	Ar <sub>2</sub> H <sup>+</sup>	Ar <sub>2</sub> D <sup>+</sup>	Ar <sub>2</sub> T <sup>+</sup>
$E_{Rg_1 \rightarrow 2}$	7.5	8.1	8.4	5.1	5.7	6.0	3.6	4.1	4.3
$\Delta HZPE_{Rg_1 \rightarrow 2} X^+$	0.0	-0.5	-0.6	-1.1	-1.3	-1.2	-4.0	-3.2	-2.7
$\Delta E_{Rg_1 \rightarrow 2}^{es} X^+$	4.8	-2.1	-4.0	-1.8	-4.5	-5.5	-18.3	-21.8	-23.0
$\Delta E_{Rg_1 \rightarrow 2}^{pol} X^+$	-56.3	-50.5	-48.9	-56.0	-53.3	-52.3	-48.3	-45.3	-44.2
$\Delta E_{Rg_1 \rightarrow 2}^{ct} X^+$	-7.3	-6.2	-5.8	-5.4	-5.1	-5.0	7.7	9.6	10.4
$\Delta E_{Rg_1 \rightarrow 2}^{dis} X^+$	-4.6	-4.8	-4.9	-19.1	-20.1	-20.5	-26.0	-27.2	-27.7
$\Delta E_{Rg_1 \rightarrow 2}^{en} X^+$	-1.1	-0.7	-0.5	-1.1	-0.7	-0.6	-0.1	0.0	0.0
$E_{Rg_1 \rightarrow 2} X^+$	-57.2	-56.6	-56.3	-79.4	-79.2	-79.1	-85.4	-83.7	-82.9

**Table 5-5:** APMO/MBPT(2)/HPA equilibrium distances and binding energies for  $\text{Rg}_3^+\text{X}$  complexes (X=H,D,T Rg=He,Ne,Ar)

	$R_{\text{Rg-X}}$ (Å)	$R_{\text{Rg}\cdots\text{X}}$ (Å)	$E_{\text{Rg}_2\rightarrow 3\text{X}^+}$ (kJ mol <sup>-1</sup> )
$\text{He}_3\text{H}^+$	0.956	2.130	-3.88
$\text{He}_3\text{D}^+$	0.947	2.142	-3.84
$\text{He}_3\text{T}^+$	0.942	2.146	-3.83
$\text{Ne}_3\text{H}^+$	1.167	2.430	-4.04
$\text{Ne}_3\text{D}^+$	1.159	2.442	-3.99
$\text{Ne}_3\text{T}^+$	1.156	2.447	-3.97
$\text{Ar}_3\text{H}^+$	1.514	3.010	-7.63
$\text{Ar}_3\text{D}^+$	1.508	3.106	-7.59
$\text{Ar}_3\text{T}^+$	1.505	3.110	-7.57

Calculations were performed with the [aug-cc-pVTZ:5ZSP-DZD] electronic:nuclear basis sets.

### 5.3.3 $\text{Rg}_3\text{X}^+$ complexes

We now analyze the calculated equilibrium distances and one rare gas atom binding energies for the  $\text{Rg}_3\text{X}^+$  complexes. As observed in Figure 5-1c these clusters adopt a characteristic T-shape [114, 123]. By comparing the geometry data for  $\text{Rg}_2\text{X}^+$  and the  $\text{Rg}_3\text{X}^+$  results presented in Tables 5-3 and 5-5, we find that the coordination of the third rare gas atom does not affect significantly the Rg-X distance of the other two rare gas atoms. We will refer to the closest two atoms as the first solvation shell and the outermost atom as the second solvation shell. We also find that the binding energy of the second shell rare gas atom,  $E_{\text{Rg}_2\rightarrow 3\text{X}^+}$ , is one order of magnitude smaller than the binding energy of a first solvation shell one,  $E_{\text{Rg}_1\rightarrow 2\text{X}^+}$ .

Table 5-5 presents the IEs data of  $\text{Rg}_3\text{X}^+$  complexes. We observe that the IE on the distance between the hydrogen ion and the first solvation shell rare gas atom is identical to the geometric IE in  $\text{Rg}_2\text{X}^+$  complexes, i.e.  $R_{\text{Rg-H}} > R_{\text{Rg-D}} > R_{\text{Rg-T}}$ . In contrast, the distance between the hydrogen ion and the second shell rare gas atom follows the opposite trend, i.e.  $R_{\text{Rg}\cdots\text{H}} < R_{\text{Rg}\cdots\text{D}} < R_{\text{Rg}\cdots\text{T}}$ . Surprisingly, both geometric IEs are of the same order of magnitude. In contrast, the IEs on the second shell rare gas atom binding energies are very small, being lower than 0.1 kJ/mol, and follow the trend,  $E_{\text{Rg}_2\rightarrow 3\text{H}^+} < E_{\text{Rg}_2\rightarrow 3\text{D}^+} < E_{\text{Rg}_2\rightarrow 3\text{T}^+}$ .

We performed our proposed EDA for the successive binding reaction,  $\text{Rg}_2\text{X}^+ + \text{Rg} \rightarrow \text{Rg}_3\text{X}^+$ . Results presented in Table 5-6 reveal that for all complexes the polarization, which accounts for about 90 % of the former, is the main contribution to the stabilization energy. IEs on the polarization energy are very small, lower than 0.1 kJ/mol, and follow the same trend of the total energy,  $\Delta E_{\text{Rg}_2\rightarrow 3\text{H}^+}^{\text{pol}} < \Delta E_{\text{Rg}_2\rightarrow 3\text{D}^+}^{\text{pol}} < \Delta E_{\text{Rg}_2\rightarrow 3\text{T}^+}^{\text{pol}}$ .

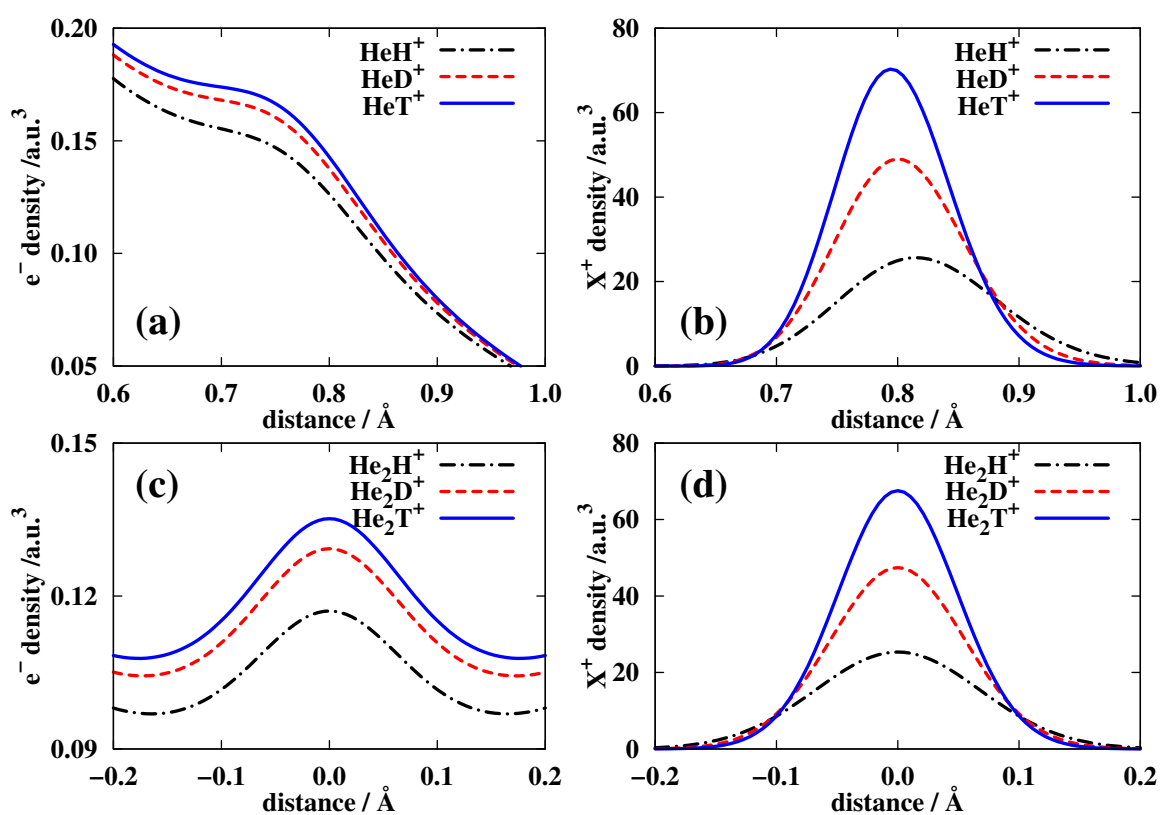


**Figure 5-2:** Electronic (a,c) and nuclear (b,d) densities of  $\text{HeX}^+$  and  $\text{He}_2\text{X}^+$  ( $X=\text{H},\text{D},\text{T}$ ). Plots along the internuclear axis in the regions near the hydrogen nuclei

$\text{Rg}_3\text{X}^+$  complexes can be considered as induced dipole-ion systems, in which the ionic core formed by two rare gas atoms and the hydrogen ion, polarizes the third rare gas atom. Therefore, the observed IEs in the second shell rare gas atom distance and binding energy, can be explained by analyzing the electronic distribution of  $\text{Rg}_2\text{X}^+$  complexes. Figure 5-2c reveals that the electronic density around the hydrogen ion is lower for the protonated isotopologue. Therefore, the positive charge of the ion is screened less effectively in  $\text{Rg}_2\text{H}^+$  complexes, in turn allowing these complexes to polarize more the second shell rare gas atom. The above results reveal that in weakly bonded systems subtle changes in the charge distribution induced by IEs can have a significant impact on the molecular geometries, even if the impact on the binding energies is negligible.

Previous calculations [114] on  $\text{Rg}_n\text{H}^+$  ( $n > 3$ ) clusters revealed that the  $\text{Rg}_2\text{H}^+$  moiety remains almost unperturbed by the addition of more rare gas atoms. These reports also show that the binding energies and distances of the second solvation shell rare gas atoms are very similar to those of the third rare gas atom. Given these similarities, we expect that the geometric and equilibrium IEs on the rare gas atoms in the second solvation shell will be very similar to the IEs already discussed for the  $\text{Rg}_3\text{X}^+$  complexes.

**Table 5-6:** Energy decomposition terms for the reaction  $Rg_2X^+ + Rg \rightarrow Rg_3X^+$  ( $X=H,D,T$ ,  $Rg=He,Ne,Ar$ ). Energies in kJ/mol.

Product	He <sub>3</sub> <sup>+</sup> H	He <sub>3</sub> <sup>+</sup> D	He <sub>3</sub> <sup>+</sup> T	Ne <sub>3</sub> <sup>+</sup> H	Ne <sub>3</sub> <sup>+</sup> D	Ne <sub>3</sub> <sup>+</sup> T	Ar <sub>3</sub> <sup>+</sup> H	Ar <sub>3</sub> <sup>+</sup> D	Ar <sub>3</sub> <sup>+</sup> T
$E_{Rg_2 \rightarrow 3}$	1.32	1.31	1.30	1.20	1.20	1.21	-0.34	-0.34	-0.33
$\Delta HZPE_{Rg_2 \rightarrow 3}X^+$	-0.10	-0.07	-0.03	-0.15	-0.10	-0.08	-0.05	-0.03	-0.02
$\Delta E_{Rg_2 \rightarrow 3}^{es}X^+$	-0.10	-0.07	-0.06	-0.58	-0.57	-0.54	0.14	0.15	0.16
$\Delta E_{Rg_2 \rightarrow 3}^{pol}X^+$	-5.13	-5.07	-5.04	-5.09	-5.06	-5.05	-7.22	-7.19	-7.17
$\Delta E_{Rg_2 \rightarrow 3}^{ct}X^+$	0.45	0.37	0.31	0.53	0.52	0.51	0.54	0.50	0.46
$\Delta E_{Rg_2 \rightarrow 3}^{dis}X^+$	-0.30	-0.29	-0.28	0.01	-0.02	-0.05	-0.69	-0.66	-0.65
$\Delta E_{Rg_2 \rightarrow 3}^{en}X^+$	-0.02	-0.02	-0.02	0.05	0.03	0.02	-0.01	-0.01	-0.01
$E_{Rg_2 \rightarrow 3}X^+$	-3.88	-3.84	-3.83	-4.04	-3.99	-3.97	-7.63	-7.59	-7.57

# 6 Finite Nuclear Mass and Muonic Partial Screening Effects in Muonic Chemistry: A Full-CI study

In this chapter we present a study of different effects produced by replacing one electron with a negative muon on atoms at the full configuration interaction (CI) level of theory.

In previous works we have studied the electronic and muonic structure of muonic atoms with the APMO approach at the HF level [38, 39]. We concluded that an atom with atomic number  $Z$  adopts the electronic properties of the atom with atomic number  $Z - 1$  when one of its electrons is replaced by a muon. Although, this study unveiled some of the qualitative features of atomic systems containing one negative muon some questions remain open, for instance: 1) Is the increase of the nuclear mass the only effect relevant in muonic atom chemistry? 2) How effective is the screening of one positive nuclear charge produced by the muon? 3) How does the presence of a muonic atom affect the energy barriers in a chemical reaction?

With the aim of answering these questions quantitatively, we present a study of atomic muonic systems using the APMO approach at the full-CI (APMO/FCI) level for electrons and muons. Mass effects are considered by including the finite mass correction proposed by Mohallem [137]. The electronic properties of muonic atoms are analyzed in terms of total and ionization energies. We present a detailed analysis of the mass, partial screening, muon relaxation and muon-electron correlation effects on electronic energies of muonic systems. In addition, we present potential energy surfaces (PESs) for  $H_3$  and  $He\mu H_2$  to establish the importance of those effects in chemical reaction energies. Results presented here will be submitted for publication to the Journal of Physical Chemistry A [41]

This chapter is organized as follows. In section 6.1 we summarize the equations of the APMO method and of the finite mass correction. In section 6.2 we provide some computational details. In section 6.3 we present the calculated ionization potentials for muonic atoms and compare these with theoretical and experimental results for regular atoms, as well as the calculated PES for the  $H_2 + H$  reaction and its muonic helium,  $He\mu$ , and “heavy” hydrogen,  ${}^4.1H$ , analogues.

## 6.1 Theory

Here we summarize the expressions of the APMO/HF and APMO/FCI levels of theory [61, 63] for muonic atoms and molecules.

### 6.1.1 APMO theory for muonic systems

The non-relativistic hamiltonian (in atomic units) of a molecular system containing  $N^e$  quantum electrons,  $N^\mu$  quantum muons and  $N^{nuc}$  nuclei expressed in terms of kinetic and potential energy operators is

$$\begin{aligned}
 H_{tot} = & - \sum_i^{N^e} \frac{1}{2} \nabla_i^2 - \sum_i^{N^\mu} \frac{1}{2m_\mu} \nabla_i^2 - \sum_A^{N^{nuc}} \frac{1}{2M_A} \nabla_i^2 + \sum_i^{N^e} \sum_{j>i}^{N^e} \frac{1}{r_{ij}} + \sum_i^{N^\mu} \sum_{j>i}^{N^\mu} \frac{1}{r_{ij}} \\
 & + \sum_A^{N^{nuc}} \sum_{B>A}^{N^{nuc}} \frac{Z_A Z_B}{r_{AB}} + \sum_i^{N^e} \sum_j^{N^\mu} \frac{1}{r_{ij}} - \sum_i^{N^e} \sum_A^{N^{nuc}} \frac{Z_A}{r_{iA}} - \sum_i^{N^\mu} \sum_A^{N^{nuc}} \frac{Z_A}{r_{iA}}.
 \end{aligned} \tag{6-1}$$

where  $m_\mu$  is the muon mass and  $M_A$  and  $Z_A$  are the mass and the charge of the  $A$  nucleus respectively. Considering nuclei as point charges under the BOA the resulting BOA hamiltonian  $H_{BO}$  is equal to  $H_{tot}$  neglecting the nuclear kinetic energy operators.

At the APMO/HF level, the wavefunction of the electron-muon system,  $\Psi_0$ , is expressed as a product of single configurational wavefunctions

$$\Psi_0 = \Phi^e \cdot \Phi^\mu. \tag{6-2}$$

Because of their fermionic nature, electronic and muonic wavefunctions,  $\Phi^e$  and  $\Phi^\mu$ , are represented as Slater determinants of molecular orbitals,  $\psi_i$ .

The molecular wavefunction of a multi-species system at the APMO/FCI approach is given by [44]

$$\Psi_{CI} = \sum_i C_i \Psi_i, \tag{6-3}$$

where  $C_i$  is the coefficient for the  $i$ -th configuration,  $\Psi_i$  is a product of single configurational wavefunctions (as in Eq. 6-2) and the sum runs over all the possible configurations obtained from an APMO/HF reference. The coefficients are obtained by diagonalizing the hamiltonian matrix,  $\mathbf{H}$ . The elements of this matrix are

$$H_{ij} = \langle \Psi_i | \hat{H} | \Psi_j \rangle. \tag{6-4}$$

The correlation energy is calculated as the difference of the CI and HF energies,

$$E_{corr} = \langle \Psi_{CI} | \hat{H} | \Psi_{CI} \rangle - \langle \Psi_0 | \hat{H} | \Psi_0 \rangle. \tag{6-5}$$

### 6.1.2 Finite Nuclear Mass Correction (FNMC)

The use of the BOA for muonic systems leads to large errors in the calculation of total energies [138] because the mass of the  $\mu$  is about 1/9 that of a proton. To correct for these errors, we have used the finite nuclear mass correction (FNMC) proposed by Mohallem [137, 139]. An extension of the FNMC to the APMO equations for electrons and muons is straightforward [39]. After moving from the laboratory reference frame to the molecular reference frame and disregarding small muon-muon, electron-electron non-diagonal and muon-electron cross-terms we arrive at the hamiltonian [139],

$$H_{\text{FNMC}} = H_{\text{BO}} + \sum_A^{N^{\text{nuc}}} P_A \left( \sum_i^{N^e} \frac{\nabla_i^2}{2M_A} + \sum_i^{N^\mu} \frac{\nabla_i^2}{2M_A} \right) P_A, \quad (6-6)$$

where  $P_A$  is a projector operator onto the wavefunction subspace of muonic atom A.

At the APMO/HF level we arrive to a correction matrix,  $\mathbf{Q}^\alpha$ , to each BO Fock matrix [137],

$$\mathbf{F}_{\text{FNMC}}^\alpha = \mathbf{F}^\alpha + \mathbf{Q}^\alpha. \quad (6-7)$$

Electronic and muonic correction matrix elements  $Q_{ijAB}^\alpha$  are related to the corresponding kinetic energy matrix elements  $T_{ijAB}^\alpha$ ,

$$Q_{ijAB}^\alpha = \begin{cases} \frac{m_\alpha}{M_A} T_{ijAB}^\alpha & \text{if } A = B \\ 0 & \text{if } A \neq B, \end{cases} \quad (6-8)$$

$$T_{ijAB}^\alpha = \left\langle \phi_{iA}^\alpha \left| -\frac{\nabla^2}{2m_\alpha} \right| \phi_{jB}^\alpha \right\rangle, \quad (6-9)$$

where  $\phi_{iA}^\alpha$  is a basis function of species  $\alpha$  centered on nucleus A. This correction compares well with the diagonal Born-Oppenheimer correction [137]. We will refer to calculations including this correction as APMO/FNMC calculations .

## 6.2 Computational Details

All calculations have been carried out with a modified version of the LOWDIN computational package[80] considering electrons and muons as quantum particles and nuclei as point charges. New features were implemented to LOWDIN including: 1) A two particle APMO/FCI method for muonic Helium-like atoms; 2) LOWDIN was interfaced with Knowles et al. FCI routine [140] to perform electronic FCI calculations at the APMO level. Calculations including muon-electron correlation are denoted as APMO/FNMC/FCI and calculations including only electron correlation will be called APMO/FNMC/eFCI . Calculations performed within the BOA are referred as infinite nuclear mass limit calculations.

Muonic basis set functions were constructed using an even-tempered scheme following Ref. [38]. Some electronic basis sets were constructed following the same scheme.

Ionization potentials (IP) are calculated as the energy difference,

$$\text{IP}(X^{n+}) = E(X^{n+}) - E(X^{(n+1)+}). \quad (6-10)$$

## 6.3 Results and discussion

The electronic properties of an atom change dramatically after one of its electrons is replaced by a muon. It is commonly believed that the muon orbital is so close to the nucleus that it effectively screens one positive charge of the nucleus. We want to determine the degree of accuracy of this approximation by describing explicitly muons and electrons. We have analyzed four different effects that arise in the electronic ionization of muonic atoms: mass effects, muon screening effect, correlation effects and muon relaxation effect.

### 6.3.1 Nuclear mass effect

When comparing the electronic properties of muonic atoms and regular atoms we must take into account the changes in the nuclear mass. We start by discussing this effect because it is not necessary to describe explicitly the muon to estimate its impact. Following Fleming et al [36] work, a Helium nucleus and a muon can be considered as a pseudonucleus with one positive charge and 4.1 times the mass of a H nucleus. We have studied the impact of these non-BOA effects with the FNMC.

Because the FNMC decreases with the nuclear mass, the largest effect will be observed for hydrogen nuclei. This correction decreases the  $^1\text{H}$  atom IP by 7.3 meV and the IP of muonic helium,  $^4\text{H}$ , by 1.8 meV with respect to the IP of  $^\infty\text{H}$ . Therefore, the difference in the nuclear mass between hydrogen and muonic helium atoms increases the IP of the latter by 5.5 meV. We expect that as the nuclear mass increases this correction will become smaller. We are now in a better position to analyze other effects that depend on a quantum description of the muon, such as the electron-muon correlation, muonic relaxation and the full screening effect approximation. Before doing that we will discuss the error in total energies introduced by our choice of muonic basis sets.

### 6.3.2 Muonic basis set errors

We have calculated the ground state energy of  $^4\text{He}\mu^+$  with different number of s-type GTFs. For this two particle system the FNMC is exact. Table 6-1 reports the results of these calculations. Table 6-1 reveals that the convergence with respect to the basis set size is slow: 37 s-type GTF are required to obtain energies converged to 0.001 meV, which corresponds to 99.999996% of the exact energy. Table 6-1 also reveals that with the even-tempered scheme employed total energy converges to a value 0.043 meV above the exact energy.

Nevertheless, in this work we are interested in electronic energies and properties, therefore in Table 6-2 we are presenting the APMO/FNMC/FCI IP of  $^4\text{He}\mu$  calculated with different

**Table 6-1:** APMO/FNMC/FCI  ${}^4\text{He}\mu^+$  atom total energy with different muonic basis sets.

$\mu$ Basis set	Total energy/eV	percentage
1s	-9290.393488	84.882636%
7s	-10869.986568	99.314751%
13s	-10942.265578	99.975136%
19s	-10944.897428	99.999182%
25s	-10944.983700	99.999970%
31s	-10944.986453	99.999995%
37s	-10944.986540	99.999996%
43s	-10944.986543	99.999996%
49s	-10944.986543	99.999996%
Exact	-10944.986974	100.000000%

**Table 6-2:** APMO/FNMC/FCI  ${}^4\text{He}\mu$  atom IP with different muonic basis sets.

e: $\mu$ Basis set	IP/eV
31s13p:1s	13.604144
31s13p:7s	13.604187
31s13p:13s	13.604183
31s13p:25s	13.604183
31s13p:31s	13.604183
31s13p:49s	13.604192
31s13p:31s13p	13.604200
Accurate <sup>a</sup>	13.604242

<sup>a</sup> Accurate IP calculated from Ref. [141]  ${}^4\text{He}\mu$  energy and  ${}^4\text{He}\mu^+$  exact energy.

muonic basis sets. These calculations were performed with a 31s13p electronic basis set, which allow us to recover 99.999995% of the energy of the H atom. For reference we also present the IP calculated from the difference of Ref. [141] very accurate  ${}^4\text{He}\mu$  energy and the  ${}^4\text{He}\mu^+$  exact energy. Comparing this reference value with our calculations we found that the closest IP (obtained with a 31s13p muonic basis sets) is 0.042 meV below it. However, the IP is not very sensitive to the muonic basis set, for instance the difference between the calculation with 7s and 31s13p is just 0.013 meV.

Careful inspection of Tables **6-1** and **6-2** reveal that the use of small muonic basis sets, for instance a 13s, results in large errors in the total energy, of the order of 2 eV, but small errors in the electronic energy, of the order of 0.060 meV. Therefore in many of the calculations below we will use a 13s muonic basis sets, as we are interested only in the electronic properties.

### 6.3.3 Electron-muon correlation

We now want to establish the magnitude of the muon-electron correlation in muonic atoms. The simplest neutral atom containing one electron and one muon is  ${}^4\text{He}\mu$ . For simplicity we are treating the  ${}^4\text{He}$  nucleus under a BOA approximation assuming infinite mass. Muon-electron correlation energy is calculated by subtracting the APMO/FCI and APMO/HF total energies (eq. 6-5). Energy results using different electronic and muonic basis sets are summarized in Table 6-3.

Given the variational nature of the APMO/FCI method, the result with the largest basis set is expected to be the most accurate. With a 31s25p electronic and a 31s25p muonic basis sets we obtained a muon-electron correlation energy of -0.035 meV. Even with this large basis set this contribution is negligible when compared to the muon-electron interaction.

Muon-electron correlation is small because the overlap between these densities is very small [38], and a mean-field approach gives a good description of their interaction. This is similar to the correlation contributions of core and valence electrons in all-electron molecules, where it is well known that the major contributions come from the valence electrons [86].

For most chemical applications this correlation energy is negligible. For instance if we calculate ionization energies for a particular choice of electronic and muonic basis sets we observe that the muon-electron correlation energy is even lower than the error introduced by our choice of basis sets.

For other muonic systems we do not expect muon-electron correlation to be significantly larger. Consequently, in further calculations for systems with more than one electron, this correlation was neglected and only electron correlation was included.

### 6.3.4 Partial muon screening and muon relaxation effects

We can get an estimate of these two effects by analyzing the electronic and muonic energies of atoms containing one muon and one electron. For simplicity we performed this calculations considering infinite nuclear mass. The muon relaxation energy upon electron removal is defined as the change in the muon kinetic and the muon-nucleus potential energies after the ionization. For all the muonic atoms presented in Table 6-4 we found that the muon relaxation energy is lower than 0.001 meV, and therefore can be neglected.

The muon screening effect can be estimated by comparing the APMO/FCI IPs of hydrogen-like atoms with those of atoms containing one muon and one electron. Again, we consider infinite nuclear mass for simplicity. We present these results in Table 6-4. As expected, the ionization potential of isoelectronic muonic atoms and regular atoms is very similar. In all cases we observe that the IP of the muonic atom is lower than the IP of the regular atom with the same number of electrons. For instance  ${}^\infty\text{He}\mu$  IP is 0.351 meV lower than  ${}^\infty\text{H}$  IP and  ${}^\infty\text{K}\mu^{17+}$  IP is 20.5 meV lower than  ${}^\infty\text{Ar}^{17+}$  IP.

The results discussed above reveal that the muon does not screen perfectly one positive charge from the nucleus. To estimate the magnitude of this imperfect screening we performed the

**Table 6-3:** APMO/FCI infinite mass limit muonic helium,  ${}^{\infty}\text{He}\mu$ , total and muon-electron ( $\mu e$ ) correlation energies.

$e:\mu$ Basis set <sup>a</sup>	APMO/MEFCI $E^{total}/\text{eV}$	APMO/HF $E^{total}/\text{eV}$	$-E_{\mu e}^{corr}/\text{meV}$
1s:1s	-9556.156945	-9556.156945	0.000
3s:3s	-10660.783695	-10660.783695	< 0.001
5s:5s	-11032.436566	-11032.436566	< 0.001
7s:7s	-11183.170371	-11183.170371	< 0.001
9s:9s	-11238.190489	-11238.190489	< 0.001
11s:11s	-11257.148405	-11257.148405	< 0.001
13s:13s	-11263.468694	-11263.468694	< 0.001
15s:15s	-11265.529485	-11265.529485	< 0.001
17s:17s	-11266.195183	-11266.195183	< 0.001
19s:19s	-11266.408094	-11266.408094	< 0.001
21s:21s	-11266.476112	-11266.476112	< 0.001
23s:23s	-11266.497700	-11266.497700	< 0.001
25s:25s	-11266.504569	-11266.504568	< 0.001
27s:27s	-11266.506741	-11266.506741	0.001
29s:29s	-11266.507432	-11266.507431	0.001
31s:31s	-11266.507650	-11266.507649	0.001
31s3p:31s3p	-11266.507650	-11266.507649	0.001
31s7p:31s7p	-11266.507651	-11266.507649	0.002
31s11p:31s11p	-11266.507658	-11266.507649	0.009
31s13p:31s13p	-11266.507666	-11266.507649	0.016
31s17p:31s17p	-11266.507679	-11266.507649	0.030
31s21p:31s21p	-11266.507683	-11266.507649	0.034
31s25p:31s25p	-11266.507684	-11266.507649	0.035

<sup>a</sup> Basis set: [electronic:muonic]

**Table 6-4:** Infinite mass limit APMO/FCI IPs of hydrogen-like atoms and the one-electron muonic atoms in eV. 31s25p:31s25p electronic:muonic basis set.

No. e <sup>-</sup>	Atom	IP	Muonic Atom	IP	$Z_{eff}$	$Z/Z_{eff}$
1	${}^{\infty}\text{H}$	-13.605699	${}^{\infty}\text{He}\mu$	-13.606050	1.000013	0.999987
2	${}^{\infty}\text{He}^+$	-54.422795	${}^{\infty}\text{Li}\mu^+$	-54.423995	2.000022	0.999989
3	${}^{\infty}\text{Li}^{2+}$	-122.451287	${}^{\infty}\text{Be}\mu^{2+}$	-122.453524	3.000027	0.999991
4	${}^{\infty}\text{Be}^{3+}$	-217.691175	${}^{\infty}\text{B}\mu^{3+}$	-217.694531	4.000031	0.999992
5	${}^{\infty}\text{B}^{4+}$	-340.142458	${}^{\infty}\text{C}\mu^{4+}$	-340.146977	5.000033	0.999993
6	${}^{\infty}\text{C}^{5+}$	-489.805137	${}^{\infty}\text{N}\mu^{5+}$	-489.810845	6.000035	0.999994
7	${}^{\infty}\text{N}^{6+}$	-666.679211	${}^{\infty}\text{O}\mu^{6+}$	-666.686123	7.000036	0.999995
8	${}^{\infty}\text{O}^{7+}$	-870.764683	${}^{\infty}\text{F}\mu^{7+}$	-870.772813	8.000037	0.999995
9	${}^{\infty}\text{F}^{8+}$	-1102.061551	${}^{\infty}\text{Ne}\mu^{8+}$	-1102.070904	9.000038	0.999996
10	${}^{\infty}\text{Ne}^{9+}$	-1360.569815	${}^{\infty}\text{Na}\mu^{9+}$	-1360.580397	10.000039	0.999996
11	${}^{\infty}\text{Na}^{10+}$	-1646.289474	${}^{\infty}\text{Mg}\mu^{10+}$	-1646.301292	11.000039	0.999996
12	${}^{\infty}\text{Mg}^{11+}$	-1959.220531	${}^{\infty}\text{Al}\mu^{11+}$	-1959.233584	12.000040	0.999997
13	${}^{\infty}\text{Al}^{12+}$	-2299.362983	${}^{\infty}\text{Si}\mu^{12+}$	-2299.377277	13.000040	0.999997
14	${}^{\infty}\text{Si}^{13+}$	-2666.716832	${}^{\infty}\text{P}\mu^{13+}$	-2666.732367	14.000040	0.999997
15	${}^{\infty}\text{P}^{14+}$	-3061.282077	${}^{\infty}\text{S}\mu^{14+}$	-3061.298857	15.000041	0.999997
16	${}^{\infty}\text{S}^{15+}$	-3483.058717	${}^{\infty}\text{Cl}\mu^{15+}$	-3483.076741	16.000041	0.999997
17	${}^{\infty}\text{Cl}^{16+}$	-3932.046754	${}^{\infty}\text{Ar}\mu^{16+}$	-3932.066025	17.000041	0.999998
18	${}^{\infty}\text{Ar}^{17+}$	-4408.246187	${}^{\infty}\text{K}\mu^{17+}$	-4408.266705	18.000041	0.999998

following analysis: For hydrogen-like atoms at the infinite nuclear mass limit the exact IP depends only on the nuclear charge. Therefore if we compare the IPs of a hydrogen-like atom A and the H atom we find that

$$\frac{\text{IP}_A}{\text{IP}_H} = Z_A^2. \quad (6-11)$$

Given that one-electron muonic atoms IP are very close to the total energies of isoelectronic regular atoms, we may use the above relation to calculate an effective pseudonucleus,  $X\mu$ , charge:

$$Z_{X\mu}^{eff} = \sqrt{\frac{\text{IP}_{X\mu}}{\text{IP}_H}}. \quad (6-12)$$

In Table **6-1** we present the effective charges obtained from one-electron muonic atoms. As expected from the IP results, the effective charge of the muon+nucleus pseudonucleus is a little bit higher than the charge of the regular nucleus with  $Z-1$ .

Now, if we compare the charges of the isoelectronic muonic and regular atoms we obtain a number that shows how similar those nucleus are from the electrons perspective,

$$\frac{Z_Y}{Z_{X\mu}^{eff}} = \sqrt{\frac{\text{IP}_Y}{\text{IP}_{X\mu}}}. \quad (6-13)$$

The closer this ratio to one, the more similar the electronic properties of both all-electron and muonic atom are expected to be. In Table **6-1** we include the results for this ratio. From those results we can conclude that as  $Z$  increases the transmutation of the electronic properties induced by the screening of the muon is more effective.

### 6.3.5 Combined effects in IP

A simple way to assess quantitatively the mass and screening effects on electronic properties of atoms is by contrasting the IPs of muonic atoms and those of all electronic counterparts at a APMO/FNMC/eFCI level. These results are presented in Table **6-5**. In previous works we have reported IPs for muonic atoms with  $Z=2-19$  and regular atoms with  $Z=1-18$  calculated at the translation-free APMO/HF and APMO/FNMC propagator theory of second order [38, 39], showing that the IP of a muonic atom with atomic number  $Z$  is almost equal to that of a regular atom with atomic number  $Z-1$ . As observed in Table **6-5** qualitative results remain, the IP of a muonic atom with atomic number  $Z$  is almost equal to that of a regular atom with atomic number  $Z-1$ .

We observe that the APMO/FNMC/eFCI average absolute deviation (0.152 eV) is lower than the translation-free APMO/HF (0.441 eV) and APMO/FNMC propagator theory of second order (0.292 eV) previously reported [38, 39]. Also, the difference between IPs from muonic and regular atoms is smaller than those presented in ref [38]. Figure **6-1** shows IPs

**Table 6-5:** APMO/FNMC/eFCI IPs of regular and muonic atoms in eV. Differences between isoelectronic muonic and regular atoms IPs in meV. cc-pVTZ 13s electronic and muonic basis sets were used. Experimental IPs for regular atoms were included for comparison.

No.	Regular atoms IP			Muonic atoms IP		$\Delta_{\text{Muonic-Regular}}$
	$e^-$ atom	APMO/FNMC/FCI	exp <sup>a</sup>	atom	APMO/FNMC/FCI	$\Delta_{\text{APMO/FNMC/FCI}}$
1	<sup>1</sup> H	13.593	13.598	<sup>4</sup> He $\mu$	13.597	4.4
2	<sup>4</sup> He	24.524	24.587	<sup>7</sup> Li $\mu$	24.526	2.9
3	<sup>7</sup> Li	5.342	5.392	<sup>9</sup> Be $\mu$	5.342	0.4
4	<sup>9</sup> Be	9.287	9.323	<sup>11</sup> B $\mu$	9.287	0.5
5	<sup>11</sup> B	8.211	8.298	<sup>12</sup> C $\mu$	8.212	0.2
6	<sup>12</sup> C	11.163	11.260	<sup>14</sup> N $\mu$	11.163	0.3
7	<sup>14</sup> N	14.427	14.534	<sup>16</sup> O $\mu$	14.427	0.1
8	<sup>16</sup> O	13.314	13.618	<sup>19</sup> F $\mu$	13.314	-0.2
9	<sup>19</sup> F	17.129	17.423	<sup>20</sup> Ne $\mu$	17.129	-0.1
10	<sup>20</sup> Ne	21.111	21.565	<sup>23</sup> Na $\mu$	21.111	-0.3
11	<sup>23</sup> Na	4.952	5.139	<sup>24</sup> Mg $\mu$	4.953	0.8
12	<sup>24</sup> Mg	7.527	7.646	<sup>27</sup> Al $\mu$	7.528	0.3
13	<sup>27</sup> Al	5.948	5.986	<sup>28</sup> Si $\mu$	5.948	-0.2
14	<sup>28</sup> Si	8.114	8.152	<sup>31</sup> P $\mu$	8.114	0.1
15	<sup>31</sup> P	10.456	10.487	<sup>32</sup> S $\mu$	10.456	0.2
16	<sup>32</sup> S	10.094	10.360	<sup>35</sup> Cl $\mu$	10.093	-0.2
17	<sup>35</sup> Cl	12.703	12.968	<sup>40</sup> Ar $\mu$	12.703	-0.9
18	<sup>40</sup> Ar	15.465	15.760	<sup>39</sup> K $\mu$	15.465	-0.1
	aad <sup>b</sup>	0.152				

<sup>a</sup> Experimental values taken from Ref. [142]

<sup>b</sup> Average absolute deviation with respect to the experimental values

for muonic and regular atoms. This figure shows clearly the well-known behavior that the IPs of muonic atoms are shifted to the left by one atomic number and the aforementioned improvement of IPs.

### 6.3.6 Combined effects in reaction energies

We have calculated the PES for the colinear reaction between muonic helium and a hydrogen molecule at the APMO/FNMC/eFCI level. Our goal is to determine the impact of the nuclear mass and the partial muonic screening in the reaction barrier. For the calculation of the PES we assumed that atoms A and B are bonded and atom C is moving towards B in a collinear trajectory. We considered the distances between atom A and B,  $R_1$ , and between

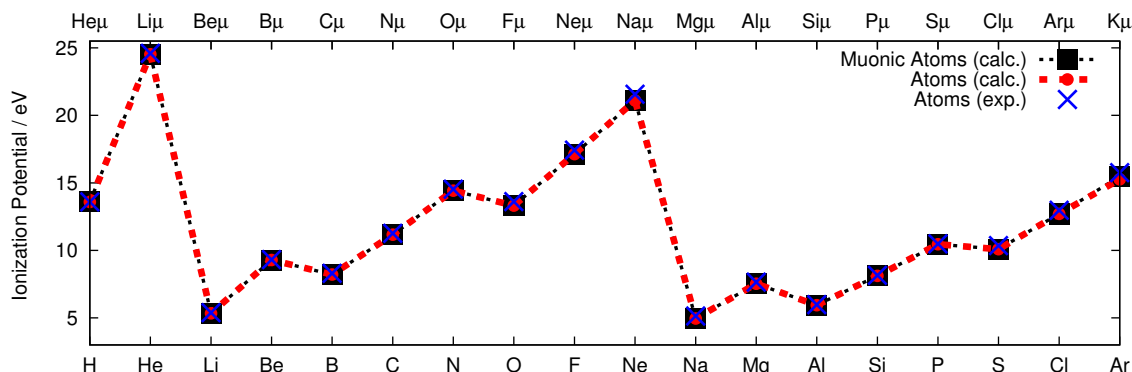


**Figure 6-1:** FNMC/APMO/eFCI ionization potentials for regular and muonic atoms

B and C,  $R_2$  as coordinates. The obtained PES is presented in Figure 6-2.

To determine the effect of the partial muonic screening we have calculated the PESs for the  ${}^{\infty}\text{H}_2 + {}^{\infty}\text{H}$  and  ${}^{\infty}\text{H}_2 + {}^{\infty}\text{He}\mu$  reactions assuming infinite nuclear mass. Under this approximation the difference between both reaction barriers can be attributed only to the partial muon screening. Results presented in Table 6-6 reveal that the partial muon screening reduces the reaction barrier by 0.847 meV. This effect is small but should be taken into account if very accurate calculations are needed.

Following the same lines, to determine the effect of finite nuclear mass we have calculated the PESs for the  ${}^1\text{H}_2 + {}^4\text{H}$  and compared it to the infinite mass PES. The difference between both reaction barriers is caused by the inclusion of the FNMC. Results presented in Table 6-6 reveal that considering the finite nuclear mass increases the reaction barrier by 0.954 meV. Fleming et al using a diagonal BO correction found that the inclusion of the finite nuclear mass increases the reaction barrier by 5.637 meV. Therefore, although our FNMC predicts correctly that the reaction barrier should increase, it underestimates the impact of the finite mass on the  $\text{H}_2 + \text{H}$  reaction barrier.

When we compare the barrier presented in Table 6-6 for the original  $\text{H}_2 + {}^4\text{He}\mu$  reaction with the infinite mass  $\text{H}_2 + \text{H}$  PES we find that the former is higher by 0.115 meV. If we add the estimates for the partial screening effect (-0.847 meV) and the finite nuclear mass (0.954 meV) we obtain an expected change in the energy barrier of 0.107 meV. The good agreement between those two values allow us to conclude that the two effects discussed so far give a good description of the chemistry of muonic helium.

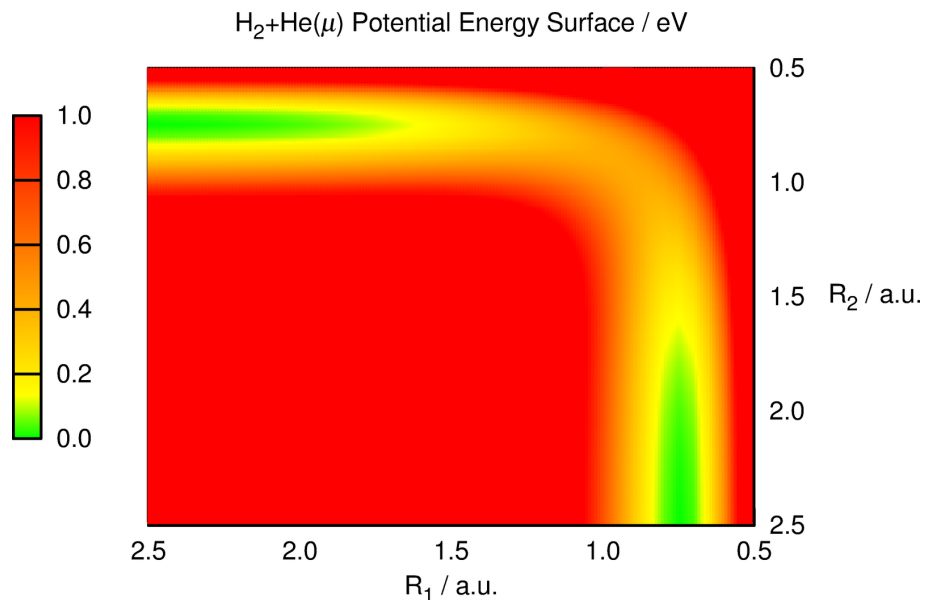


**Figure 6-2:** APMO/FNMC/eFCI PES for  ${}^1\text{H}_2 + {}^4\text{He}\mu$  reaction. PESs for  ${}^\infty\text{H}_2 + {}^\infty\text{H}$ ,  ${}^\infty\text{H}_2 + {}^\infty\text{He}\mu$ ,  ${}^1\text{H}_2 + {}^1\text{H}$ ,  ${}^1\text{H}_2 + {}^4\text{H}$  reaction are identical to the naked eye.

**Table 6-6:** Transition state coordinates and reaction barriers for the  ${}^4\text{He}\mu + \text{H}_2$  and  $\text{H} + \text{H}_2$  reactions.

reaction	$R_1$ T.S. / a.u.	$R_2$ T.S. / a.u.	Barrier / eV
${}^\infty\text{H}_2 + {}^\infty\text{H}$	0.9304	0.9304	0.429979
${}^\infty\text{H}_2 + {}^\infty\text{He}\mu$	0.9305	0.9308	0.429132
${}^1\text{H}_2 + {}^4\text{H}$	0.9305	0.9307	0.430932
${}^1\text{H}_2 + {}^4\text{He}\mu$	0.9307	0.9310	0.430094

FNMC-APMO/FCI calculations using the cc-pVTZ electronic basis set and a 13s muonic basis set.

## 7 Conclusions

In this work, we have presented theoretical developments of the APMO method to reduce its computational cost and to include interparticle correlation, as well as APMO applications to the study of NQEs and muonic chemistry. In this section we summarize our findings.

In chapter 2 we presented APMO/DFT equations implemented on the LOWDIN code, including the CS-type nuclear-electron correlation functional proposed by Nakai [55]. The inclusion of nuclear-electron correlation improves the accuracy of the proton affinities predicted with the APMO method.

In chapter 3 we have proposed the APMO/ADFT/HPA and APMO/ADFT methods and implemented them on the LOWDIN code. The APMO/ADFT/HPA method combines the advantages in efficiency electronic ADFT and nuclear LHP. Tests calculations performed on a series of small molecules to determine the impact of the APMO/ADFT/HPA approximations on the molecular properties revealed that the magnitudes of the errors in energies and geometries are small and comparable to those obtained with the electronic ADFT. In the APMO/ADFT method, nuclear auxiliary densities are required to evaluate the nuclear-electron correlation functional. A method to generate suitable auxiliary nuclear basis sets was presented. It was found that APMO/ADFT nuclear-electron energies are around 5% larger than previously reported calculations. However, these differences do not have a significant impact on chemical properties such as proton affinities. The scaling behavior of both methods was tested on HF chains. It was found that APMO/ADFT/HPA and APMO/ADFT methods presented cubic scaling with respect to the size of the systems as opposed to the quartic scaling of the APMO/HF/HPA or APMO/DFT methods. Even for medium size molecules, this reduction in the scaling results in speedups of 5x and more with respect to APMO/HF/HPA calculations. These methodologies open the possibility of studying nuclear quantum effects on large size systems that otherwise would be impractical.

In chapter 4 we have described an alternative second-order many-body perturbation theory for the Any Particle Molecular Orbital method. In this approach, the reference wave function is constructed as a product of Slater determinants for the lighter species (electrons) and Hartree products of localized nuclear orbitals for the heavier species (muons, nuclei). Calculations on hydrogen-bonded dimers and the hydrogen molecule revealed that the Hartree product approximation has an impact on the MBPT(2) energies. An analysis of the correlation energy contributions showed that the HPA increases the amount of nuclear-electron correlation recovered by the MBPT(2) calculation. Application of the new approach on hydrogen fluoride chains of different length revealed that the HPA reduces the computational

---

costs of the MBPT(2) calculation, because it lowers the formal scaling of the nuclear-electron and nuclear-nuclear integral transformations. Application of the APMO/MBPT(2) method to muonic helium and lithium atoms and a muonic helium dimer reveals that the muon-electron correlation is of the order of  $10^{-6}$  a.u., and therefore can be neglected in the study of the muonic atoms chemistry.

In this chapter we also have proposed a simple nuclear-electron correlation functional from APMO/MBPT(2)/HPA correlation energies. The deviation of the energies calculated with the proposed approximated functional are lower than chemical accuracy (1 kcal/mol). The computational cost of this approximated functional is lower than the APMO/MBPT(2)/HPA method cost.

In chapter 5 we proposed an EDA scheme for the APMO/MBPT(2)/HPA method based on protonation reactions, to gain insight on the impact of nuclear quantum effects in rare gas-hydrogen ion bonding. With this methodology we studied the H/D/T IEs in geometry and binding energies of small protonated rare gas clusters. For  $\text{RgX}^+$  ions our results reveal that the Rg-X bond is formed due to polarization and charge transfer contributions. These energy terms are larger in the heavier isotopologues. In the case of  $\text{Rg}_2\text{X}^+$  complexes, we found that polarization is the main contribution to the Rg-X bond, and that the lighter isotopologues are the most stable. In these complexes substitution of a proton with a heavier nucleus results in a shortening and weakening of the Rg-X bond.  $\text{Rg}_3\text{X}^+$  complexes are formed by a  $\text{Rg}_2\text{X}^+$  core that polarizes the third rare gas atom. The IEs on the binding energy of the latter rare gas atom are almost negligible. Nevertheless, our results reveal that subtle changes in the charge distribution of the  $\text{Rg}_2\text{X}^+$  core induced by an isotopic substitution have an impact on the geometry of the  $\text{Rg}_3\text{X}^+$  complex.

In chapter 6 we have investigated different effects produced by replacing one electron with a negative muon on atoms with  $Z=1-18$  with the APMO method at FCI level of theory. We included nuclear mass effects using the finite nuclear mass correction proposed by Mohallem. We used version of the LOWDIN code interfaced with FCI program from Knowles et al. Our results reveal that the chemistry of a muonic atom is very similar to that of a regular atom with  $Z-1$ . The difference in the ionization potentials of isoelectronic muonic atoms and regular atoms is of the order of meV. This difference can be attributed to two effects: (1) The increase in nuclear mass and (2) the imperfect muonic screening of the positive charge. The former effect is usually larger than the second one, and the impact of both of them decrease as  $Z$  increases. Our calculations also reveal that muon-electron correlation and muon relaxation upon electronic removal are very small and can be neglected in the calculation of chemical properties.

Also in chapter 6 we quantified the partial muonic screening effect and the finite nuclear mass effect on the energy barrier of the  $\text{H}_2 + {}^4\text{He}\mu$  reaction. Compared to the infinite mass  $\text{H}_2 + \text{H}$  reaction barrier, the partial muonic screening effect reduces the energy barrier by 0.847 meV, and the finite nuclear mass effect increases it by 0.954 meV. Comparison with calculations performed with the diagonal BO correction reveal that the FNMC underestimates the finite

nuclear mass effect on this reaction barrier by a factor of 5 [36]. Nevertheless, this analysis yielded a value for the muonic effect which is independent of the mass correction employed. Although the partial muonic screening effect is small for most chemical applications, it should be considered for precise calculations aiming for spectroscopical accuracy.

# Bibliography

- [1] Q. Peng, X. Zhang, L. Hung, E. A. Carter, and G. Lu, *Phys. Rev. B* **78**, 054118 (2008).
- [2] H. Nakai, *Int. J. Quantum Chem.* **107**, 2849 (2007).
- [3] T. Ishimoto, M. Tachikawa, and U. Nagashima, *Int. J. Quantum Chem.* **109**, 2677 (2009).
- [4] T. Udagawa and M. Tachikawa, *Multi-Component Molecular Orbital Theory* (Nova Science Publishers, New York, 2009).
- [5] Y. Jean, P. Mallon, and D. Schrader, *Principles and applications of positron & positronium chemistry* (World Scientific, 2003).
- [6] K. Nagamine, *Introductory muon science* (Cambridge University Press, 2003).
- [7] P. Froelich, *Adv. Phys.* **41**, 405 (1992).
- [8] K. Ishida, K. Nagamine, T. Matsuzaki, and N. Kawamura, *J. Phys. G: Nucl. Part. Phys.* **29**, 2043 (2003).
- [9] J. Cohen, *Rep. Prog. Phys.* **67**, 1769 (2004).
- [10] W. Breunlich, P. Kammel, J. Cohen, and M. Leon, *Annu. Rev. Nucl. Part. S.* **39**, 311 (1989).
- [11] R. Gheisari, *Nucl. Instrum. Meth. A* **634**, 1 (2011).
- [12] S. G. Karshenboim, *Phys. Rep.* **422**, 1 (2005).
- [13] R. Pohl, A. Antognini, F. Nez, F. Amaro, F. Biraben, J. Cardoso, D. Covita, A. Dax, S. Dhawan, and L. Fernandes, *Nature* **466**, 213 (2010).
- [14] D. Gotta, *Prog. Part. Nucl. Phys.* **52**, 133 (2004).
- [15] E. Armour and W. Brown, *Acc. Chem. Res.* **26**, 168 (1993).
- [16] M. I. Eides, H. Grotch, and V. A. Shelyuto, *Phys. Rep.* **342**, 63 (2001).

- 
- [17] K. Shirazi, *Chaos, Solitons Fractals* **36**, 1232 (2008).
- [18] A. Frolov, *J. Phys. B: At. Mol. Opt. Phys.* **37**, 4517 (2004).
- [19] J. Cohen, *Phys. Rev. A* **59**, 1160 (1999).
- [20] W. Czapliński, J. Gronowski, W. Kamiński, and N. Popov, *Phys. Lett. A* **375**, 155 (2010).
- [21] B. Fricke, *Phys. Rev. Lett.* **30**, 119 (1973).
- [22] W. Bian, X. Zhao, Y. Wang, and Y. Wang, *Chem. Phys.* **242**, 195 (1999).
- [23] M. Eskandari, B. Rezaie, and S. Mohammadi, *Mod. Phys. Lett. B* **19**, 889 (2005).
- [24] A. Krutov and A. Martynenko, *Phys. Rev. A* **78**, 032513 (2008).
- [25] A. Frolov and D. Wardlaw, *Eur. Phys. J. D* **63**, 1 (2010).
- [26] A. Frolov and D. Wardlaw, *Phys. Rev. A* **81**, 062504 (2010).
- [27] K. Rodriguez, L. Ancarani, G. Gasaneo, and D. Mitnik, *Int. J. Quantum Chem.* **110**, 1820 (2010).
- [28] T. Yamazaki, K. Nagamine, S. Nagamiya, O. Hashimoto, K. Sugimoto, K. Nakai, and S. Kobayashi, *Phys. Scr.* **11**, 133 (1975).
- [29] K. Nagamine, *Hyperfine Interact.* **6**, 347 (1979).
- [30] T. Yamazaki, *Hyperfine Interact.* **8**, 463 (1981).
- [31] E. Torikai, K. Nagamine, K. Nishiyama, E. Hirose, P. Birrer, I. Tanaka, H. Kojima, S. Srinivas, T. Das, and S. Maekawa, *Hyperfine Interact.* **97-98**, 387 (1996).
- [32] T. Mamedov, D. Andrianov, D. Gerlach, K. Gritsai, V. Gorelkin, O. Cormann, J. Major, A. Stoikov, M. Shevchik, and U. Zimmerman, *JETP Lett.* **71**, 438 (2000).
- [33] J. V. Mallow, J. P. Desclaux, and A. J. Freeman, *Phys. Rev. A* **17**, 1804 (1978).
- [34] J. V. Mallow, J. P. Desclaux, A. J. Freeman, and M. Weinert, *Hyperfine Interact.* **8**, 455 (1981).
- [35] D. J. Arseneau, D. G. Fleming, O. Sukhorukov, J. H. Brewer, B. C. Garrett, and D. G. Truhlar, *Physica B* **404**, 946 (2009).
- [36] D. Fleming, D. Arseneau, O. Sukhorukov, J. Brewer, S. Mielke, G. Schatz, B. Garrett, K. Peterson, and D. Truhlar, *Science* **331**, 448 (2011).

- [37] D. G. Fleming, D. J. Arseneau, O. Sukhorukov, J. H. Brewer, S. L. Mielke, D. G. Truhlar, G. C. Schatz, B. C. Garrett, and K. A. Peterson, *J. Chem. Phys.* **135**, 184310 (2011).
- [38] F. Moncada, D. Cruz, and A. Reyes, *Chem. Phys. Lett.* **539-540**, 209 (2012).
- [39] F. Moncada, D. Cruz, and A. Reyes, *Chem. Phys. Lett.* **570**, 16 (2013).
- [40] F. Moncada, S. González, R. Flores-Moreno, and A. Reyes, *Mol. Phys.* **submitted** (2013).
- [41] E. Posada, F. Moncada, and A. Reyes, *J. Chem. Phys. A*. **In preparation** (2013).
- [42] M. Tachikawa, K. Mori, H. Nakai, and K. Iguchi, *Chem. Phys. Lett.* **290**, 437 (1998).
- [43] H. Nakai, *Int. J. Quantum Chem.* **86**, 511 (2002).
- [44] M. Tachikawa, *Chem. Phys. Lett.* **360**, 494 (2002).
- [45] S. Webb, T. Iordanov, and S. Hammes-Schiffer, *J. Chem. Phys.* **117**, 4106 (2002).
- [46] H. Nakai and K. Sodeyama, *J. Chem. Phys.* **118**, 1119 (2003).
- [47] C. Swalina, M. Pak, and S. Hammes-Schiffer, *Chem. Phys. Lett.* **404**, 394 (2005).
- [48] T. Ishimoto, M. Tachikawa, and U. Nagashima, *J. Chem. Phys.* **125**, 4103 (2006).
- [49] M. Hoshino and H. Nakai, *J. Chem. Phys.* **124**, 194110 (2006).
- [50] M. Tachikawa and Y. Osamura, *J. Chem. Phys.* **113**, 4942 (2000).
- [51] T. Ishimoto, M. Tachikawa, and U. Nagashima, *J. Chem. Phys.* **128**, 164118 (2008).
- [52] A. Chakraborty, M. V. Pak, and S. Hammes-Schiffer, *J. Chem. Phys.* **129**, 014101 (2008).
- [53] M. Hoshino, H. Nishizawa, and H. Nakai, *J. Chem. Phys.* **135**, 024111 (2011).
- [54] T. Udagawa and M. Tachikawa, *J. Chem. Phys.* **125**, 244105 (2006).
- [55] Y. Imamura, H. Kiryu, and H. Nakai, *J. Comput. Chem.* **29**, 735 (2008).
- [56] M. V. Pak, A. Chakraborty, and S. Hammes-Schiffer, *J. Phys. Chem. A* **111**, 4522 (2007).
- [57] A. Chakraborty, M. V. Pak, and S. Hammes-Schiffer, *Phys. Rev. Lett.* **101**, 153001 (2008).

- 
- [58] M. Hoshino, Y. Tsukamoto, and H. Nakai, *Int. J. Quantum Chem.* **107**, 2575 (2007).
- [59] T. Udagawa, T. Ishimoto, H. Tokiwa, M. Tachikawa, and U. Nagashima, *J. Phys. Chem. A* **110**, 7279 (2006).
- [60] H. Nakai, Y. Iwabata, Y. Tsukamoto, Y. Imamura, K. Miyamoto, and M. Hoshino, *Mol. Phys.* **105**, 2649 (2007).
- [61] S. González, N. Aguirre, and A. Reyes, *Int. J. Quantum Chem.* **108**, 1742 (2008).
- [62] M. Kaneko, T. Udagawa, and M. Tachikawa, *J. Comput. Chem., Jpn.* **9**, 21 (2010).
- [63] S. González and A. Reyes, *Int. J. Quantum Chem.* **110**, 689 (2010).
- [64] D. V. Moreno, S. A. González, and A. Reyes, *J. Phys. Chem. A* **114**, 9231 (2010).
- [65] F. Moncada, L. S. Uribe, J. Romero, and A. Reyes, *Int. J. Quantum Chem.* **113**, 1556 (2013).
- [66] Y. Kikuta, T. Ishimoto, and U. Nagashima, *Bull. Chem. Soc. Jpn.* **81**, 820 (2008).
- [67] T. Ishimoto, Y. Ishihara, H. Teramae, M. Baba, and U. Nagashima, *J. Chem. Phys.* **128**, 184309 (2008).
- [68] J. Romero, E. Posada, R. Flores-Moreno, and A. Reyes, *J. Chem. Phys.* **137**, 074105 (2012).
- [69] M. Diaz-Tinoco, J. Romero, J. V. Ortiz, A. Reyes, and R. Flores-Moreno, *J. Chem. Phys.* **138**, 194108 (2013).
- [70] M. Tachikawa, T. Ishimoto, H. Tokiwa, H. Kasatani, and K. Deguchi, *Ferroelectrics* **268**, 3 (2002).
- [71] M. Tachikawa, *Integrated Ferroelectrics* **100**, 72 (2008).
- [72] F. Moncada, S. González, and A. Reyes, *Mol. Phys.* **108**, 1545 (2010).
- [73] Y. Kita and M. Tachikawa, *J. Mol. Struct.: THEOCHEM* **912**, 2 (2009).
- [74] D. V. Moreno, S. A. González, and A. Reyes, *J. Chem. Phys.* **134**, 024115 (2011).
- [75] B. I. Dunlap, J. W. D. Connolly, and J. R. Sabin, *J. Chem. Phys.* **71**, 4993 (1979).
- [76] J. W. Mintmire and B. I. Dunlap, *Phys. Rev. A* **25**, 88 (1982).
- [77] K. Eichkorn, O. Treutler, H. Öhm, M. Höser, and R. Ahlrichs, *Chem. Phys. Lett.* **240**, 283 (1995).

- [78] B. Dunlap, *J. Mol. Struct.: THEOCHEM* **529**, 37 (2000).
- [79] A. M. Köster, *J. Chem. Phys.* **118**, 9943 (2003).
- [80] R. Flores-Moreno, E. Posada, F. Moncada, J. Romero, J. Charry, M. A. Díaz-Tinoco, S. A. González, N. Aguirre, and A. Reyes, *Int. J. Quantum Chem.* **accepted** (2013).
- [81] J. F. Capitani, R. F. Nalewajski, and R. G. Parr, *J. Chem. Phys.* **76**, 568 (1982).
- [82] N. Gidopoulos, *Phys. Rev. B* **57**, 2146 (1998).
- [83] S. F. Sousa, P. A. Fernandes, and M. J. Ramos, *J. Phys. Chem. A* **111**, 10439 (2007).
- [84] A. Reyes, M. Pak, and S. Hammes-Schiffer, *J. Chem. Phys.* **123**, 064104 (2005).
- [85] B. Auer and S. Hammes-Schiffer, *J. Chem. Phys.* **132**, 084110 (2010).
- [86] A. Szabo and N. Ostlund, *Modern quantum chemistry: introduction to advanced electronic structure theory* (Dover Publications, 1996).
- [87] A. Sirjoosingh, M. V. Pak, and S. Hammes-Schiffer, *J. Chem. Theory Comput.* **7**, 2689 (2011), <http://pubs.acs.org/doi/pdf/10.1021/ct200473r>.
- [88] J. T.H. Dunning, *J. Chem. Phys.* **90**, 1007 (1989).
- [89] D. Woon and J. T.H. Dunning, *J. Chem. Phys.* **100**, 2975 (1994).
- [90] D. Woon and J. T.H. Dunning, *J. Chem. Phys.* **98**, 1358 (1993).
- [91] W. L. Jolly, *Modern Inorganic Chemistry*, 2nd edition ed. (McGraw-Hill, New York, 1991).
- [92] C. Cramer, *Essentials of computational chemistry: theories and models* (Wiley, 2004).
- [93] D. N. Laikov, *Chem. Phys. Lett.* **281**, 151 (1997).
- [94] A. M. Köster, J. U. Reveles, and J. M. del Campo, *J. Chem. Phys.* **121**, 3417 (2004).
- [95] F. Janetzko, A. Goursot, T. Mineva, P. Calaminici, R. Flores-Moreno, A. M. Köster, and D. R. Salahub, Cluster structures: Bridging experiment and theory, in *Nanoclusters - A Bridge Across Disciplines, Chapter II. Structures: Interfacing Theory and Experiment*, edited by P. Jena and A. Castleman Jr., chap. 4, pp. 151–218, Elsevier, Amsterdam, The Netherlands, 2010.
- [96] F. Moncada, E. Posada, R. Flores-Moreno, and A. Reyes, *Chemical Physics* **400**, 103 (2012).

- 
- [97] J. Charry, F. Moncada, R. Flores-Moreno, and A. Reyes, Chemical Physics **In preparation** (2013).
- [98] J. W. Mintmire, J. R. Sabin, and S. B. Trickey, Phys. Rev. B **26**, 1743 (1982).
- [99] A. Köster, P. Calaminici, Z. Gomez, and J. Reveles, Density functional theory calculation of transition metal clusters, in *Reviews in Modern Quantum Chemistry (A Celebration of the contributions of Robert G. Parr)*, edited by K. D. Sen, World Scientific, Singapore, 2002.
- [100] P. Dirac, Proc. R. Soc. London, Ser. A **123**, 714 (1929).
- [101] J. C. Slater, Phys. Rev. **81**, 385 (1951).
- [102] S. Vosko, L. Wilk, and M. Nusair, Can. J. Phys. **58**, 1200 (1980).
- [103] R. Krishnan, J. S. Binkley, R. Seeger, and J. A. Pople, J. Chem. Phys. **72**, 650 (1980).
- [104] W. J. Hehre, R. Ditchfield, and J. A. Pople, J. Chem. Phys. **56**, 2257 (1972).
- [105] P. Calaminici, F. Janetzko, A. M. Köster, R. Mejía-Olvera, and B. Zuñiga-Gutierrez, J. Chem. Phys. **126**, 044108 (2007).
- [106] M. Cafiero, S. Bubin, and L. Adamowicz, Phys. Chem. Chem. Phys. **5**, 1491 (2003).
- [107] W. J. Hehre, R. F. Stewart, and J. A. Pople, J. Chem. Phys. **51**, 2657 (1969).
- [108] S. Yamamoto and U. Nagashima, Comput. Phys. Commun. **166**, 58 (2005).
- [109] N. F. Aguirre, P. Villarreal, G. Delgado-Barrio, E. Posada, A. Reyes, M. Biczysko, A. O. Mitrushchenkov, and M. P. de Lara-Castells, J. Chem. Phys. **138**, 184113 (2013).
- [110] T. Kreibich and E. Gross, Phys. Rev. Lett. **86**, 2984 (2001).
- [111] J. S. Lee and D. Secrest, J. Chem. Phys. **85**, 6565 (1986).
- [112] S. T. Kim and J. S. Lee, Bull. Korean Chem. Soc. **16**, 1232 (1995).
- [113] I. Baccarelli, F. Gianturco, and F. Schneider, J. Phys. Chem. A **101**, 6054 (1997).
- [114] M. Beyer, A. Lammers, E. Savchenko, G. Niedner-Schatteburg, and V. Bondybey, Phys. Chem. Chem. Phys. **1**, 2213 (1999).
- [115] J. Lundell, M. Pettersson, and M. Räsänen, Phys. Chem. Chem. Phys. **1**, 4151 (1999).
- [116] J. Y. Qu, W. Li, R. Guo, and X. S. Zhao, J. Chem. Phys. **117**, 2592 (2002).

- [117] A. N. Panda and N. Sathyamurthy, *J. Phys. Chem. A* **107**, 7125 (2003).
- [118] F. Filippone and F. Gianturco, *Europhys. Lett.* **44**, 585 (1998).
- [119] F. Gianturco and F. Filippone, *Chem. Phys.* **241**, 203 (1999).
- [120] B. Balta and F. Gianturco, *Chem. Phys.* **254**, 203 (2000).
- [121] F. Gianturco and F. Filippone, *Comput. Phys. Commun.* **145**, 78 (2002).
- [122] K. T. Giju, S. Roszak, and J. Leszczynski, *J. Chem. Phys.* **117**, 4803 (2002).
- [123] T. Ritschel, P. Kuntz, and L. Zülicke, *Eur. Phys. J. D* **33**, 421 (2005).
- [124] T. Ritschel, C. Zuhrt, L. Zülicke, and P. Kuntz, *Eur. Phys. J. D* **41**, 127 (2007).
- [125] W. David, *Chem. Biol. Interact.* **117**, 191 (1999).
- [126] M. Tachikawa, *Mol. Phys.* **100**, 881 (2002).
- [127] T. Udagawa, T. Ishimoto, H. Tokiwa, M. Tachikawa, and U. Nagashima, *Chem. Phys. Lett.* **389**, 236 (2004).
- [128] M. F. Shibl, M. Tachikawa, and O. Kuhn, *Phys. Chem. Chem. Phys.* **7**, 1368 (2005).
- [129] Y. Iwabata, Y. Imamura, and H. Nakai, *J. Phys. Chem. A* **115**, 1433 (2011).
- [130] C. Swalina, M. Pak, A. Chakraborty, and S. Hammes-Schiffer, *J. Phys. Chem. A* **110**, 9983 (2006).
- [131] S. T. Kim and J. S. Lee, *J. Chem. Phys.* **110**, 4413 (1999).
- [132] K. Morokuma, *J. Chem. Phys.* **55**, 1236 (1971).
- [133] P. Su and H. Li, *J. Chem. Phys.* **131**, 014102 (2009).
- [134] J. Watson, *J. Mol. Spectrosc.* **45**, 99 (1973).
- [135] J. Almlöf, *Chem. Phys. Lett.* **17**, 49 (1972).
- [136] M. Tachikawa and M. Shiga, *J. Am. Chem. Soc.* **127**, 11908 (2005).
- [137] C. P. Gonçalves and J. R. Mohallem, *Theor. Chem. Acc.* **110**, 367 (2003).
- [138] S. Takahashi and K. Takatsuka, *J. Chem. Phys.* **124**, 144101 (2006).
- [139] J. R. Mohallem, L. G. Diniz, and A. S. Dutra, *Chem. Phys. Lett.* **501**, 575 (2011).
- [140] P. J. Knowles and N. C. Handy, *Comp. Phys. Comm.* **54**, 75 (1989).

- [141] A. M. Frolov, *Phys. Rev. A* **61**, 022509 (2000).
- [142] S. G. Lias, Section 10, atomic, molecular, and optical physics, ionization energies of gas-phase molecules, in *CRC Handbook of Chemistry and Physics*, edited by D. R. Lide, pp. 10–206, CRC Press, 2010.